Humidity dependent impedance of Zn(_x)Co(_2-x)GeO(_4)

Hales, Debbie

HUMIDITY DEPENDENT

IMPEDANCE OF

$Zn_xCo_{2-x}GeO_4$

by

Debbie Hales

A thesis presented in candidature for the degree of

Doctor of Philosophy

at the

University of Durham

UK

Department of Physics

May 1999

ABSTRACT

$Zn_xCo_{2-x}GeO_4$ materials were prepared and the variation in structure with composition was investigated using XRD, SEM and EDX analysis. Limited series of solid solution were identified at both ends of the compositional range.

D.C. electrical measurements were carried out to characterize the variation in the resistivity of the materials with humidity. Resistivities of the order of 10^8 Ω m were observed in dry conditions, decreasing by 4 to 5 orders of magnitude with increasing humidity. Resistivity was not found to vary greatly with composition. Resistivity was temperature dependent, increasing by 1 to 2 orders of magnitude for a 70°C decrease in temperature.

A.C. impedance measurements were performed to gain an understanding of the mechanism of the humidity dependent conductivity. At low frequencies impedance was found to be independent of frequency and humidity dependent. At high frequencies impedance was found to be inversely proportional to frequency and independent of humidity. The break point frequency was also humidity dependent and an increase in the impedance indicated inductive-type behaviour. Complex plane representation of the impedance gave a distorted semicircle at high frequencies and a low frequency tail. At high humidities the tail appears as a straight line, inclined at approximately 45°. At medium levels of humidity a distinctive loop is apparent at the intersection between the semicircle and the tail, corresponding to the inductive behaviour indicated at the break-point frequency. The impedance response was modelled by an equivalent circuit consisting of various ideal and constant phase (dispersive) elements.

The proposed mechanism of humidity-dependent conductivity is due to chemisorption and physisorption of water vapour from the atmosphere at the surface of the material. It is suggested that conduction occurs by hopping of protons between chemisorbed hydroxyl groups at low humidities, by diffusion of H_3O^+ ions between the hydroxyl groups at intermediate humidities and by hopping of protons between physisorbed H_3O^+ ions (Grotthus Chain reaction) at high humidities.

DECLARATION

I declare that all the work in this thesis was carried out by the candidate except when explicitly stated otherwise. I also declare that none of this work has been previously submitted for any degree and that it is not currently being submitted for any other degree.

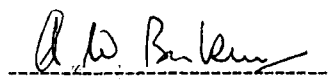

Dr. A. W. Brinkman

Supervisor

Debbie Hales

Candidate

ACKNOWLEDGEMENTS

I would like to thank my supervisor, Dr. Andy Brinkman, for his help and patience over the years, Elmwood Sensors Ltd and Peter Thompson for their support in the first few years, Dr. Tooraj Hashemi for his help and friendship during my time at Elmwood and since, Dr. Mike Petty for the use of the impedance analyser, Harry Kelly for building the humidity chamber and Norman Thompson and David Pattinson for their excellent technical support.

Thanks also to all the great friends I have made in the department over the years, but especially to Tim Hallam for all those coffee breaks back at the start, to Chris Leighton and Matt Hogan for their great help and to Sharon Fairless for being such a good friend.

I would also like to thank all my friends elsewhere, but especially Carol, Colin, Jill, Chris and Kandy.

Thanks to my family for their tremendous support and finally, thanks to Fanjio, who never complained about how late I worked!

STATEMENT OF COPYRIGHT

This thesis is dedicated

to my parents

CONTENTS

CHAPTER 1

INTRODUCTION

Zinc-cobalt germanate has not previously been utilized as a material for humidity sensing. Its potential in this respect was noted during the course of a preliminary study of various ceramic materials for other applications, when it was found to have humidity sensitive resistivity. It was therefore decided to investigate zinc-cobalt germanate as a potential new humidity sensing material.

The field of humidity sensing has expanded rapidly and the use of humidity sensors has become widespread, as shown in Table 1. Many different areas of application require different operating conditions and thus different types of humidity sensors have been developed utilizing various materials.

Humidity can be quantified by various characteristics, such as dew point, absolute humidity or relative humidity. Dew point is the temperature at which water begins to condense when moist air is cooled at constant pressure and constant water vapour content. Absolute humidity is the mass of water vapour in the atmosphere per unit volume, and relative humidity is the ratio of the mass of water vapour in the atmosphere to the mass of water vapour at saturation. (Numerical definitions are given in Chapter 2.) Which of these quantities needs to be measured depends on the application. In most applications it is more important to measure relative humidity than absolute humidity. Where either can be measured it is usually preferable to measure relative humidity because this is generally simpler and therefore cheaper[1]. Dew point measurements are required in applications where the presence of dew or condensation could be detrimental, for instance on the cylinder heads of VTRs, car windows and duplicating machines.

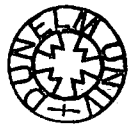

Dew-point hygrometers all work by measuring the temperature at which condensation occurs on a surface. There are various methods used for detecting condensation; by measuring the changes in reflectivity of a mirrored surface, by measuring the relative attenuation of acoustic waves passed over a surface, by measuring the attenuation of a bulk crystal quartz oscillator or by direct mass measurement of the condensation[2]. Dew point hygrometers give an absolute measure of water vapour concentration and provide better accuracy than relative humidity sensors but are usually more expensive[2].

Many different relative humidity sensors are in use and these can be classified according to the types of sensing materials used and their operating principles. The different types of sensing materials in use are electrolytes, organic polymers and ceramics[3,4]. Sensors utilise the changes in the electrical properties of the materials which occur when atmospheric humidity conditions vary. Measurement of atmospheric humidity is based on measurement of either the impedance or the capacitance of the sensing material. Impedance-type sensors can be further sub-divided by the nature of the electrical transport mechanism - whether by ionic or electronic charge carriers (with electrolytic sensors and p-n junctions being special cases of ionic transport). Examples of the various types of materials and different operating principles are given in Table 2.

Lithium chloride electrolyte humidity sensors have been widely used in radio-sonde circuits as well as in instruments for medical services[3,4]. A LiCl solution is immersed in a porous supporting material across which a potential difference is applied to form an electrolytic cell. The resistance of the cell changes when water vapour from the atmosphere is absorbed by the porous material and electrolysed, adding to the current flow due to electrolysis of the LiCl solution.

Polymer humidity sensors fall into two categories, polymer dielectrics, in which humidity is measured by changes in capacitance, and polyelectrolytes, in which humidity measurements are based on changes in resistance. Early polymer humidity

sensors used mechanical output from the dilation of hairs or synthetic fibres, although these were not very accurate due to creep[1].

Capacitive polymer sensors are based on the fact that, since the dielectric constant of the polymers is approximately 5, whilst that of water is around 80, the adsorption of water by a polymer would cause an increase in the relative permittivity[1]. This apparent increase in relative permittivity results in a linear increase in capacitance with increasing relative humidity[5]. Polyimides and cellulose esters are examples of polymers used in dielectric polymer humidity sensors[1]. The problems with polymer dielectrics are that they are sensitive to temperature, only being able to operate at low temperatures and requiring temperature compensation. They also exhibit slow response[5]. This is due to the fact that their mechanism relies on a bulk phenomenon. The advantage of a bulk mechanism is that the materials are relatively resistant to contamination[1]. The electrical response can show hysteresis[5], i.e. the resistance does not return to its original value for a cyclic change in humidity. This is thought to be due to clustering of the adsorbed water molecules resulting in residual water content on reduction of humidity[5]. The sensors also experience long-term drift and experience degradation on exposure to some solvents[3]. Another widely used polymer dielectric sensor material is cross-linked polymethylmethacrylate (PMMA)[6]. It has a hydrophobic nature so absorbs less water for a corresponding increase in humidity than certain cellulose derivatives and this results in less evidence of hysteresis.

Resistive polymer sensors consist of cross-linked polymers with hydrophilic ionic species appended to the polymeric backbone. Their capacity to absorb water depends on the nature and concentration of the ionic appendages[1]. The conductivity increases with an increase in water adsorption, due to increasing ionic mobility and/or charge carrier concentration[4]. An example of a polyelectrolyte sensor material is iodine-doped polyphenylacetylene (PPA)[7]. Bulk devices in the form of pressed pellets of PPA have been shown to exhibit resistance changes ranging from $10^{12}\,\Omega$ in dry conditions to $10^{5}\,\Omega$ at 90% relative humidity. Polyelectrolyte sensors do not have good stability because ion exchange between polar sites and the environment result in internal

chemical change over time. This can be controlled by copolymerization with more stable resins and by the use of protective coatings[1]. Also, being hydrophilic and soluble, polyelectrolyte sensors have poor durability to liquid phase water, such as dew condensation, and hence cannot be used at high humidities[4]. The problem of solubility can be overcome by forming a graft copolymer from a hydrophobic trunk polymer and a hydrophilic branch polymer, e.g. polytetrafluoroethylene (PTFE)-graft-polystyrene, by crosslinking of the hydrophilic polymer to make it insoluble or by forming an interpenetrating polymer network (IPN) from a cross-linked hydrophilic polymer and a cross-linked hydrophobic polymer[5].

Ceramic humidity sensors are generally much less sensitive to temperature than polymers[1] and also have advantages over polymers in terms of their mechanical strength, resistance to chemical attack and their thermal and physical stability[3].

Ceramic humidity sensors can be classified into groups according to their humidity-sensing mechanisms, namely ionic conduction-type, electronic conduction-type, capacitive type and p-n heterojunctions[3], as shown in Table 2. The ionic and electronic type sensors operate by measuring changes in the conductivity of the sensing material with humidity. The mechanisms of these conductivity changes will be discussed in Chapter 2. Certain materials are referred to in the literature as electrolyte type sensors[8,9]. These are essentially ionic type impedance sensors in which water vapour from the atmosphere is absorbed by the ceramic material and the resulting current varies with the quantity of water adsorbed, as is discussed in greater detail in Chapter 2. In this way the ceramic material of these and other ionic type sensors acts as a solid electrolyte, allowing the movement of charges when a potential difference is applied across the material. In a capacitive-type sensor the capacitance of the sensing material increases with increasing relative humidity due to the relative permittivity of water absorbed by the material[4]. A p-n heterojunction is a junction between two different semiconducting materials, where one is p-type and the other is n-type. The humidity sensing property of such a junction is due to the electrolysis of absorbed water which occurs at the contact points between the two materials[3,10]. When a potential

difference is applied to the junction with the positive terminal connected to the p-type material (forward bias) electrons flow from the n-type material to the p-type. Water molecules absorbed at the contact are electrolysed and the H^+ and OH^- ions migrate to the n-type and p-type sides of the junction respectively and contribute to the current flow through the junction. Current flow increases at higher humidities as the rate of the hydrolysis increases with increasing amount of absorbed water.

The main problem with many ceramic sensor materials is the need for periodic heating in order to recover their humidity-sensitive properties after prolonged exposure to humidity[3]. Contamination by impurities in the atmosphere such as dust, dirt, oil, smoke, alcohol and solvents can also be a problem. These can also be removed from the ceramic surface by heat cleaning[3]. The performance of ceramic sensors is affected more than that of polymers by contamination because their sensing mechanism relies on a surface effect[1].

In cases where ceramic sensors can be operated without heat cleaning they are very low in cost. Ceramic humidity sensors generally function well over the entire humidity range although resistive-type ceramic sensors are not so suitable for use at very low humidities because of their high resistivity whilst capacitive-type ceramic sensors function well at low humidity but are subject to severe drift at high humidity[1].

Some materials are capable of detecting changes in other atmospheric conditions in addition to humidity, such as gas concentration or temperature[3]. This can cause problems where the humidity response of a material can be masked by its response to other parameters, but these properties can also be utilized to give a multifunctional sensor. Examples of multifunctional sensors are SnO_2, which can detect temperature and flammable gases as well as humidity[11], $ZnO\text{-}TiO_2\text{-}SnO_2$, which can detect temperature and chemical vapours such as acetone, ethanol and ammonia as well as humidity, and $ZrO_2\text{-}Y_2O_3$, which can detect oxygen as well as humidity[8,9].

Industry	Application areas	Temperature (°C)	Humidity (% *r.h.*)
Domestic	air conditioners	5-40	40-70
electrical	drying of clothing	80	0-40
appliances	cooking control in microwave ovens	5-100	0-100
	VTRs (dew prevention)	0-60	60-100
Automobile	rear-window defoggers	-20-80	50-100
	motor assembly line	17-25	40-55
Medical	respiratory equipment	20-30	80-100
	sterilizers	>100	0-100
	incubators	10-30	50-80
	surgical rubber goods treatment	23-25	25-30
	pharmaceuticals	20-25	20-40
	biological products	0-6	60-65
Agriculture	greenhouse air-conditioning	5-40	0-100
	plantation protection (dew prevention)	-10-60	50-100
	cereal stocking	15-20	0-45
	broiler farming	20-25	40-70
Industry	humidity control in factories	5-40	0-50
	dryers	50-100	0-50
	ovens	100-500	0-100
	film desiccation	20-60	0-30
	humidifiers for industry	30-300	50-100
	paper	10-30	50-100
	textiles	10-30	50-100
	ceramic powders	5-100	0-50
	fire brick desiccation	45-55	50-60
	electronic parts	5-40	0-50
Alimentary	dried foodstuffs	50-100	0-50
	alimentary paste preparation	20-25	38
	slicing of salami	15	45
	fruit storage	-1-1	75-85
	frozen meat storage	-17-15	85
	sugar storage	25	45
	hard cake manufacturing	20-25	30-50
	chocolate covering	16-17	50-55
Measurement	thermostatic baths	-5-100	0-100
	repair and calibration of instruments	18	50-55
	radiosondes for meteorology	-5-40	0-100
	hygrometers	-5-100	0-100
Others	soil humidity	5-30	0-90
	book storage	17-20	38-50
	fur storage	-2-5	50-65
	photography	20-25	50-70
	printing	20-30	40-80

Table 1 - Applications of humidity sensors, with operating temperature and humidity ranges[3].

Table 2 - Types and characteristics of humidity sensors[4].

Type of material	Operating principle	Sensing element	Operating Temp. (°C)	Range Humidity (% *r.h.*)	Response time	Reference
Electrolyte	Impedance	LiCl + polyvinyl acetate	-40-60	10-99	2 - 5 min	4
	(ionic)	LiCl + glass fibre sheet	-30-50	15-99	3 - 10 min	4
Organic	Impedance	Iodine-doped polyphenylacetylene	30-60	10-90	30 s	7
polymer	Capacitance	Polyimide	25	0-100	1 min	1,4
		x-linked polymethylmethacrylate	-20-60	10-90	30 s	6
Porous	Impedance	$MgCr_2O_4$ - TiO_2	0-150	1-100	10 s	4,12-14
ceramics	(ionic)	TiO_2 - V_2O_5	0-150	15-100	10 s	4
		TiO_2 - Nb_2O_5	25	10-90	2 min	15
		TiO_2 - K_2TiO_{13}	25	15-95		16
		$ZnCr_2O_4$ - $LiZnVO_4$	0-150	30-90	3 min	4,17
		$MgAl_2O_4$	40	2-98	5 s	18-21
		$MgFeO_2$	40	5-95	5 s	18,20,22
		$(Ba,Sr)TiO_3$	25	15-95	5 s	23-26
		$(Pb,La)(Zr,Ti)O_3$	30-45	0-90	2 min	27
		$CaTiO_3$	15-85	15-95		28
		$Ni(Al,Fe)_2O_4$ - TiO_2	35	3-90	< 40 s	29
		ZrO_2 - TiO_2	40-80	20-95		30
	(SolidElectrolyte)	ZrO_2 - Y_2O_3	50-150	0-450mmHg	1 - 2 min	8,9
	Impedance	$Sr_{1-x}La_xSnO_3$	300-500	1-10ppm	2 min	4,31
	(electronic)	ZrO_2 - MgO	400-700	1-10ppm	10 s	4,10,32
		SnO_2	10-360	$55gm^{-3}$	1 min	11
		$Sr(Sn,Ti)O_3$	400			31
	Capacitance	Al_2O_3	-10-40	1-100	10 s	4
		Ta_2O_5 - MnO_2	-10-55	1-100	1 min	4
		$MnWO_4$	15-35	25-95	5 - 15 s	33
	p-n junction	NiO - ZnO	20	5-85		10
		CuO - ZnO	22	10-100	1 min	34

REFERENCES

[1]B. M. Kulwicki, "Humidity sensors", J. Am. Ceram. Soc, **74** (4), 697-708 (1991).

[2]K.A. Vetelino, P.R. Story, R.D. Mileham and D.W. Galipeau, "Improved dew point measurements based on an SAW sensor", Sens. & Act., **35-36**, 91-98 (1996).

[3]E. Traversa, "Ceramic sensors for humidity detection: the state-of-the-art and future developments", Sens. & Act. B, **23**, 135-156 (1995).

[4]N. Yamazoe and Y. Shimizu, "Humidity sensors - principles and applications", Sens. & Act., **10** (3-4), 379-398 (1986).

[5]Y. Sakai, "Humidity sensors using chemically modified polymeric materials", Sens. & Act. B, **1993** (13), 82-85 (1993).

[6]M. Matsuguchi, Y. Sadaoka, Y. Sakai, T Kuriowa and A. Ito, "A capacitive type humidity sensor using cross-linked poly(methyl-methacrylate) thin films", J. Electrochem. Soc., **138**, 1862-1865 (1991).

[7]A. Furlani, G. Iucci, M. V. Russo, A. Bearzotti and A. D'Amico, "Thin films of iodine-polyphenylacetylene as starting materials for humidity sensors", Sens. & Act. B, **7**, 447-450 (1992).

[8]H. Yagi and K. Ichikawa, "Humidity sensing characteristics of a limiting current type planar oxygen sensor for high temperature", Sens. & Act. B, **13**, 92-95 (1993).

[9]T. Usui, Y. Kurumiya, K. Nuri and M. Nakazawa., "Gas-polarographic multifunctional sensor: oxygen, humidity sensor", Sens. & Act., **16**, 345-358 (1989).

[10]J.G. Fagan and V.R.W. Amarakoon, "Reliability and reproducibility of ceramic sensors: part III, humidity sensors", Am. Ceram. Soc. Bull., **72** (3), 119-130 (1993).

[11]S. Mukode and H. Futata, "A semiconductive humidity sensor", Sens. & Act., **16**, 1-11 (1989).

[12]T. Nitta, Z. Terada, and S. Hayakawa, "Humidity-sensitive electrical conduction of $MgCr_2O_4$ - TiO_2 porous ceramics", J. Am. Ceram. Soc., **63** (5-6), 295-300 (1980).

[13]T. Nitta and S. Hayakawa, "Ceramic humidity sensors", IEEE Trans. Components Hybrids Manufact. Technol., **CHMT-3**, 237-243 (1980).

[14]G. Drazic and M. Trunteij, "Preparation and properties of ceramic sensor elements based on $MgCr_2O_4$", Sens. & Act., **18**, 407-414 (1989).

[15]K. Katayama, K. Hasegawa, T. Takahashi, T. Akiba and H. Yanagida, "Humidity sensitivity of Nb_2O_5 - doped TiO_2 ceramics", Sens. & Act., **24**, 55-60 (1990).

[16]Y-C. Yeh, T-Y. Tseng, and D-A. Chang, "Electrical properties of TiO_2-$K_2Ti_6O_{13}$ porous ceramic humidity sensor", J. Am. Ceram. Soc., **73** (7), 1992-1998 (1990).

[17]Y. Yokomizo, S. Uno, M. Harata and H. Hiraki, "Microstructure and humidity-sensitive properties of $ZnCr_2O_4$ - $LiZnVO_4$ ceramic sensors", Sens. & Act., **4**, 599-606 (1983).

[18]Y. Shimizu, H. Arai, and T. Seiyama, "Theoretical studies on the impedance-humidity characteristics of ceramic humidity sensors", Sens. & Act., 7, 11-22 (1985).

[19]G. Gusmano, G. Montesperelli, P. Nunziante and E. Traversa, "Study of the conduction mechanism of $MgAl_2O_4$ at different environmental humidities", Electrochim. Acta, **38** (17), 2617-2621 (1993).

[20]G. Gusmano, G. Montesperelli, P. Nunziante and E. Traversa, "Microstructure and electrical-properties of $MgAl_2O_4$ and $MgFe_2O_4$ spinel porous compacts for use in humidity sensors", B. Ceram. Trans., **92** (3), 104-108 (1993).

[21]G. Gusmano, G. Montesperelli, E. Traversa, A. Bearzotti, C. Petrocco, A. D'Amico and C DiNatale, "Magnesium aluminium spinel thin film as a humidity sensor", Sens. & Act., 7, 160-463 (1992).

[22]G. Gusmano, G. Montesperelli, P. Nunziante and E. Traversa, "Humidity sensitive electrical response of sintered $MgFe_2O_4$", J. Mater. Sci., **28**, 6195-6198 (1993).

[23]J. Slunecko, J. Holc, M. Hrovat amd M. Ceh."Thick film humidity sensors based on $(Ba,Sr)TiO_3$ porous ceramic doped with MgO and CaO", Sens. & Act., **B 7**, 439-442 (1992).

[24]Y-C. Yeh, T-Y. Tseng, and D-A. Chang, "Electrical properties of porous titania ceramic humidity sensors", J. Am. Ceram. Soc., **72** (8), 1472-1475 (1989).

[25]Y.C. Yeh and T.Y. Tseng, "Humidity-sensitive electrical properties of $Ba_{0.5}Sr_{0.5}TiO_3$ porous ceramics", J. Mater. Sci. Lett., 7, 766-768 (1988).

[26]Y.C. Yeh and T.Y. Tseng, "Analysis of the D.C. and A.C. properties of K_2O - doped porous $Ba_{0.5}Sr_{0.5}TiO_3$ ceramic humidity sensor", J. Mater. Sci., **24**, 2739-2745 (1989).

[27]Y. Sadaoka, M. Matuguchi, Y. Sakai, H. Aono, S. Nakayama and H. Kuroshima, "Humidity sensors using KPH_2PO_4 - doped porous (Pa La) (Zr, Ti) O_3", J. Mater. Sci., **22**, 3685-3692 (1987).

[28]D. A. Chang and T. Y. Tseng, "Humidity-sensitive characteristics of $CaTiO_3$ porous ceramics", J. Mater. Sci. Lett., **9**, 943-944 (1990).

[29]L. Wu, C.C. Wu, and J.C. Her, "$Ni(Al,Fe)_2O_4$ - TiO_2 ceramic humidity sensors", J. Mater. Sci., **26**, 3874-3878 (1991).

[30]S.L. Yang and J.M. Wu, "ZrO_2 - TiO_2 ceramic humidity sensors", J. Mater. Sci., **26**, 631-636 (1991).

[31]T. Seiyama, N. Yamazoe, and H. Arai, "Ceramic Humidity Sensors", Sens. & Act., **4** (1), 85-96 (1983).

[32]T. Nitta, Y. Fukushima, and Y. Matsuo, "Water vapour gas sensor using ZrO_2 - MgO ceramic body", Anal. Chem. Symp. Ser.: Chemical Sensors, **17** (Kodansha, Tokyo/ Elsevier, Amsterdam), 387-392 (1983).

[33]W. Qu and J.U. Meyer, "A novel thick-film ceramic humidity sensor", Sens. & Act., **B 40**, 175-182 (1997).

[34]Y. Ushio, M. Miyayama, and H. Yanagida, "Fabrication of thin-film CuO/ZnO heterojunction and its humidity sensing properties", Sens. & Act. B, **12**, 135-139 (1993).

CHAPTER 2

LITERATURE REVIEW

2.1 HUMIDITY MEASUREMENT PARAMETERS

Humidity is a measure of the amount of water vapour in the atmosphere. This can be defined in various ways, such as dew point, absolute humidity or relative humidity.

Dew point is the temperature at which water begins to condense when moist air is cooled at constant pressure and constant water vapour content.

Absolute Humidity, F_{ab}, is defined as the mass of water vapour in the atmosphere, m_w, per unit volume:

$$F_{ab} = m_w / V \qquad \textbf{(2.1)}$$

Saturation Humidity, F_s, is defined as the mass of water vapour at saturation, m_{ws}, per unit volume:

$$F_s = m_{ws} / V \qquad \textbf{(2.2)}$$

The Saturation Humidity is temperature dependent and gives the maximum amount of water vapour that may be present in a unit volume at a given temperature.

Relative Humidity, $r.h.$, is expressed by the ratio of Absolute Humidity to Saturation Humidity given as a percentage:

$$r.h. = 100\, F_{ab} / F_s \qquad \textbf{(2.3)}$$

2.2 HUMIDITY SENSING MECHANISMS

All ceramic humidity sensing mechanisms, ionic conduction, electronic conduction, capacitive, solid-electrolyte and p-n heterocontact, rely on the adsorption of water vapour from the atmosphere by either or both of two basic adsorption processes - chemical adsorption and physical adsorption[1,2]. Some sensing devices are also affected by the action of capillary condensation[1,3]. These processes govern the electrical properties of the conduction, capacitance or electrolytic conduction depending on the sensor type. The sensing mechanisms of the capacitive, solid-electrolyte and p-n heterocontact type were outlined in Chapter 1. Here the ionic and electronic conduction types are discussed.

2.2.1 ADSORPTION OF WATER - CHEMISORPTION

Chemisorption of water vapour occurs at the surface of an oxide material by a process of dissociation and adsorption. Each water molecule dissociates to form a hydroxyl and a proton. The hydroxyl bonds to a metal cation in the oxide surface and the proton reacts with an O^{2-} ion in the surface to form a second hydroxyl[1,4], as shown in Figure 2.1.

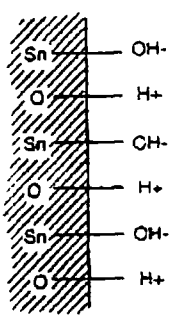

Figure 2.1 - Schematic representation of chemisorbed water on SnO_2[2].

The layer of chemisorbed water molecules, once formed, is very stable and unaffected by subsequent changes of relative humidity[1,2]. The chemisorbed layer can be removed by heating the material to a temperature of approximately 400°C, at which the surface hydroxyls will desorb[1,5-7].

2.2.2 ADSORPTION OF WATER - PHYSISORPTION

After a single layer of water molecules has been chemisorbed, physisorption of water molecules occurs. In physisorption the water molecules do not dissociate but are adsorbed onto the first hydroxyl layer. The first layer of physisorbed water molecules are localized by double hydrogen bonding of each water molecule[1,4], as shown in Figure 2.2. Subsequent layers of physisorbed water molecules are singly bonded. These layers become less constrained as they build up with the first few layers having an ice-like structure, while layers formed further from the ceramic surface are more liquid-like[4].

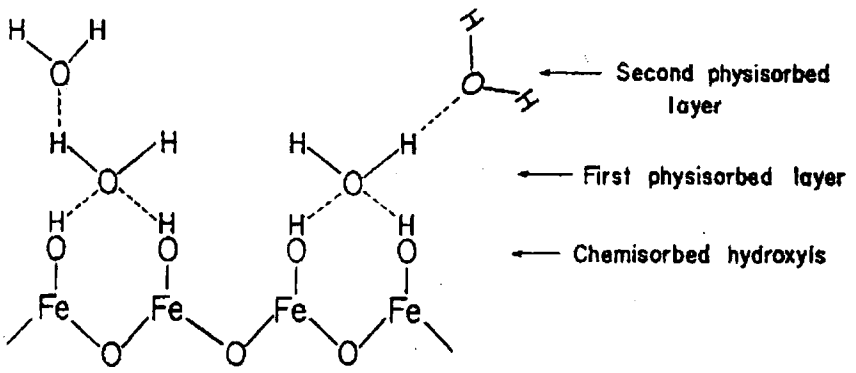

Figure 2.2 - Layers of adsorbed water molecules on an iron oxide surface[4].

Physisorption is reversible, all physisorbed layers can be removed by decreasing the humidity of the atmosphere[5]. Physisorption takes place only below 100°C, at normal pressures, whilst chemisorption can take place up to temperatures of approximately 400°C[6].

2.2.3 CAPILLARY CONDENSATION

In ceramics with porous structure condensation of water can take place in the capillary pores. The occurrence of capillary condensation can be theoretically described. If the pores are cylindrical, with one end closed, condensation occurs in all pores with radii up to r_K given by the Kelvin equation,

$$r_K = \frac{2\gamma M}{\rho R T \ln(p_{ws}/p_w)} \qquad (2.4)$$

where γ, ρ and M are the surface energy, density and molecular weight of water respectively, p_w and p_{ws} are water vapour pressure in the surrounding environment and saturation water vapour pressure respectively, R is the gas constant and T is absolute temperature[3]. In open pores, i.e. those open at both ends, condensation takes place in pores with radii up to $r_K/2$. In reality the pores in a ceramic are not cylindrical or of uniform radius but are, in fact a series of interconnecting constituent pores of different radii forming a 3-dimensional network. In such cases condensation depends also on whether adjacent pores are filled with condensed water. When capillary pore radii are less than approximately 2nm, the surface tension of the water inside the capillary pores exceeds its tensile strength and spontaneous evaporation takes place[5]. Also capillary condensation cannot occur at relative humidities less than about 40% since under these conditions the water vapour will adsorb onto the pore walls thus existing only as an adsorbed phase and not as a condensate.

2.2.4 IONIC CONDUCTION-TYPE SENSING MECHANISM

In an ionic conduction-type humidity sensor conductivity increases exponentially with the content of water vapour in the atmosphere[8]. The conductivity is controlled by the amount of water vapour adsorbed from the atmosphere onto the surface of the sensor.

The conduction mechanism depends on the surface coverage of adsorbed water. When only the layer of chemisorbed hydroxyl ions are present conduction occurs by hopping of protons, H^+, between adjacent hydroxyl groups[1,8].

In the physisorbed layers water molecules dissociate into hydroxide ions, OH^-, and hydronium ions, H_3O^+, as follows[2,5]:

$$2H_2O \Leftrightarrow H_3O^+ + OH^-$$

The energy of formation of H_3O^+ from a bare proton and a water molecule under vacuum suggests that H_3O^+ is more stable than a bare proton[8]. In the first physisorbed layer the water molecules tend to dissociate more readily due to the high local electron charge density and electrostatic fields in the underlying chemisorbed layer[1,2].

When molecular water is present but surface coverage is not complete, i.e. in the initial layer of physisorbed water, conduction takes place predominantly by diffusion of H_3O^+ ions between neighbouring hydroxyl groups[1,8].

When more molecular water is present in the physisorbed layer charge transport occurs by the hopping of protons from one water molecule to another. One H_3O^+ ion releases a proton to a nearby H_2O molecule, ionizing it and forming another H_3O^+ ion. This process is known as the Grotthus Chain reaction and is the charge transport mechanism which occurs in liquid water[1,2,5,8]. It is possible that mobile protons may come from dissociation of hydroxyl groups in the chemisorbed layer but this is not

energetically favourable since the activation energy required to dissociate hydroxyl ions is higher than that necessary to dissociate water molecules[1].

There is a gradual variation between conduction by diffusion of H_3O^+ ions and conduction by the proton transfer mechanism whereby as more physisorbed water is present clustering of water molecules occurs, forming patches of liquid-like network of hydrogen-bonded water molecules within which conduction occurs by proton transfer[1,8]. When physisorbed water molecules are abundant, i.e. there is a complete layer of physisorbed water, conduction by proton transfer process is dominant.

Carrier concentration depends on the number of physisorbed molecules dissociating at the surface. In pure liquid water the fraction of dissociated water molecules is approximately 1×10^{-8} but in a physisorbed layer of water molecules formed on the surface of an ionic solid the fraction of dissociated water is estimated to be approximately 10^6 times greater than this. This gives a surface charge density of about 1×10^{13} ions/cm^2 per monolayer of adsorbed water[5].

Carrier concentration also increases when more than one layer of physisorbed water molecules is present. Water molecules in the first layer are bound to the surface by two hydrogen bonds whereas molecules in subsequent layers are singly bonded. The doubly bonded molecules are not as free to reorient in an applied electric field as those which are singly bonded - hence the singly bonded physisorbed water molecules make a greater contribution to the dielectric constant than the doubly bonded water molecules[8].

Condensation of water vapour in capillary pores also affects the conductivity, since electrolytic conduction occurs in the condensed water layer resulting in a further rise in conductivity[1,7].

The presence of defect lattice sites and chemisorbed oxygen atoms at the oxide surface may increase the number of water molecule adsorption sites[1,9]. Oxygen vacancies

created by reduction treatments or doping may also enhance the chemisorption of water[10].

$MgCr_2O_4$ - TiO_2 is an example of an ionic conduction-type sensing material. As well as an exponentially increasing conductivity with increasing atmospheric humidity it also exhibits characteristic polarization as indicated by its charging characteristics[17].

2.2.5 ELECTRONIC CONDUCTION-TYPE SENSING MECHANISM

Semiconducting oxides can act as electronic-type humidity sensors, where the conduction mechanism is dependent on the chemisorption of water molecules. In such cases the chemisorption of water can result in either an increase or a decrease in the resistivity depending on whether the semiconductor is n-type or p-type[1].

In electronic-type sensors there is generally a power law relationship between the resistivity and the water vapour concentration[3]. *Seiyama et al* state that the change in conductivity associated with a change in water vapour pressure is larger for an n-type electronic sensor, such as $SrSnO_3$, than for a p-type sensor, such as $SrTiO_3$[11], although it is not clear why. According to *Yamazoe et al*, elements of microstructure such as surface area and porosity have a much less pronounced effect on the sensing characteristics of electronic-type sensors than they do on the ionic-type[3]. Again it is not clear why this is so since both electronic and ionic mechanisms rely on adsorption of water vapour.

The electrical behaviour of electronic-type sensors in the presence of water vapour is similar to their behaviour in the presence of reducing gases[1]. In the presence of reducing gases a reaction takes place between the oxygen ions adsorbed on the surface of the semiconductor and the reducing gases, injecting electrons and therefore resulting

in a decrease in the resistivity of n-type semiconductors and an increase in p-type. The corresponding increase or decrease in conductivity of an n-type or p-type semiconducting oxide which occurs when water molecules are adsorbed onto the oxide suggests electron transfer from the water molecules to the oxide, as occurs in the electron donation from reducing gases; however this is not the case. When a water molecule is adsorbed onto an active site two surface hydroxyl groups are formed, H^+ being bonded to an oxide ion and OH^- to a metal ion. This reaction does not involve a release of charge. It has been suggested that electrons may be trapped by surface defects such as ionized oxygen vacancies and that these may be released when water molecules are adsorbed onto the defect sites[11]. However it is arguable whether vacancies can occur in such a surface – especially oxygen vacancies since a surface exposed to the atmosphere is most likely to be completely oxidized. In fact, in normal dry atmospheric conditions the surface of an oxide material is fully covered with adsorbed oxygen ions. It is thought that electrons trapped by the adsorbed oxygen ions are released when water molecules are coadsorbed onto the surface causing some of the oxygen ions to be desorbed[11,13]. This explanation is more feasible.

One advantage of electronic-type sensors is that they can operate at high temperatures, up to approximately 400°C, since chemisorption of water molecules can still occur at these temperatures[1-3]. Ionic sensors can only operate up to 100°C, the limiting temperature for the process of physisorption[4-6]. Electronic-type sensors can be operated with d.c. voltage because the conduction occurs by movement of electrons, which are free to flow from the material into electrodes on application of a potential difference. In an ionic-type sensor conduction occurs by movement of ionic charge (by hopping between ions) and these cannot flow into the electrodes so the application of a d.c. potential difference will result in an accumulation of charge at the electrodes.

The disadvantages of electronic sensors are their slow response times, their sensitivity to reducing gases[2] and their temperature dependence[14]. The response times of electronic sensors are relatively slow compared to those of ionic sensors. For example the p-type electronic sensor $SrTiO_3$ has a response time of 5 minutes as compared to 10 - 20 seconds for $MgCr_2O_4$ - TiO_2, an ionic type sensor[11,17]. The short response

time of such an ionic sensor arises from the rapid processes of physisorption and capillary condensation, whereas the slow response of an electronic-type sensor may be attributable to the relatively slow diffusion process involved in chemisorption[11]. The sensitivity to the presence of reducing gases is due to the transfer of electrons between the gas molecules and the ceramic, affecting the electronic conductivity and therefore the humidity sensitivity of the ceramic[2]. Electronic type sensors also tend to have significant temperature dependence. For example in the n-type sensor, SnO_2, the temperature dependence is stronger than the humidity dependence. This can be overcome by heating the sensor at a constant temperature of about 350°C, which serves to ensure that electronic conductivity is the dominant process[14].

Some ceramic sensors have been shown to exhibit both ionic and electronic conduction mechanisms. For example, TiO_2 - $K_2Ti_{16}O_{13}$[15] and $(Ba,Sr)TiO_3$[16], where conduction in a highly humid atmosphere is by both ions and electrons, with ions being the dominant carriers, whereas in a low-humidity atmosphere the dominant carriers are electrons.

2.2.6 EFFECT OF MICROSTRUCTURE ON HUMIDITY SENSITIVITY

Microstructure and porosity are very important factors in determining the electrical response of ionic-type humidity sensors to humidity because the conduction mechanisms rely on surface effects[12,17].

Shimizu et al have modelled the impedance-humidity characteristics of some ceramic humidity sensors on the basis of the amount of capillary condensation[12]. The calculated impedances were found to agree well with experimental values only when surface adsorbed ions were removed from the materials prior to measurement. This treatment thus takes no account of the effects of chemisorbed or physisorbed water and therefore can only be applicable where adsorption is minimal and condensation

effects are dominant. According to the theoretical treatment proposed, the impedance-humidity characteristics of a porous material can be calculated by summing the conductances of the condensed water in all the pores that are filled. Considering a disc-shaped sample with electrodes on both sides and making the simplification that all pores go right through the disc and are perpendicular to the electrodes[12], the conductance of the condensed water in a pore of radius r is given by:

$$G_{pore}(r) = \frac{\sigma_w \pi r^2}{l} \qquad (2.5)$$

where l is the length of the pore (or thickness of the disc), and σ_w is the conductivity of the condensed water in the pore. The electrical conductances of the pores act in parallel so the total conductance of all filled pores is:

$$G_w = \int_0^{rK} G_{pore}(r) n(r) dr \qquad (2.6)$$

where $n(r)$ is the number of pores, per unit radius, with radius between r and $r + dr$ and r_K is the maximum radius of pores filled by capillary condensation, as given by the Kelvin equation **(2.4)**. The total conductance of the disc due to both condensed water in pores and to the ceramic material itself, is given by:

$$G_T = G_w + G_o \qquad (2.7)$$

where G_o is the conductance of the disc in dry conditions. It is clearly necessary to know the pore size distribution, the intrinsic conductivity of the material and the conductivity of condensed water. Aside from the initial simplifications there is also the complication that as opposed to 'open' pores perpendicular to the electrodes the pores in fact consist of a three dimensional structure of pores in all orientations, some of which will be closed at either or both ends.

As shown by the above equations both total open porosity and pore-size distribution can influence the resistance - humidity sensitivity of those sensors in which capillary condensation is the most significant mechanism of conduction. From the Kelvin equation, taking surface energy, $\gamma = 0.073$ Nm^{-1}, the molar volume of water, M / ρ = 0.018×10^{-3} m^3, absolute temperature, T = 293 K, gas constant, R = 8.314 J K^{-1} mol^{-1} and relative humidity, *r.h.* = 100 (p_w / p_{ws}), at 10 % *r.h.* condensation will occur in pores up to a radius of 0.5 nm and at 98% *r.h.* condensation will occur in pores up to a radius of 53 nm. Thus pore sizes in the range 0.5 to 53 nm will allow capillary condensation across the range of humidity, whilst a uniform distribution of pores in this size range will result in a uniform contribution to the electrical conductivity from the condensed water over the range of humidity[18]. However this range of pore size is very small and most ceramic sensors tend to have pore sizes larger than this so that although there may be some capillary condensation, particularly in the interstices, it could not form the dominant mechanism.

The size of capillary pores also affects the adsorption processes. The rate of adsorption and desorption of water is controlled by the rate of diffusion of water vapour through the pores[11]. The presence of pores of sub-micron radius will slow the response time, whilst conversely the presence of larger pores will result in a faster response time[19,20]. Also a large specific surface area can lead to greater sensitivity to humidity due to a greater surface area being available for adsorption[1].

The porosity of a ceramic material can be controlled by the processing techniques, in particular the sintering temperature. The porosity, or total pore volume, of a ceramic material decreases with higher sintering temperature, whilst the grain size and overall density increases. An increase in sintering temperature will therefore generally result in a decrease in the surface area available for adsorption and this will result in a decrease in the sensitivity to humidity. For example $Ba_{0.5}Sr_{0.5}TiO_3$ specimens sintered at lower temperature showed larger specific surface areas, greater open porosity and better sensitivity to humidity[21]. Also the volume of closed pores (i.e. those closed at both ends) can increase with higher sintering temperature thus decreasing humidity sensitivity since closed pores do not contribute to humidity dependent conduction[20].

The microstructural characteristics of the starting materials used in the preparation of ceramics affect the microstructure of the final material. For example in the preparation of ceramic $MgFe_2O_4$ starting materials with submicrometer particle size gave ceramics with higher specific surface areas but smaller pores and lower total open porosity than samples prepared from powder with 0.5 - 10 μm particle size[19].

The addition of a pore-forming agent, such as graphite powder or organic particles, during the fabrication of a ceramic is a highly efficient method of controlling pore size. The pore forming agent is removed by burning out during the sintering process but acts to form pores in the ceramic material, increasing its porosity whilst ideally having no effect on the composition. This technique can allow sintering to be carried out at higher temperatures in order to achieve complete solid phase reaction, good mechanical strength and stability of electrical behaviour whilst still resulting in samples of suitable porosity. For example the addition of 10 to 20 weight percent of graphite to the starting materials in the preparation of $CoFe_2O_4$ and $MgCr_2O_4$ has been found to result in an increase in porosity thus giving greatly improved humidity sensitivity[22]. Neither auger electron spectrum (AES) analysis with Ar^+ etching, nor x-ray diffraction analysis revealed any trace of carbon[23], within the sensitivity limits of these methods (approximately 1% for an even distribution). Hence it was concluded that the graphite had been completely oxidised away during sintering. It is however possible that the graphite would cause reduction of the matrix material, as opposed to the fully oxidized state that would normally occur in a pure sample fired in air. There is no evidence presented in the literature as to whether or not this is the case.

Porosity can be controlled by the use of a binder containing a foaming agent which generates gas whilst the binder becomes rigid due to polymerization creating a highly porous structure[24]. Both binder and foaming agent are then burnt out during sintering. An existing porous structure, such as coral, may be impregnated with wax then chemically dissolved to leave a mould into which the ceramic powder slip is placed. The mould is then melted out during firing[24].

Porosity can also be controlled in the sintering stages by the addition of materials which affect the sintering process and remain in the final material but are not necessarily active in its electrical behaviour. Such sintering aids enable the formation of the required compound and the necessary mechanical strength at lower sintering temperatures. Sintering at lower temperatures allows the production of a material with greater porosity than could be achieved by sintering at the higher temperatures that would be necessary without the sintering aid. For example the addition of K_2CO_3 to TiO_2 allows the sensor material to be easily sintered with the resulting material having greater porosity so that the conductance-humidity sensitivity was found to be less dependent on sintering temperature[15,16]. Also the addition of TiO_2 to $MgCr_2O_4$ was found to enhance sintering by forming a solid solution with the chromite[17]. The larger the amount of TiO_2 added the greater the percentage of theoretical density that was achieved, with a corresponding decrease in the specific surface area. The best results for humidity sensitivity were obtained for 15 mol % TiO_2[17].

2.2.7 EFFECT OF DOPING ON HUMIDITY SENSITIVITY

The introduction of a small amount of dopant can improve the humidity response of some ceramic sensors. These can improve the overall conductivity and also in some cases the response of conductivity to humidity[3]. For example the addition of 1 mol % MgO or $FeO_{1.5}$ to ZrO_2 - TiO_2 increased its conductivity across the range of humidity[10] and the addition of 0.5 mol % Nb_2O_5 or V_2O_5 to TiO_2 also lowered its resistivity[20]. The addition of K^+, Li^+ or Na^+ to $MgFe_2O_4$[3] and K^+ to $NiWO_4$ and $ZnWO_4$[26] resulted in an improvement in their sensitivity to humidity. In the case of K_2O doped $Ba_{0.5}Sr_{0.5}TiO_3$ the conductance-humidity sensitivity of the doped material is an order of magnitude greater than the undoped material[21,25].

It has been suggested that the dopant ions may act as dominant charge carriers instead of protons[3]. This is thought to be the case in $ZnCr_2O_4$ - $LiZnVO_4$, where the hydrated Li^+ ions seem to contribute to charge transport and humidity sensitivity[3,27]. The dopant ions could also improve humidity-sensitive electrical response by increasing the number of sites available for water adsorption[1]. It has been suggested that this is due to the fact that dopant ions create defect-lattice sites and oxygen vacancies, resulting in an increase in the number of adsorption sites[10,25]. There is no direct evidence as to how the mechanism of doping works.

Ti - doped $MgCr_2O_4$ ceramic has a wide variation in resistance with relative humidity - up to 4 or 5 orders of magnitude. This is due to the distribution of the titanium and chromium cations in the spinel structure[28]. The cations on the surface are 5 co-ordinated but the oxide surface prefers to have a negative surface charge on adsorption of water molecules so adsorption induced Cr^{3+} / Cr^{2+} redox changes occur on the oxide surface, giving rise to great sensitivity in humidity-resistivity characteristics.

2.2.8 EFFECT OF COATINGS ON HUMIDITY SENSITIVITY

Coatings are used to improve humidity sensing performance in both electronic-type and ionic-type sensors. The coatings can protect the humidity sensitive material from contamination in the atmosphere or prevent drift in the response due to the build up of chemisorbed hydroxide ions. Coatings can take the form of a thin layer over the entire sensing element or on a microstructural level with the grains of the sensing material each surrounded by another material or phase.

Examples of the first type of coatings are Al_2O_3, SiO_2 or Mn_2O_3, as used to cover the electronic-type SnO_2 humidity-sensitive element in order to overcome its sensitivity to inflammable gases such as alcohol vapour[14].

An example of the second type of coating is found in the ionic-type $ZnCr_2O_4$ - $LiZnVO_4$ ceramic sensor where the vanadium compound forms a glassy phase which surrounds the ceramic grains of the $ZnCr_2O_4$[27]. Water vapour adsorbs and desorbs on this vanadium compound. The coating gives an improvement in the long-time drift in the response otherwise caused by the gradual increase in the amount of hydroxide ions adsorbed on the oxide surface. The vanadium phase coating allows the sensor to be operated without heat cleaning.

Another example is the coating of the $Sr_{1-x}La_xSnO_3$ electronic-type humidity sensor with Pt/Al_2O_3, which serves to suppress the interference of ethanol on the humidity response[3]. Silica coating was also found to be an effective means to eleiminate sensitivity to certain gases in an α-Fe_2O_3 humidity sensor[29].

2.3 CERAMIC PROCESSING METHODS

In the preparation of ceramics, raw materials are turned into the required compound in the form of a body of the required shape and size with specific required properties. The properties required may be electrical, thermal, magnetic or optical but in all cases mechanical strength is also necessary for the material to be durable. The properties of the finished ceramic are affected by its composition, grain size and porosity. These factors can be controlled in the preparation processes.

The various processes in the preparation of ceramics are mixing, calcination, shaping and sintering. Further details can be found in standard textbooks on ceramics[24,30,31]. Thorough mixing of the raw materials is important to ensure uniform compound formation during calcination or firing. Mixing is also important in controlling the rate of compound formation by reducing the particle size in the raw materials. During compound formation matter of neighbouring particles must interdiffuse and the time taken for this process is proportional to the square of the particle size[24]. Mixing is also

important to ensure uniform density after calcining or firing by breaking up aggregates in the starting materials, which would otherwise undergo more rapid internal densification than neighbouring particles during the heat treatment. Mixing also introduces defects into the crystal particles, which may enhance diffusion and accelerate sintering.

The method used most commonly for mixing is ball milling. It involves placing the starting materials, or charge, in a barrel, with some grinding media, usually in the form of spheres, cylinders or rods. The barrel is then steadily rotated for an extended period of time resulting in the charge being both mixed and ground by the action of the grinding media. The latter are inevitably abraded and may cause contamination of the charge. Contamination is minimized by optimizing the milling time, using hard material for the grinding media (flint, tungsten carbide or sialon) or by using a material for the grinding media which has the same composition as one of the constituents of the charge. For efficient mixing the optimum volume of charge should be about a third of that of the grinding media. Milling can be conducted either with or without the addition of liquid, although wet milling is faster than dry milling and also aids the final separation of the charge from the media. The disadvantage of wet milling is that the liquid must be removed afterwards, by filtration or evaporation. Water is commonly used since it is available at high purity, is low in cost, non-flammable and non-toxic. The volume of liquid must be sufficient to form the charge into a free flowing cream. This is usually 100 to 200% of the volume of the charge.

Calcination is a process of heat treatment which causes the constituents to react by interdiffusion of their ions. The ions redistribute themselves in such a way as to minimize the Gibbs free energy, or total internal energy, of the system. The required final phase may be completely formed or in some cases may be incomplete, but in such cases the remaining chemical gradients may assist sintering. The calcined material usually has undergone some degree of sintering and must be reground to form a powder suitable for shaping. In some cases calcination need not be performed as a separate process, but can occur during the sintering stage. In these cases the mixed raw materials are shaped directly.

The method used for shaping is very dependent on the shape to be produced. In some cases a binder can be used to give strength in the green body (unfired) form or to aid shaping. The binder must be a material which does not affect the final composition or density and will be burned or volatilized out during firing. One method of shaping, probably the simplest, is dry-pressing, where a measured quantity of free-flowing granulated powder is placed into a die and is compressed to a pre-determined volume or pressure. Others methods of shaping include isostatic-pressing, extrusion, slip-casting, band-casting and injection moulding.

Sintering is a heat treatment process used to convert a compacted powder into a dense structure of crystallites joined by grain boundaries. It involves the minimization of internal surface area and frequently an increase in grain size. Both of these processes are energy driven, i.e. they proceed because they result a decrease in energy. Minimization of internal surface area involves a reduction in the surface energy, and involves the transfer of matter from the interior of the grains, along the grain boundaries to adjacent pores, which are eventually filled. Grain growth is energetically favourable because the crystal lattice has a lower free energy than the highly defective grain boundary region and for larger grains the ratio of boundary area to volume is smaller. As a result of these processes sintering usually leads to shrinkage in the macroscopic dimensions. Densification during sintering can occur in purely solid phases, by solid state sintering, but the process can be accelerated by the presence of a small amount of liquid phase in which the main phase is soluble, then called liquid phase sintering. In the case of liquid phase sintering transfer of material from grains to pores occurs by diffusion through a solution at the grain boundary which is a more rapid process than diffusion through the solid or along the grain boundaries, as occurs in solid state sintering.

2.4 ZINC AND COBALT GERMANATE

Zinc and cobalt germanate are members of the family of ternary compounds A_xBO_y, where A and B are two different metal atoms and x = 1 or 2, y = 3 or 4. Many of these materials are of scientific and technological interest and have been investigated to establish details of their preparation, physical properties and potential applications, for example; zinc stannate, Zn_2SnO_4[32], cadmium germanate, Cd_2GeO_4[33], copper germanate, $CuGeO_3$[34], and barium stannate, Ba_2SnO_4[35].

2.4.1 PREPARATION OF ZINC AND COBALT GERMANATES

Much of the previous work has concerned the preparation of single crystals of Zn_2GeO_4. These have been produced by vapour growth at temperatures from 1000 to 1200°C, giving various forms of crystals, including ribbons, hexagonal-prisms and whiskers[36,37]. Zn_2GeO_4 crystals have also been formed by hydrothermal crystallisation from alkaline solutions[38-40], by the hydrolysis of zinc and germanium alkoxides[41] and from a melt of germanium dioxide, zinc oxide and cadmium carbonate[42].

Production of Zn_2GeO_4 by solid state reaction was first noted in the course of a study of the behaviour of germanium in the electrolytic production of zinc, where Zn_2GeO_4 was formed by reaction between germanium dioxide, GeO_2, and zinc oxide, ZnO, at 900°C[43].

The phase diagram of GeO_2 - ZnO has been established with Zn_2GeO_4 found to melt at 1450°C[44]. The equilibrium constants have been determined for the formation of zinc germanate by the reaction[45]:

$$2Zn + GeO_2 + 2H_2O \leftrightarrow Zn_2GeO_4 + 2H_2$$

Ceramic Zn_2GeO_4 has been produced by the solid state reaction between ZnO and GeO_2[46,47]. The reaction kinetics of ZnO and GeO_2 have been studied with the highest yields of Zn_2GeO_4 being obtained at temperatures $\geq 1200^{\circ}C$[48]. Formation of Zn_2GeO_4 was found to occur at temperatures of 800-1400°C[46] whilst signs of sintering were observed in powder samples of Zn_2GeO_4 heated at 1000°C[41]. There was a marked increase in grain size from 10 to 40 nm between 600 and 1000°C accompanied by a decrease in specific surface area[41], from 55 to 2 $m^2 g^{-1}$.

Ceramic zinc germanate has been prepared from ZnO and GeO_2, (in the molar ratio 2:1) by calcining at 800-900°C in air for 12 hours, followed by regrinding and sintering at 1200°C in air for 12 hours to produce well sintered pellets, white in colour[47]. Energy dispersive x-ray (EDX) analysis of the pore surfaces suggested an evaporation - condensation mechanism was responsible for compound formation, as has been reported for the related compound zinc stannate, Zn_2SnO_4[32]. This suggestion was supported by the fact that the sintered samples of Zn_2GeO_4 showed a 5% expansion with respect to the pre-sintered samples, which is consistent with an evaporation-condensation model[47].

Ceramic cobalt germanate has been produced by calcination of Co_3O_4 and GeO_2 (in the molar ratio 2:3) at 800-900°C in air for 12 hours followed by regrinding and sintering at 1200°C in air for 12 hours[47]. The resulting as-fired ceramic was deep blue in colour. EDX analysis of the sintered Co_2GeO_4 showed an increase in the Ge to Co ratio at grain boundaries, indicating a mechanism of sintering and grain growth involving the formation of a Ge rich liquid phase, which has also been observed in the related compound cadmium germanate, Cd_2GeO_4[33]. This theory was supported by the fact that the sintered samples showed shrinkage of a few percent with respect to the pre-sintered samples.

2.4.2 STRUCTURE OF ZINC GERMANATE

Zinc germanate has the structure of phenacite, Be_2SiO_4[42,49-53], in common with its silicate analogue, willemite, Zn_2SiO_4[49,54,55]. The phenacite structure has a characteristic hexagonal symmetry ($a = b \neq c$, $\alpha = \beta = 90°$, $\gamma = 120°$), whilst the unit cell is a rhombohedron (with trigonal symmetry; $\alpha = \beta = \gamma < 120° \neq 90°$) which fits within the hexagonal lattice and contains 6 formula units per unit cell[53,56,57]. The phenacite structure is illustrated in Figure 2.3, where the open circles represent the oxygen ions, the shaded circles represent the cations and the dotted lines indicate the unit cell[53].

The crystal structure of Zn_2GeO_4 is described as consisting of MO_4 tetrahedra (M: Zn or Ge) linked to each other by shared corners, with each O atom triply shared by three different tetrahedra, as shown in Figure 2.4[42]. The tetrahedra are arranged around a three-fold axis to form six-membered rings, as shown in Figure 2.5. The inter-atomic distances are Ge-O = 0.174 – 0.178 nm and Zn-O = 0.189 – 0.202 nm[49].

The crystal structure of zinc germanate has been widely reported[36,37,41,42,49,58] and variation in the reported values of the lattice parameters are summarized in Table 3.

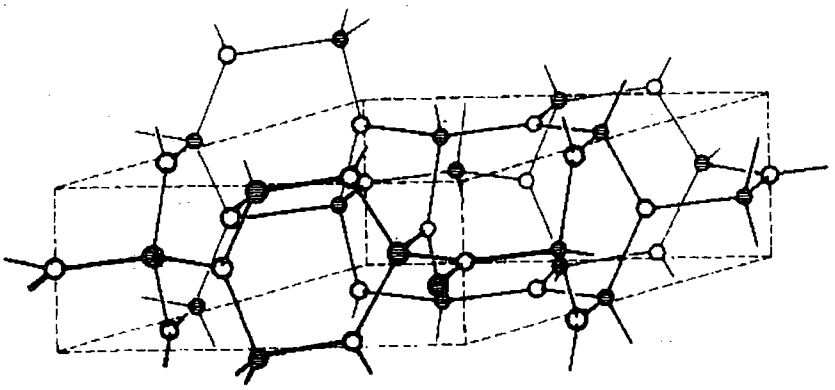

Figure 2.3 - Phenacite structure[51].

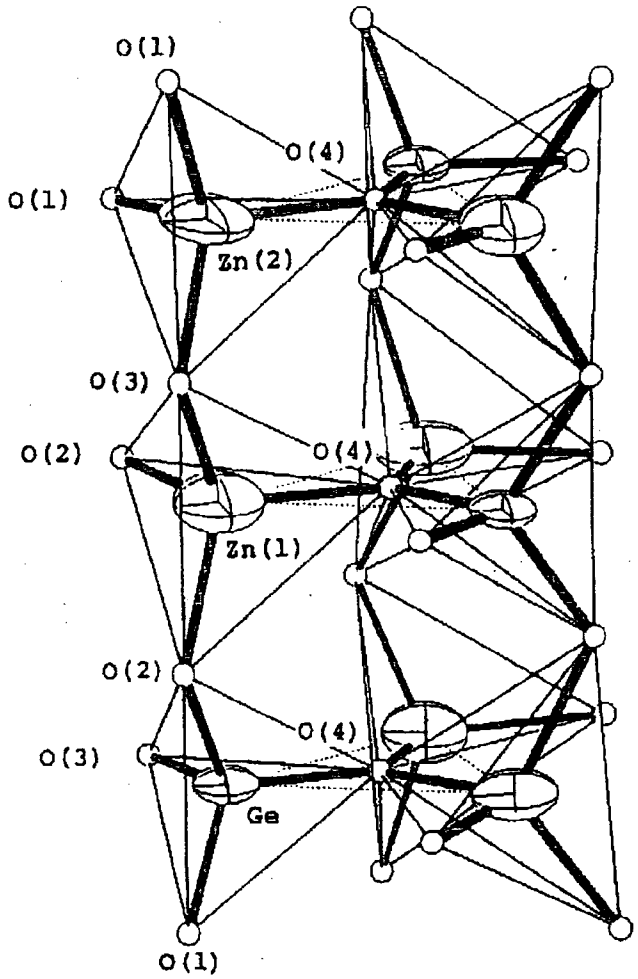

Figure 2.4 - MO_4 in the zinc germanate structure[42]

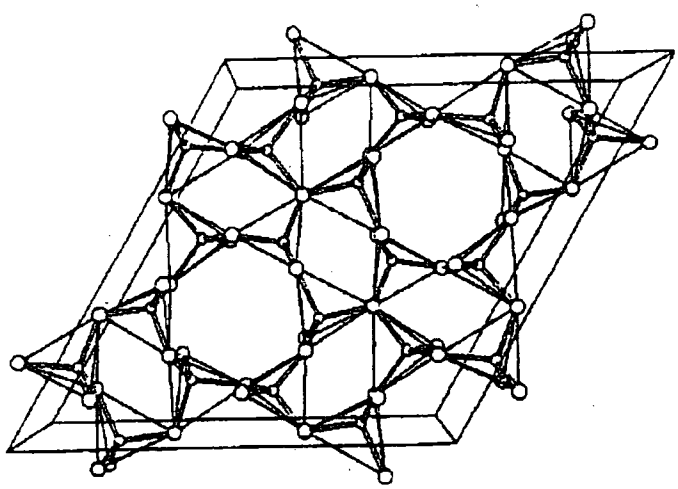

Figure 2.5 - Layer of tetrahedra in the zinc germanate structure[42]

Hexagonal cell parameters		Rhombohedral cell parameters		Reference
a (nm)	c (nm)	a_{rh} (nm)	α	
1.4284	0.9547			42
1.424	0.953			36
1.423	0.952			37
1.427	0.956	0.884	107°42'	49
1.4198	0.9512			41
1.4231	0.953			58

Table 3 - Variation in structural data reported for Zn_2GeO_4.

2.4.3 STRUCTURE OF COBALT GERMANATE

Cobalt germanate has the 'normal' spinel structure[50-53] as do many oxides of the form AB_2O_4[53]. The spinel structure consists of oxygen ions in a cubic close packing arrangement, where the ions are stacked in layers, such that each ion is in contact with six other ions within its layer and three other ions in each of the layers above and below. Within the layers of oxygen ions there are tetrahedral interstices, surrounded by triangular groups of ions, and between the layers there are octahedral interstices, surrounded by polyhedral groups of ions. In a closest packed system of N ions there are 2N of such tetrahedral interstices and N octahedral ones. A spinel unit cell consisting of eight AB_2O_4 formula units contains 32 cubic closest packed oxygen ions

with 64 tetrahedral interstitial sites and 32 octahedral interstitial sites. The unit cell also contains a total of 24 positive ions, of which 8 occupy some of the 64 available tetrahedral interstitial sites and the other 16 occupy half of the available octahedral interstitial sites. In a 'normal' spinel the A ions are in the tetrahedral positions and the B ions are in octahedral positions ($A[B_2]O_4$). This usually happens because the A ions are smaller than the B ions but is also related to the stabilization energies of each ion for particular octahedral or tetrahedral co-ordination[53,59]. In an 'inverse' spinel half of the B atoms occupy tetrahedral positions, whilst the remaining B atoms and the A atoms occupy octahedral positions ($B[AB]O_4$).

The 'normal' spinel structure in illustrated in Figure 2.6[59]. The open circles represent O^{2-} ions, the dark circles represent B^{2+} ions and the A^{4+} ions are located in the centres of the shaded tetrahedra. The structure is made up of B_4O_4 cubes and AO_4 tetrahedra. Hence each A^{4+} ion is in tetrahedral co-ordination with the four O^{2-} ions at the vertices of the tetrahedra and each B^{2+} ion is in octahedral co-ordination with the six O^{2-} ions at the corners of the surrounding cubes. Each B^{2+} ion belongs to two such B_4O_4 cubes, whilst each O^{2-} ion belongs to one B_4O_4 cube and one AO_4 tetrahedra. The cubic unit cell contains eight AO_4 tetrahedra and eight B_4O_4 cubes - a total of 8 formula units.

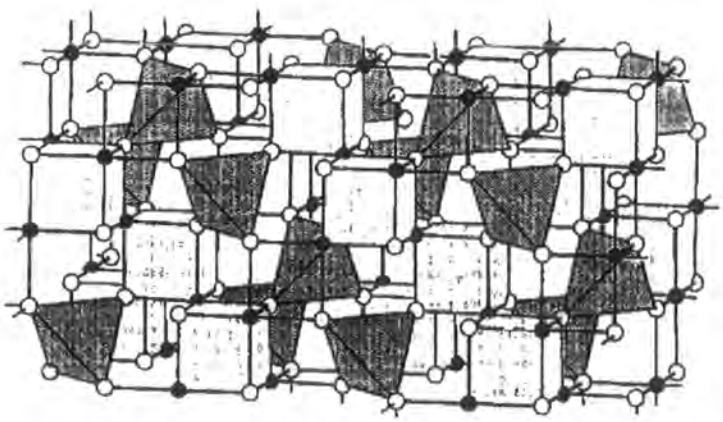

Figure 2.6 - 'Normal' spinel structure[59].

2.4.4 SOLID SOLUTIONS IN THE ZINC-COBALT GERMANATE SYSTEM

Solid solutions within the Co_2GeO_4 - Zn_2GeO_4 system have been discussed in the literature in a number of cases[50-52,60,61]. In the series $Zn_xCo_{2-x}GeO_4$, for x = 0 to 2, there are three solid solution phases, separated by miscibility gaps in which two separate phases occur simultaneously[50-52,61]. These phase regions are illustrated in Figure 2.7. At the Zn_2GeO_4 end, from x ≈ 1.6 to x = 2, is a solid solution phase with a phenacite structure[47,48], denoted Ph in Figure 2.7. The extent of this phase indicates the limit of the solubility of Co_2GeO_4 in Zn_2GeO_4 and this has been found to be 19 mole % at 1050°C[50].

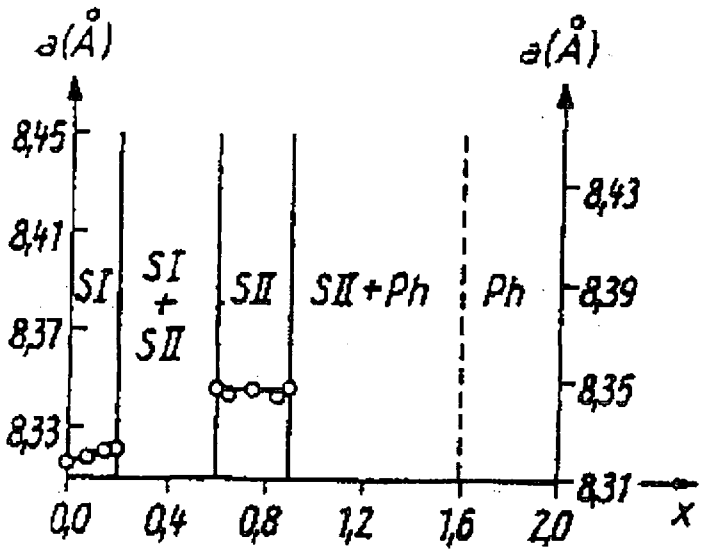

Figure 2.7 - The phases and variation in lattice constants in the system $Co_{2-x}Zn_xGeO_4$[52].

At the Co_2GeO_4 end, from x = 0 to x≈ 0.2, is a spinel solid solution phase[46-48,57], denoted SI in Figure 2.7. Another spinel solid solution phase is formed around x ≈ 0.8, SII in Figure 2.7[46-48,57], which has larger lattice constants than the terminal spinel phase, SI[47,48].

The spinel solid solution phase SI has a normal, cubic spinel structure with the Ge^{4+} ions occupying tetrahedral sites in the crystal lattice and the Co^{2+} and Zn^{2+} ions occupying octahedral sites[51,61]. The spinel solid solution phase, SII, has an inverse spinel structure with the Ge^{4+} ions occupying octahedral sites and the Co^{2+} and Zn^{2+} ions shared between the remaining octahedral sites and the tetrahedral sites[51,61]. This probably accounts for the difference in lattice constants between SI and SII.

The composition range $x \approx 0.2$ to $x \approx 0.7$ is a mixed phase region consisting of both the normal and inverse spinel phases SI and SII. There is a second mixed phase region, from $x \approx 0.9$ to $x \approx 1.6$, consisting of the inverse spinel phase, SII, and the phenacite phase, Ph.

2.4.5 APPLICATIONS OF ZINC AND COBALT GERMANATES

Reported applications for zinc germanate include optical materials, heat resistant materials, lamps, inks and a chromatographic indicator. Both zinc germanate and cobalt germanate have been cited as candidate materials for gas sensors.

Zn_2GeO_4 was investigated among a number of new optical ceramics for potential application in advanced missile sensor windows[62]. Zinc germanate has also been included in a patent for a high density, heat resistant sintered ceramic material prepared from a mixture of carbon, silicon nitride, yttrium oxide, nickel oxide, zinc oxide and germanium dioxide[63].

Zinc germanate has been included in studies of the phosphorescent properties of various ceramic materials[64-71]. It shows efficient luminescence under both ultra violet and cathode ray excitation, with the nature of the luminescence depending strongly on any dopants and the excitation source[64]. The absorption edge of 'pure' Zn_2GeO_4 is situated at about 265nm (hence the white colour of the undoped compound) and the

excitation spectrum consists of one band with a maximum at 260 nm, giving an energy gap of 4.8 eV. The emission band of Zn_2GeO_4 peaks at about 360 nm under cathode-ray excitation, this probably being due to emission from defect-centres. The emission from doped Zn_2GeO_4 is generally blue-green for 254 nm excitation and yellow-green for 365 nm excitation. Results mostly concern the luminescence of Mn-activated Zn_2GeO_4[65-71]. These properties have been utilised in several patented applications, including a phosphor lamp[72], fluorescent ink marker pens[73] and a chromatographic indicator[74].

Both Zn_2GeO_4 and Co_2GeO_4 have potential applications as sensors for reducing or oxidizing gases due to the large increase in electrical conductivity when they are annealed in a reducing atmosphere[47]. As-fired samples of Zn_2GeO_4 and Co_2GeO_4 are electrically insulating, however when annealed in a flow of H_2/N_2 gas at temperatures of 300-450°C the materials become more conducting, with resistances in the range of a few $k\Omega$. The process of reduction also produces a dramatic colour change from white to black in Zn_2GeO_4 and a darkening in colour of Co_2GeO_4. The effect is totally reversible and samples return to their original colour and insulating properties when heated in air. XRD profiles of reduced and as-fired samples were identical, indicating that no phase changes had taken place during reduction. Thus oxidation/reduction could in principle be repeated for an infinite number of cycles, without danger of the build-up of internal stress. The conductivity of reduced samples showed behaviour typical of NTC thermistors[47].

Several related compounds also show potentially useful applications, such as zinc germanium oxynitrides, sodium germanates and a mixture of zinc, cobalt and cadmium germanate.

Semiconducting pellets of zinc germanium oxynitrides can be used to detect ammonia[75,76]. Like most oxides, $Zn_xGeO_yN_z$ is able to ionosorb oxygen. Ammonia is a privileged reducer of germanium oxynitrides, i.e. the reaction of oxygen ionosorbed on the oxynitrides proceeds more easily with ammonia than with other reducing gases

(such as H_2, CO, CH_4, C_4H_{10})[75]. The mechanism of ammonia detection is the decrease in electrical resistance of the $Zn_xGeO_yN_z$ pellets caused by the reducing action of the ammonia on the ionosorbed oxygen[76].

Sodium germanates, $Na_3HGe_7O_{16}.6H_2O$ and $Na_3HGe_7O_{16}.4H_2O$, have potential as conducting electrolytes and humidity sensing materials[77]. These materials exhibit humidity sensing properties in the temperature range 50-120°C. At 50°C the conductivity-humidity characteristics indicate that the mechanism is a mixture of bulk and surface effects whilst at higher temperatures, above 100°C, the conductivity is dominated by surface effects. In the range 50-120°C the charge carriers in the hydrated compounds are protons and H_3O^+ ions whilst at lower temperatures, and in the dehydrated $Na_3HGe_7O_{16}$, sodium ions are the charge carriers.

A mixture of zinc and cadmium germanate with 10% Co_2O_3 has been used in the synthesis of blue pigments for ceramic colours[78].

REFERENCES

[1]E. Traversa, "Ceramic sensors for humidity detection: the state-of-the-art and future developments", Sens. & Act. B, **23**, 135-156 (1995).

[2]J.G. Fagan and V.R.W. Amarakoon, "Reliability and reproducibility of ceramic sensors: part III, humidity sensors", Am. Ceram. Soc. Bull., **72** (3), 119-130 (1993).

[3]N. Yamazoe and Y. Shimizu, "Humidity sensors - principles and applications", Sens. & Act., **10** (3-4), 379-398 (1986).

[4]E. McCafferty and A.C. Zettlemoyer, "Adsorption of water vapour on α-Fe_2O_3", Discuss. Faraday Soc., **52** (239-263) (1971).

[5]W. J. Fleming, "A physical understanding of solid-state humidity sensors", Proc. Int. Auto. Meet., SAE, Detroit, USA, **Paper No. 810432**, 51-62 (1981).

[6]T. Morimoto, M. Nagao, and F. Tokuda, "The relation between the amounts of chemisorbed and physisorbed water on metal oxides", J. Phys. Chem., **73**, 243-248 (1969).

[7]B. M. Kulwicki, "Humidity sensors", J. Am. Ceram. Soc., **74** (4), 697-708 (1991).

[8]J.H. Anderson and G.A. Parks, "The electrical conductivity of silica gel in the presence of adsorbed water", J. Phys. Chem, **72**, 3662-3668 (1968).

[9]P.A. Thiel and T.E. Madey, "The interaction of water with solid surface: fundamental aspects", Surf. Sci. Rep., **17**, 211-385 (1987).

[10]S.L. Yang and J.M. Wu, "ZrO_2 - TiO_2 ceramic humidity sensors", J. Mater. Sci., **26**, 631-636 (1991).

[11]T. Seiyama, N. Yamazoe, and H. Arai, "Ceramic Humidity Sensors", Sens. & Act., **4** (1), 85-96 (1983).

[12]Y. Shimizu, H. Arai, and T. Seiyama, "Theoretical studies on the impedance-humidity characteristics of ceramic humidity sensors", Sens. & Act., **7**, 11-22 (1985).

[13]M. Egashira, M. Nakashima, and S. Kawasumi, "Change of thermal desorption behaviour of adsorbed oxygen with water coadsorption on Ag^+ doped tin (IV) oxide", J .Chem. Soc., Chem Com., 1047-1049 (1981).

[14]S. Mukode and H. Futata, "A semiconductive humidity sensor", Sens. & Act., **16**, 1-11 (1989).

[15]Y-C. Yeh, T-Y. Tseng, and D-A. Chang, "Electrical properties of TiO_2-$K_2Ti_6O_{13}$ porous ceramic humidity sensor", J. Am. Ceram. Soc., **73** (7), 1992-1998 (1990).

[16]Y-C. Yeh, T-Y. Tseng, and D-A. Chang, "Electrical properties of porous titania ceramic humidity sensors", J. Am. Ceram. Soc., **72** (8), 1472-1475 (1989).

[17]T. Nitta, Z. Terada, and S. Hayakawa, "Humidity-sensitive electrical conduction of $MgCr_2O_4$ - TiO_2 porous ceramics", J. Am. Ceram. Soc., **63** (5-6), 295-300 (1980).

[18]G. Gusmano, G. Montesperelli, P. Nunziante and E. Traversa., "Microstructure and electrical-properties of $MgAl_2O_4$ and $MgFe_2O_4$ spinel porous compacts for use in humidity sensors", B. Ceram Trans., **92** (3), 104-108 (1993).

[19]G. Gusmano, G. Montesperelli, P. Nunziante and E. Traversa, "Humidity sensitive electrical response of sintered $MgFe_2O_4$", J. Mater. Sci., **28**, 6195-6198 (1993).

[20]K. Katayama, K. Hasegawa, T. Takahashi, T. Akiba and H Yanagida, "Humidity sensitivity of Nb_2O_5 - doped TiO_2 ceramics", Sens. & Act., **24**, 55-60 (1990).

[21]Y.C. Yeh and T.Y. Tseng, "Humidity-sensitive electrical properties of $Ba_{0.5}Sr_{0.5}TiO_3$ porous ceramics", J. Mater. Sci. Lett., **7**, 766-768 (1988).

[22]H. T. Sun, M. T. Wu, P. Li and X. Yao, "Porosity control of humidity-sensitive ceramics and theoretical-model of humidity-sensitive characteristics", Sens. & Act., **19** (1), 61-70 (1989).

[23]H. T. Sun, C. Cantalini and M. Pelino, "Porosification effect on electroceramic properties", Key Eng. Mater., **115**, 167-180 (1996).

[24]A. J. Moulson and J. M. Herbert, *Electroceramics: Materials, Properties, and Applications* (Chapman and Hall, London, 1990).

[25]Y.C. Yeh and T.Y. Tseng, "Analysis of the D.C. and A.C. properties of K_2O - doped porous $Ba_{0.5}Sr_{0.5}TiO_3$ ceramic humidity sensor", J. Mater. Sci., **24**, 2739-2745 (1989).

[26]N. Ichinose, "Humidity sensitive characteristics of the MO - WO_3 (M = Mg, Zn, Ni, Mn) system", Sens. & Act., **B 13-14**, 100-103 (1993).

[27]Y. Yokomizo, S. Uno, M. Harata and H. Hiraki, "Microstructure and humidity-sensitive properties of $ZnCr_2O_4$ - $LiZnVO_4$ ceramic sensors", Sens. & Act., **4**, 599-606 (1983).

[28]S.S. Pingale, S.F. Patil, M.P. Vinod, G. Pathak and K. Vijayamohanan, "Mechanism of humidity sensing of Ti-doped $MgCr_2O_4$ ceramics", Mater. Chem. Phys., **46**, 72-76 (1996).

[29]H. T. Sun, C. Cantalini, M. Faccio and M. Pelino, "Porous silica-coated α-Fe_2O_3 ceramics for humidity measurement at elevated temperature", J. Am. Ceram. Soc., **79** (4), 927-937 (1996).

[30]T. G. Nenov and S. P. Yordanov, *Ceramic Sensors: Technology and Applications,* (Technomic Publishing A.G., Basel, 1996).

[31]W. D. Kingery, H. K. Bowen and D. R. Uhlmann, *Introduction to Ceramics*, (Wiley, New York, 1976).

[32]T. Hashemi, H.M. Al-Allak, J. Illingsworth, A.W. Brinkman and J. Woods, "Sintering behaviour of zinc stannate", J. Mater. Sci. Lett., **9**, 776-778 (1990).

[33]T. Hashemi, J. Illingsworth, and A.W. Brinkman, "Sintering behaviour and electrical properties of oxidized and electrochemically reduced di-cadmium germanate", J. Mater. Sci. Lett., **9**, 1176-1178 (1990).

[34]T. Hashemi, J. Illingsworth, and A.W. Brinkman, "Sintering and electrical behaviour of copper germanate", J. Mater. Sci. Lett., **11**, 255-256 (1992).

[35]T. Hashemi, D.L. Hales, and A.W. Brinkman, "Preparation, sintering and electrical behaviour of barium stannate", Brit. Ceram. Trans. J., **91**, 150-153 (1992).

[36]S. Ito, N. Yoneda, S. Shimada, A. Tsunahima, K. Kodaira and T. Matsushita, "Vapour growth of Zn_2GeO_4 single crystals", J. Crystal Growth, **47**, 310-312 (1979).

[37]S. Ito, K. Kodaira, and T. Matsushita, Nippon Kagaku Kaishi, **9**, 1372-1375 (1976). *[Japanese, abstract in English]*

[38]I.P. Kuzmina, O.K. Melnikov, and B.N. Litvin, Gidroterm. Sin. Krist., 141-154 (1968). *[Russian, abstract in English]*

[39]I.P. Kuzmina, B.N. Litvin, and V.S. Kurazhkovsakaya, Issled. Protesessov Krist. Gidroterm. Usloviyakh, 164-186 (1970). *[Russian, abstract in English]*

[40]A.A. Ermankov, I. P. Kovalevskaya, A.M. Kalinichenkoand A.I.Perfilev, Neorg. Khim., **27 (5)**, 1174-1178 (1982). *[Russian, abstract in English]*

[41]O Yamaguchi, J. Hidaka, and K. Hirota, "Formation and characterization of alkoxy-derived Zn_2GeO_4", J. Mater. Sci. Lett., **10**, 1471-1474 (1991).

[42]A. Oribe, K. Tanaka, H. Morikawaand F. Marumo "Refinement of the crystal structure of Zn_2GeO_4", Rep. Lab. Eng. Mater., Tokyo Inst. Technol., **12**, 7-12 (1987).

[43]Y. Umetsu and K. Tozawa, Nippon Kogyo Kaishi, **102 (1181)**, 423-429 (1986).*[Japanese, abstract in English]*

[44]O.N. Ustalova, T.I. Koryagina, A.V. Kosov, V.A. Kutvitskii and V.M.Shoriko, Zh. Neorg. Khim., **22 (3)**, 778-82 (1977). *[Russian, abstract in English]*

[45]S.V. Fedorov, V.P. Burkov, E.G. Semin, E.V. Komarov and A.M. Shev-Yakov, Zh. Prikl. Khim., **52 (2)**, 438-439 (1979). *[Russian, abstract in English]*

[46]T.I. Irgashev and N. Rakmanbekov, Dokl. Akad. Nauk USSR, **6**, 34-36 (1985). *[Russian, abstract in English]*

[47]T. Hashemi, A.W. Brinkman, and M.J. Wilson, "Preparation, sintering and electrical behaviour of cobalt, nickel and zinc germanate", J. Mater. Sci., **28**, 2084-2088 (1993).

[48]E.G. Semin, V.P. Zubenko, M.M. Aslanukova and T.I., Zh. Prikl. Khim., **51 (11)**, 2608-2610 (1978). *[Russian, abstract in English]*

[49]H. Chin, M.A. Simonov, and N.V. Belov, "Crystal structures of willemite Zn_2SiO_4 and its germanium analog Zn_2GeO_4", Sov. Phys. - Crystal., **15 (3)**, 387-390 (1970).

[50]A. Navrotsky, "Thermodynamic relations among olivine, spinel, and phenacite structures in silicates and germanates: II. The systems NiO-ZnO-GeO_2 and CoO-ZnO-GeO_2", J. Solid State Chem., **6**, 42-47 (1973).

[51]J. Preudhomme and P Tarte, "Studies of spinels. VII. Order - disorder transition in the inverse germanate spinels $Zn_{2-x}(Co,Ni)_xGeO_4$", J.Solid State Chem., **35**, 272-277 (1980).

[52]V.D. Reinen, Zeitschrift Anorg. Allg. Chem., **356**, 172 (1968). *[German, abstract in English]*

[53]A.F. Wells, *Structural Inorganic Chemistry* (Clarendon, Oxford, 1984).

[54]T. Hahn and W. Eysel, "Solid solubility in the system Zn_2SiO_4 - Zn_2GeO_4 - Be_2SiO_4 - Be_2GeO_4", Neues Jahrb. Mineral. Monatsh, **6**, 263-276 (1970).

[55]E. Ingerson, G.W. Morley, and O.F. Tuttle, "The systems K_2O - ZnO - SiO_2, ZnO - B_2O_3 - SiO_2 and Zn_2SiO_4 - Zn_2GeO_4", Am. J. Sci., **246 (1)**, 31-40 (1948).

[56]W.L. Bragg, "The Structure of Phenacite, Be_2SiO_4.", Proc. Roy. Soc. Lon., **A 113**, 642-657 (1926).

[57]K.W. Andrews, D.J. Dyson, and S.R. Keown, *Interpretation of electron diffraction patterns* (Hilger, London, 1968).

[58]JCPDS card 11-687, Zn_2GeO_4, 1960.

[59]U. Muller, *Inorganic Structural Chemistry* (Wiley, 1992).

[60]A. Navrotsky and A. Muan, "Activity - composition relations in the system CoO - ZnO and NIO - ZnO at 1050°C", J. Inorg. amd Nucl. Chem., **33**, 35-47 (1971).

[61]A. Ohtsuka, K. Hirota, M. Ohtani and N. Mochida, Kenkyu Hokoku - Asahi Garasu Kogyo Gijutsu Shoreikai, **54**, 365-374 (1989). *[Japanese, abstract in English]*

[62]S. Musikant and W.F. Savage, "Advanced optical ceramics for sensor windows", Proc. Photo-Opt. Instrum. Eng., **256**, 27-36 (1980).

[63]Japanese Patent No. 54 033 512 .

[64]G. Blasse and A. Bril, "Observations on the luminescence of some oxides containing post-transition metal ions", Mater. Res. Bull., **5**, 231-242 (1970).

[65]D.T. Palumbo and J.J. Brown, "Electronic states of Mn^{2+} - activated phosphors. I Green - emitting phosphors", J. Electrochem. Soc., **117 (9)**, 1184-1188 (1970).

[66]W.D. Partlow and D.W. Feldman, "Trapping effects in the luminescence of $Zn_2GeO_4 : Mn^{2+}$", J. Luminescence, **6**, 11-20 (1973).

[67]A. Wachtel and C.K. Lui-Wei, "Ge - esperite - a new Mn - activated phosphor.", J. Electrochem. Soc., **118 (8)**, 1373-1375 (1971).

[68]O.Y. Manashirov, V.B. Mikhitaryan, T.I. Savikhina and N.M. Korablev, Sb. Nauchn. Tr.-Vses. Nauchno-Issled. Inst. Lyuminoforov Osobo Chest. Veshchestu, **24**, 126-138 (1983). *[Russian, abstract in English]*

[69]V.A. Krug, Sb. Nauchn. Tr.-Vses. Nauchno-Issled. Inst. Lyuminoforov Osobo Chest. Veshchestu, **24**, 91-97 (1983). *[Russian, abstract in English]*

[70]E.V. Devyatykh, R.S. Zhuravleva, N.F. Kuzmin and I.I. Chertkova, Svetotekhnika, **8**, 13 (1977). *[Russian, abstract in English]*

[71]M.A. Konstantinova-Shlezinger and A.I. Kabakova, Zh. Prikl. Spektrosk., **6 (5)**, 632-636 (1967). *[Russian, abstract in English]*

[72]W.A. Thornton, USA Patent (1974).

[73]T. Ando and Y. Nishiguchi, Japan (1989). *[Japanese, abstract in English]*

[74]Marutoiu, Patent No. 94689 Japan.

[75]M. Ghers, G. Rosse, J. Guyader, Y. Laurent and Y. Colin, "Oxygen ionosorption on compressed semiconducting powders of zinc and germanium oxynitrides (gas sensor application)", Sens. & Act., **13 (3)**, 263-273 (1988).

[76]G. Rosse, M. Ghers, J. Guyader, Y. Laurent and Y. Colin, "Selective detection of ammonia by semiconducting pellets of zinc and germanium oxynitrides", Sens. & Act., **14**, 133-141 (1988).

[77]S. Feng, M. Tsai, and M. Greenblatt, "Preparation, ionic conductivity and humidity-sensing property of novel, crystalline microporous germanates, $Na_3HGe_7O_{16}.xH_2O$, x=0.6-1", Chem. Mater., **4**, 388-393 (1992).

[78]N.A. Sirazhiddinov, T.I. Irgashev, and T.I. Rakhmanbekov, Uzb. Khim. Zh., **6**, 12-15 (1980). *[Russian, abstract in English]*

CHAPTER 3

PRERARATION AND CHARACTERIZATION OF MATERIALS

3.1 INTRODUCTION

The purpose of this chapter is to describe the preparation of zinc and cobalt germanate materials and the investigation of the phases and structural variations in the Zn_2GeO_4 - Co_2GeO_4 system. Firstly monophase Zn_2GeO_4 and Co_2GeO_4 materials were prepared and the materials were identified by x-ray diffraction (XRD) analysis. The formation of solid solution phases in the range Zn_2GeO_4 - Co_2GeO_4 were investigated, the structural changes throughout the solid solution ranges were examined by XRD analysis and the grain structures of the various phases were examined by scanning electron microscopy (SEM) and energy dispersive x-ray (EDX) analysis.

3.2 EXPERIMENTAL METHODS

The ternary oxide compounds Zn_2GeO_4 and Co_2GeO_4 were prepared by conventional ceramic processing methods. Commercially available oxide powders of reagent grade were used as starting materials. These were weighed on an electronic balance to within ± 0.001g and combined in stochiometric proportions according to the molecular weights listed in the CRC Handbook of Chemistry and Physics[1]. Zn_2GeO_4 was prepared from ZnO (99.99 %) and GeO_2 (99.999 %) in the molar ratio 2:1 and Co_2GeO_4 was prepared from Co_3O_4 (99.995 %)and GeO_2 (99.999 %) in the molar ratio 2:3. The solid state reaction is between CoO and GeO_2 but Co_3O_4 was used

instead, since it is commonly believed to decompose to CoO at temperatures above 800°C in air [2] and since Co_3O_4 is less expensive and less toxic than CoO.

If all the Co^{3+} in the Co_3O_4 is turned into Co^{2+} during firing, then Co_2GeO_4 with the normal spinel structure will be formed (See Section 2.4.3). In the normal spinel structure the larger Co^{2+} ions (radii 0.072 nm) are in octahedral sites and the smaller Ge^{4+} ions (radii 0.053 nm) are in tetrahedral sites. If some of the cobalt remains as Co^{3+} then this would require a balancing of charges, either by variation in the oxygen stoichiometry, or by creation of some Ge^{2+} ions. If the cobalt ions go into octahedral sites then this would lead to the smaller Co^{3+} ions (radii 0.063 nm) in the octahedral sites and larger Ge^{2+} ions (radii 0.073 nm) in the tetrahedral sites, making the structure an inverse type spinel. Such variations in the ionic charge species could only be detected by x-ray photoelectron spectroscopy (XPS). Unfortunately this technique was not available. However it is thought to be most likely that the cobalt is all turned to Co^{2+} during firing.

Mixing of the precursor materials was carried out either by ball milling or by grinding in a pestle and mortar. In the first method, a slurry was formed from the powder mixture and de-ionized water which was ball-milled with cylindrical sialon media for approximately 12 hours. The resulting slurry was then dried in an oven to evaporate the water and the residue was ground to powder form in a pestle and mortar. In the second method the initial dry powder was mixed by hand in a pestle and mortar. The first of these two methods produced a more intimate mixture of the two starting materials and a finer particle size due to the crushing effect of the ball milling. Ball milling, however, is time consuming and best suited to large quantities of powder mix (100-200 g). Since smaller amounts of each sample were required (20-30 g) and it was found that the intimacy of mixing and the particle size produced by pestle and mortar mixing was sufficient to prepare monophase, well sintered material, this method was used in most cases.

Some contamination of the material during the mixing process is inevitable, from the materials of the milling media or the pestle and mortar. In the case of ball-milling this contamination is minimized by keeping the milling time as short as possible and by using hard milling media, made of sialon. In the case of mixing by hand, again a hard material, alumina, is used for the pestle and

of sialon. In the case of mixing by hand, again a hard material, alumina, is used for the pestle and mortar. Contamination of the final material was investigated by XRD analysis.

The calcination and sintering stages were carried out in a single firing process. First the powder mixture was formed into disc shaped pellets, 13 mm in diameter and approximately 2-3 mm in thickness, by pressing at approximately 20 kN in a hydraulic press. The pellets were then fired in an air furnace for 12 hours at 1200°C.

Materials containing solid solution phases were prepared in two different ways, either starting with the already sintered monophase ternary oxides or with the precursor oxides. When starting with the ternary oxides the sintered pellets were crushed and ground to a fine powder in a pestle and mortar, then weighed to give the required molecular proportions and mixed thoroughly in a pestle and mortar. The material was then pressed into pellets using a small quantity of poly vinyl alcohol (PVA) binder, since once fired it proved to be too dry to adhere in the green-body form. The new pellets were then re-fired for 12 hours at 1200°C in air. When starting with the precursor oxides these were weighed in the appropriate stoichiometric proportions to give the required ratio of the ternary phases. The oxide powders were then mixed thoroughly in a pestle and mortar, pressed into pellets and fired for 12 hours at 1200°C in air.

XRD analysis was performed to identify the phases present in the samples and to determine the lattice parameters of the phases. It was carried out using a Phillips PW1130 x-ray generator/diffractometer using Co Kα radiation, wavelength 0.17902 nm. The detector was a sealed proportional unit rotating at 1° 2θ per minute. The results were recorded on a chart recorder and analysed using JCPDS (Joint Committee on Powder Diffractometry Studies) data.

The samples for XRD analysis were ground to a fine powder and mounted on glass slides using double sided cellotape. For the precise determination of the position of the diffraction peaks a small amount of CeO_2 was added to the powder sample, to act as an internal standard. The positions of the diffraction peaks were measured using the main diffraction peak of CeO_2, at $2\theta =$

33.3°, as a reference. In this way small variations in the structure of solid solution compositions could be determined.

SEM was used to examine the grain structure of the sintered samples. This technique allows the grain size, porosity, densification and fusion of the grains within the sample to be assessed. The apparatus used was a Cambridge Stereoscan 600 with a Link Systems EDX analysis facility. Magnified images of the grain structure were recorded using a single lens reflex camera mounted on the cathode ray display tube.

EDX analysis was used to examine the distribution of constituent elements throughout the grain structure of the samples. This was run using 860II Analyser software giving results in graphical form of intensity versus x-ray photon energy. For both SEM and EDX analysis the samples were coated with gold by means of sputtering to prevent charging of the samples.

3.3 RESULTS

3.3.1 FORMATION OF TERNARY OXIDES

The ternary oxide materials Zn_2GeO_4 and Co_2GeO_4 were prepared as described. XRD analysis was carried out on the precursor materials and the resulting materials after firing at 1200°C for 12 hours.

Figure 3.1 shows the results of the XRD analysis of (a) the precursor powder mixture, ZnO + GeO_2, and (b) the resulting material after firing. Table 3.1 gives the values of the structural plane indices, hkl, the interplanar spacings, d, the angles of diffraction from each structural plane, 2θ,

and the relative intensities of the diffractions, I / I_1, from the JCPDS data for ZnO, GeO_2 and Zn_2GeO_4[3-5] and the values of 2θ, d and I / I_1 obtained from the results of the XRD analysis. Figure 3.1(a) shows diffraction peaks corresponding to the main structural planes of ZnO and GeO_2 whilst figure 3.1(b) shows diffraction peaks corresponding to the main structural planes of Zn_2GeO_4. This shows that firing at 1200°C has produced monophase Zn_2GeO_4 with no residual precursor materials. No trace of contamination from the mixing media was detected. The sensitivity limit of XRD analysis is approximately 1% for an evenly distributed phase. This indicates that the level of contamination is at least below this detection limit.

Figure 3.2 shows the results of the XRD analysis of (a) the precursor powder mixture, Co_3O_4 + GeO_2, and (b) the resulting material after firing. Table 3.2 gives the structural data from the JCPDS index for Co_3O_4, GeO_2 and Co_2GeO_4[4-6] and the values obtained from the XRD analysis. Figure 3.2 (a) shows diffraction peaks corresponding to the main structural planes of Co_3O_4 and GeO_2 whilst figure 3.2 (b) shows diffraction peaks corresponding to the main structural planes of Co_2GeO_4. This shows that firing at 1200°C has produced monophase Co_2GeO_4 with no residual precursor materials. Again no trace of contamination was detected.

The accuracy of the experimental data with respect to the JCPDS data is $\pm 0.5^\circ$ for values of 2θ and $\pm 5x10^{-4}$ nm for values of d (except for the Zn_2GeO_4 (110) peak where the difference is $3x10^{-3}$ nm). There is some variation in the values of I / I_1 between JCPDS data and experimental results but this could be due to variation in the sensitivity of the diffractometer detector across the 2θ spectrum.

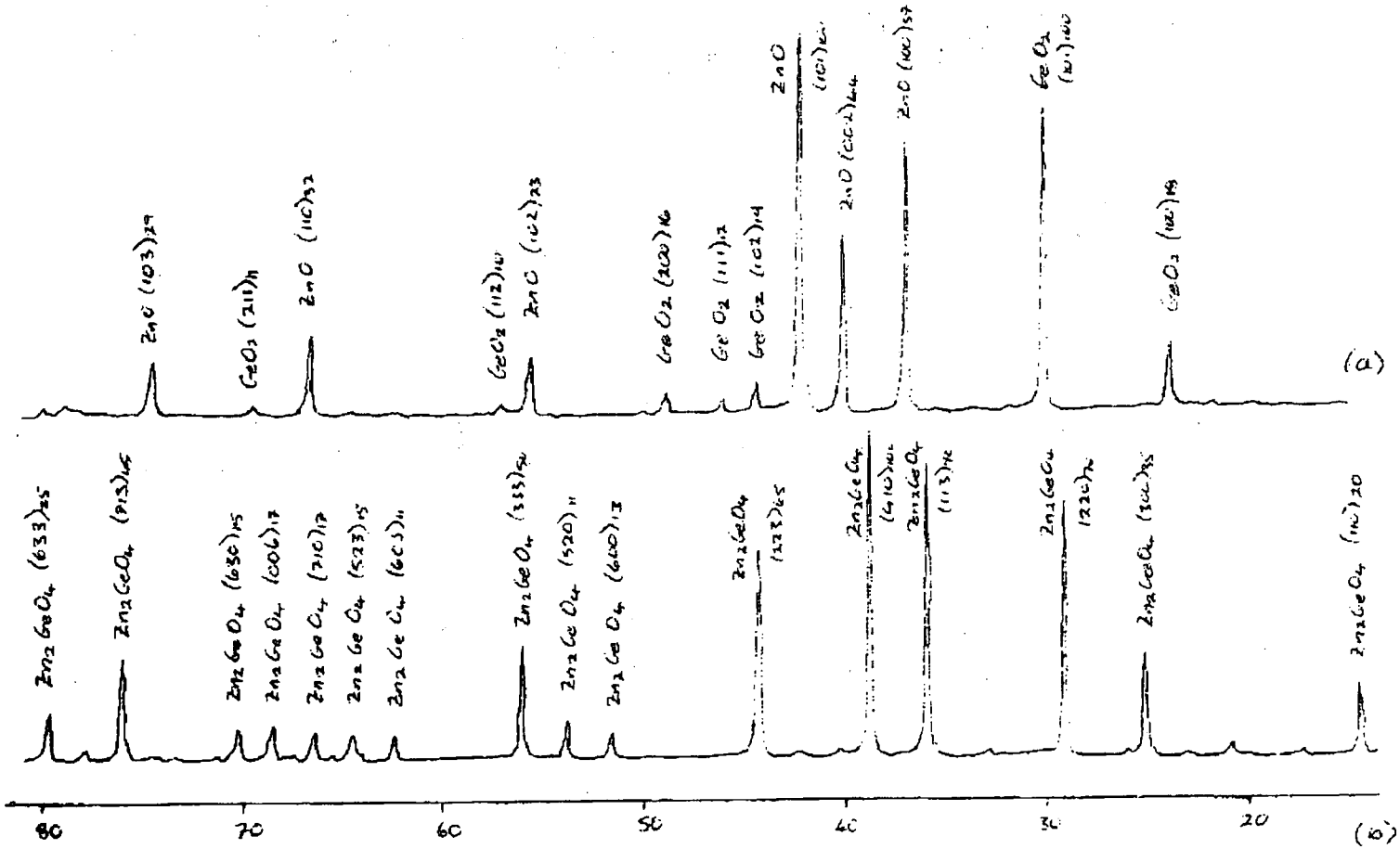

Figure 3.1 - Results of XRD analysis of (a) ZnO and GeO_2 precursor materials and (b) resulting Zn_2GeO_4 after firing at 1200°C.

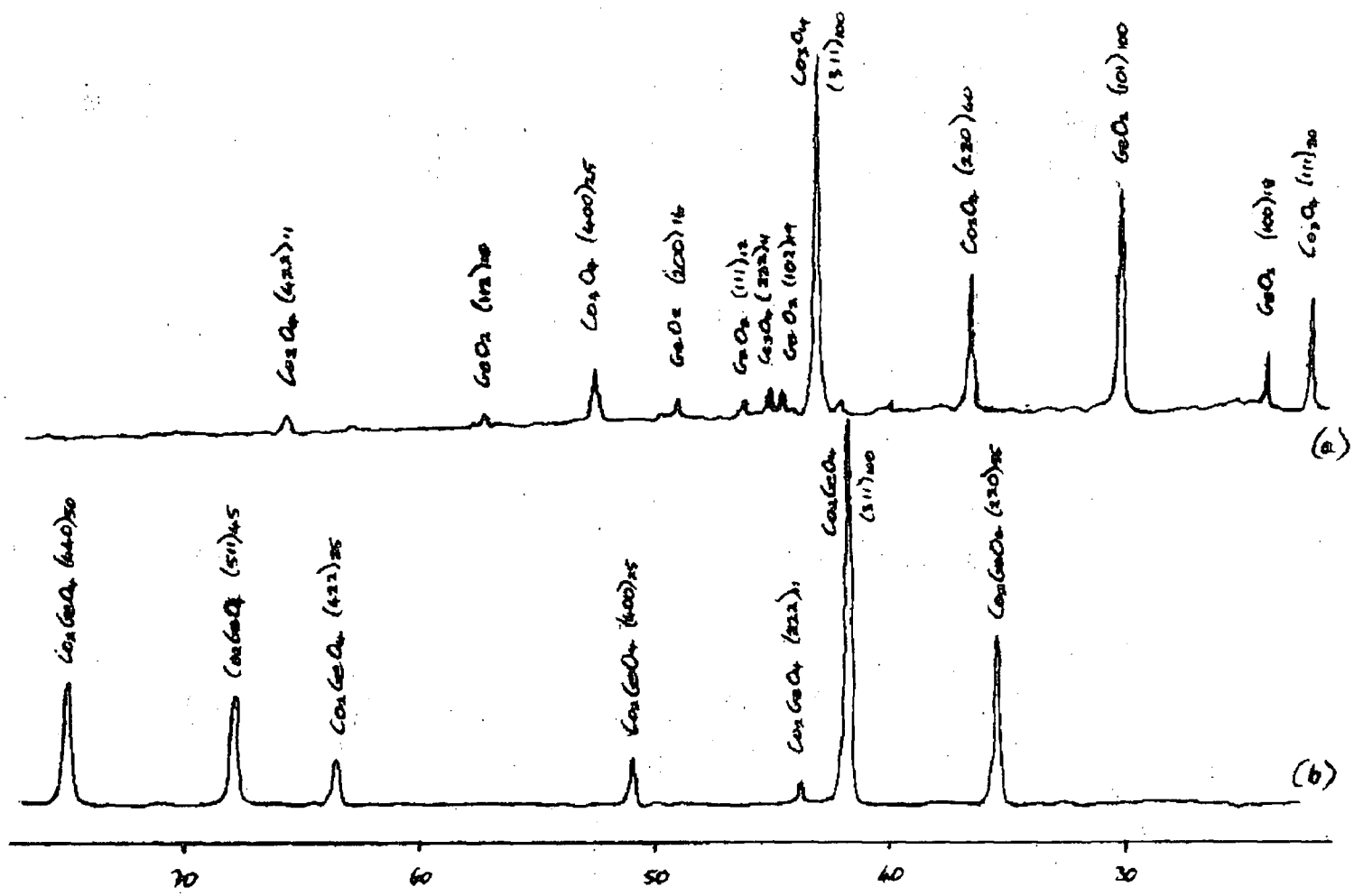

Figure 3.2 - Results of XRD analysis of (a) Co_3O_4 and GeO_2 precursor materials and (b) resulting Co_2GeO_4 after firing at 1200°C.

MATERIAL		JCPDS DATA			EXPERIMENTAL DATA		
	hkl	d (nm)	2θ	I / I_1	2θ	d (nm)	I / I_1
ZnO	100	0.2814	37.1	57	37.0	0.2821	72
	002	0.2603	40.2	44	40.2	0.2605	47
	101	0.24759	42.4	100	42.3	0.2481	100
	102	0.19111	55.9	23	55.7	0.1916	16
	110	0.16247	66.9	32	66.8	0.1626	22
	103	0.14771	74.6	29	74.5	0.1479	15
GeO_2	100	0.43212	23.9	18	23.9	0.4323	22
	101	0.34311	30.3	100	30.3	0.3425	100
	110	0.24930	42.1	10			
	102	0.23634	44.6	19	44.5	0.2364	11
	111	0.22807	46.2	12	46.2	0.2281	5
	200	0.21590	49.0	16	49.0	0.2158	7
	112	0.18687	57.2	10	57.2	0.1870	3
	211	0.15678	69.5	11	69.7	0.1570	2
Zn_2GeO_4	110	0.712	14.4	20	14.5	0.7093	23
	300	0.411	25.2	35	25.2	0.4111	30
	220	0.356	29.1	70	29.1	0.3563	63
	113	0.290	36.0	90	36.0	0.2897	86
	410	0.2689	39.0	100	38.9	0.2688	100
	223	0.2369	44.4	65	44.3	0.2374	51
	600	0.2054	51.7	13	51.6	0.2057	9
	520	0.1974	53.9	11	53.8	0.1978	10
	333	0.1901	56.2	50	56.1	0.1903	30
	603	0.1724	62.6	11	62.4	0.1728	6
	523	0.1676	64.6	15	64.4	0.1680	8
	710	0.1633	66.5	17	66.4	0.1635	8
	006	0.1588	68.6	17	68.5	0.1590	11
	630	0.1553	70.4	15	70.3	0.1555	10
	703	0.1452	76.1	45	76.0	0.1454	32
	633	0.1395	79.8	25	79.7	0.1397	14

Table 3.1 - Structural data from JCPDS index[3-5] and experimental data from XRD analysis for ZnO, GeO_2 and Zn_2GeO_4.

MATERIAL.		JCPDS DATA			EXPERIMENTAL DATA		
	hkl	d (nm)	2θ	I / I_1	2θ	d (nm)	I / I_1
Co_3O_4	111	0.4669	22.2	20	22.1	0.4670	34
	220	0.2860	36.5	40	36.5	0.2858	39
	311	0.2438	43.1	100	43.0	0.2442	100
	222	0.2333	45.1	11	45.1	0.2334	8
	400	0.2021	52.6	25	52.5	0.2024	15
	422	0.16505	65.7	11	65.7	0.1650	4
GeO_2	100	0.43212	23.9	18	23.9	0.4323	22
	101	0.34311	30.3	100	30.3	0.3425	100
	110	0.24930	42.1	10	42.1	0.2492	6
	102	0.23634	44.6	19	44.5	0.2364	11
	111	0.22807	46.2	12	46.2	0.2281	5
	200	0.21590	49.0	16	49.0	0.2158	7
	112	0.18687	57.2	10	57.2	0.1870	3
	211	0.15678	69.5	11	69.7	0.1570	2
Co_2GeO_4	220	0.2940	35.5	55	35.4	0.2944	45
	311	0.2508	41.8	100	41.7	0.2515	100
	222	0.2402	43.8	11	43.7	0.2405	5
	400	0.20792	51.0	25	50.9	0.2083	12
	422	0.16979	63.6	25	63.3	0.1706	12
	511	0.1601	68.0	45	67.7	0.1607	28
	440	0.14706	75.0	50	74.6	0.1477	32

Table 3.2 - Structural data from JCPDS index[4-6] and experimental data from XRD analysis for Co_3O_4, GeO_2 and Co_2GeO_4.

3.3.2 INVESTIGATION OF SOLID SOLUTION PHASES

Samples of $Zn_xCo_{2-x}GeO_4$ of initial compositions x = 0 to 2, were prepared and analysed by XRD to investigate the occurrence of solid solutions in the $Zn_xCo_{2-x}GeO_4$ system. The results of the XRD analysis of samples of compositions x = 1.41 to x = 2 are shown in Figure 3.3. Figure 3.3(a) shows the diffraction profile of a sample of composition x = 2 which corresponds to the diffraction profile of Zn_2GeO_4. The diffraction profile of a sample of composition x = 1.68 showed only diffraction peaks corresponding to Zn_2GeO_4, Figure 3.3(b). The presence of Co in the material was confirmed by EDX analysis and the Co was assumed to be in the form of Co_2GeO_4, forming a solid solution in the Zn_2GeO_4. Although Zn_2GeO_4 and Co_2GeO_4 are structurally dissimilar, being hexagonal and cubic respectively, the Zn^{2+} and Co^{2+} ions are similar in size, 0.074 nm and 0.072 nm respectively[1], so that a limited range of solid solution would be expected. The diffraction profile of a sample of composition x = 1.65 showed a small peak corresponding to the main diffraction from Co_2GeO_4, Figure 3.3(c), indicating that this sample consists of mixed phases. Diffraction profiles of samples with compositions x = 1.52 and x = 1.41 showed increasingly large peaks corresponding to diffractions from various structural planes of Co_2GeO_4, Figures 3.3(d) and (e), indicating that these samples also consist of mixed phases. From this it was determined that a solid solution series is formed from x = 2 to x ≈ 1.68. This corresponds to the phenacite solid solution phase, denoted Ph in Figure 2.7, which occurs for compositions of x = 2 to x ≈ 1.6[7,8], and is in good agreement with the solution limit as found to be 19 mole % Co_2GeO_4 in Zn_2GeO_4 at 1050°C[9].

Figure 3.4 shows the results of XRD analysis of samples of compositions $Zn_xCo_{2-x}GeO_4$ from x = 0 to x = 1.18. Figure 3.4(a) shows the diffraction profile of a sample of composition x = 0 which corresponds to the diffraction profile of Co_2GeO_4. The diffraction profile of a sample of composition x = 0.65 also showed only diffraction peaks corresponding to Co_2GeO_4, Figure 3.4(b). The presence of Zn in the material was confirmed by EDX analysis, suggesting that Zn_2GeO_4 has formed a solid solution in the Co_2GeO_4. The diffraction profile of a sample of composition x = 0.78 showed a small peak corresponding to the main diffraction from Zn_2GeO_4, Figure 3.4(c), indicating that this sample consists of mixed phases. Diffraction profiles of samples

with compositions x = 0.98 and x = 1.18 showed increasingly large peaks corresponding to diffractions from various structural planes of Zn_2GeO_4, Figures 3.4(d) and (e), indicating that these samples also consist of mixed phases. From this it was determined that a solid solution series is formed from x = 0 to between x = 0.65 and x = 0.78. This corresponds to the upper limit of the inverse spinel solid solution phase, SII, at $x \approx 0.9$, shown in Figure 2.7[8].

The results indicate that in the intermediate compositional region, from x = 0.78 to x = 1.68, the material is of mixed phase, consisting of phases with Zn_2GeO_4 and Co_2GeO_4-type structures, as shown by the XRD profiles in Figures 3.3 (c), (d) and (e) and 3.4 (d) and (e). This region is indicated in Figure 2.7 as a mixture of the phenacite phase, Ph, and the inverse spinel phase, SII. The mixed phase region, from x = 0.2 to x = 0.6, between the normal spinel solid solution phase, SI, and the inverse spinel solid solution phase, SII, as shown in Figure 2.7, was not detected because the phases are both cubic with lattice parameters, 0.832 and 0.835 nm respectively and these could not be separated by the resolution of the measuring system.

From the XRD analysis 2θ values were determined for the diffractions from the main structural planes indicated in the profiles in Figures 3.3 and 3.4. The lattice plane spacings corresponding to the 2θ values were obtained from tabulated data and these were used to calculate the lattice parameters for the various compositions in the solid solution ranges, as shown in Table 3.3. The lattice parameters calculated from the XRD data are shown in Figure 3.5 together with values for the lattice parameters from the phase diagram shown in Figure 2.7[8] and from the JCPDS data[5]. Figure 3.5 shows little or no variation in the lattice parameters with composition across either solid solution series and also shows good agreement between the values calculated from the XRD analysis and the published data.

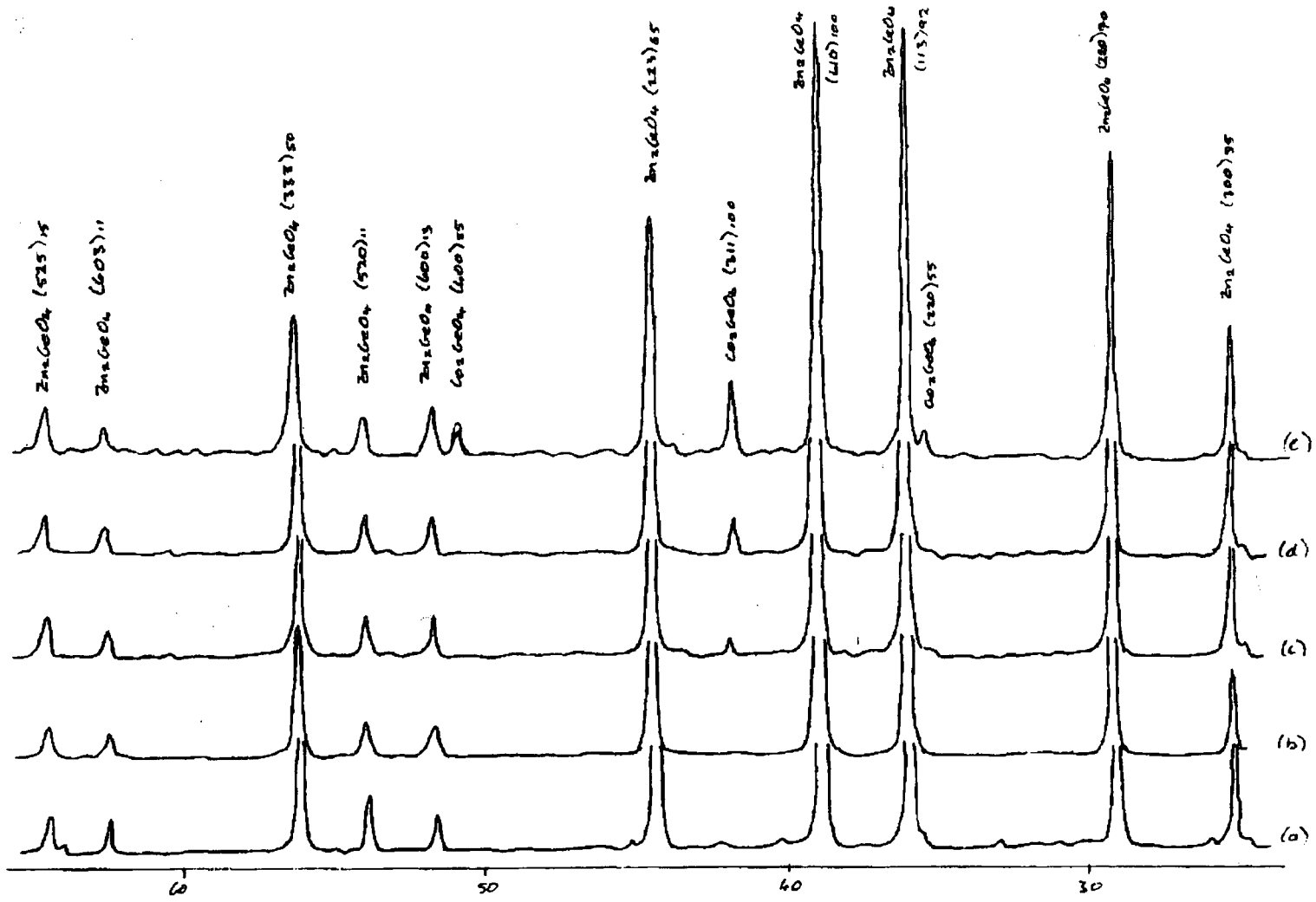

Figure 3.3 - Results of XRD analysis of $Zn_xCo_{2-x}GeO_4$ for x = (a) 2 (b) 1.682 (c) 1.652 (d) 1.52 (e) 1.408.

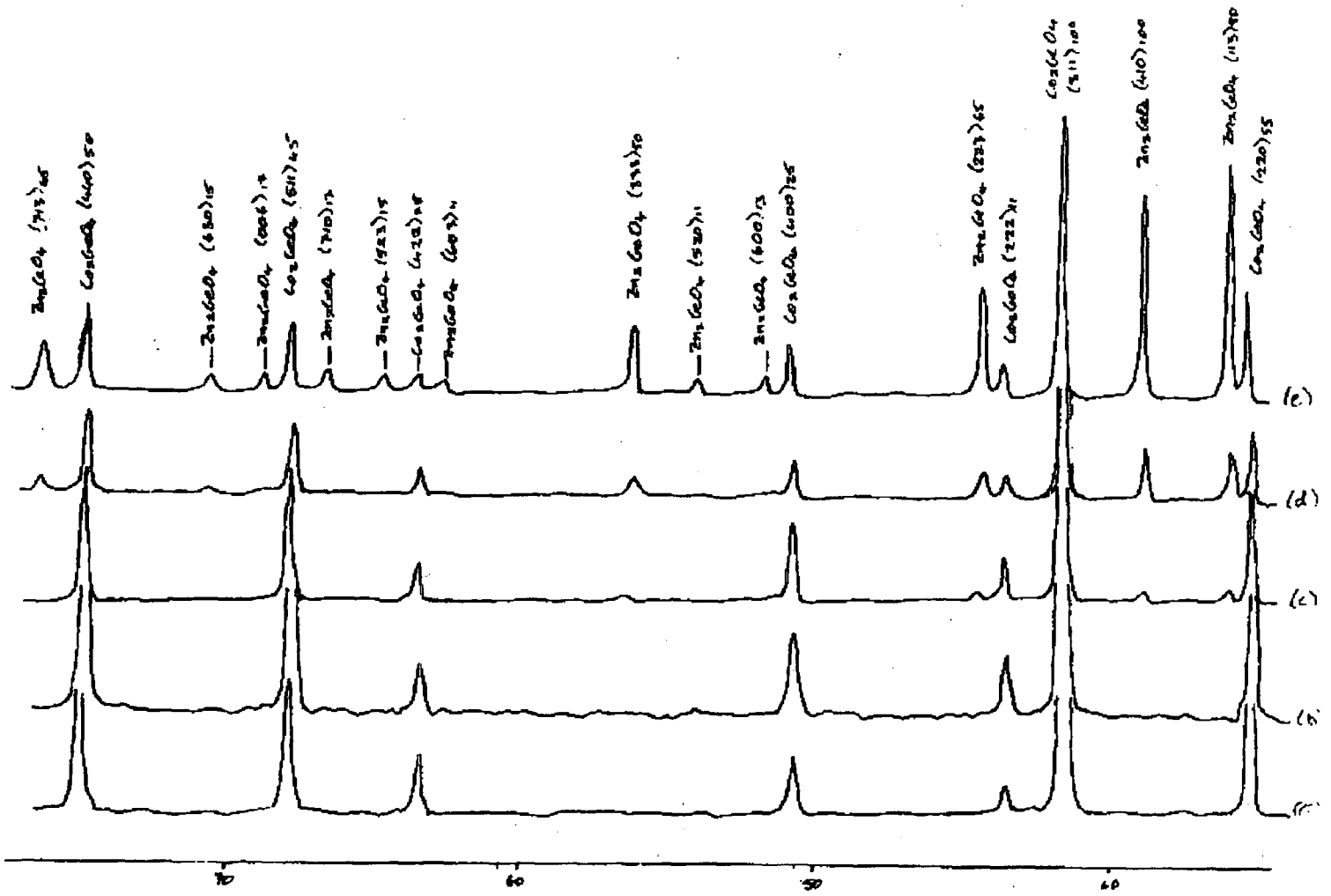

Figure 3.4 - Results of XRD analysis of $Zn_xCo_{2-x}GeO_4$ for x = (a) 0 (b) 0.646 (c) 0.776 (d) 0.976 (e) 1.176.

Table 3.3 - Calculation of Lattice Parameters and Theoretical Densities.

COMPOSITION $Zn_xCo_{2-x}GeO_4$ x	STRUCTURE	hkl	d (nm)[I]	a (nm)[II]	$\bar{a}$ (nm)	c (nm)[II]	$\bar{c}$ (nm)	VOLUME OF UNIT CELL (m^3) [III]	NO. MOLECULES IN UNIT CELL [IV]	MASS OF MOLECULES IN UNIT CELL (kg)[V]	DENSITY ($kg\ m^{-3}$)
0	cubic	220	0.2944	0.8327							
		311	0.2515	0.8341							
		222	0.2405	0.8331							
		400	0.2083	0.8332							
		422	0.1706	0.8358							
		511	0.1607	0.8350	0.834				8 x Co_2GeO_4		
		440	0.1477	0.8355	±.001			5.805×10^{-28}		$= 3.3814 \times 10^{-24}$	5.825×10^3
0.25	cubic	220	0.2944	0.8327							
		311	0.2515	0.8341							
		222	0.240	0.8314							
		400	0.2083	0.8332					8 x [0.25Zn +		
		422	0.1703	0.8343	0.834				1.75Co +		
		511	0.1607	0.8350	±.001				Ge + 4O]		
		440	0.1475	0.8344				5.793×10^{-28}		$= 3.4017 \times 10^{-24}$	5.872×10^3
0.6	cubic	220	0.2952	0.8350							
		311	0.2521	0.8361							
		222	0.2405	0.8331							
		400	0.2087	0.8348					8 x [0.6Zn +		
		422	0.1706	0.8358					1.4Co +		
		511	0.1609	0.8361	0.835				Ge + 4O]		
		440	0.1480	0.8372	±.001			5.830×10^{-28}		$= 3.4317 \times 10^{-24}$	5.886×10^3

Table 3.3 - Calculation of Lattice Parameters and Theoretical Densities (continued)

COMPOSITION $Zn_xCo_{2-x}GeO_4$ x	STRUCTURE	hkl	d (nm)[I]	a (nm)[II]	$\bar{a}$ (nm)	c (nm)[II]	$\bar{c}$ (nm)	VOLUME OF UNIT CELL (m^3) [III]	NO. MOLECULES IN UNIT CELL [IV]	MASS OF MOLECULES IN UNIT CELL (kg)[V]	DENSITY (k gm^{-3})
1.652	Hexagonal	110	0.71402	1.4284							
		300	0.4119	1.4269							
		220	0.3563	1.4252							
		113	0.2904			0.9539			6x [1.652Zn		
		410	0.2688	1.4224					+ 0.348Co +		
		223	0.2374		1.426	0.9548	0.956		Ge + 4O]		
		333	0.1907		±.002	0.9590	±.002	$5.609x10^{-28}$		$= 2.6413x10^{-24}$	$4.709x10^3$
1.81	Hexagonal	110	0.7093	1.4186							
		300	0.4103	1.4213							
		220	0.3557	1.4223							
		113	0.2897			0.9518			6x [1.81Zn +		
		410	0.2688	1.4224					0.19Co +		
		223	0.2369		1.421	0.9536	0.955		Ge + 4O]		
		333	0.1903		±.002	0.9588	±.003	$5.567x10^{-28}$		$= 2.6515x10^{-24}$	$4.763x10^3$
2	Hexagonal	110	0.7093	1.4186							
		300	0.4111	1.4241							
		220	0.3563	1.4252							
		113	0.2897			0.9516					
		410	0.2688	1.4224							
		223	0.2374		1.422	0.9567	0.955		6 x Zn_2GeO_4		
		333	0.1903		±.003	0.9575	±.003	$5.579x10^{-28}$		$= 2.6646x10^{-24}$	$4.776x10^3$

Table 3.3 - Calculation of Lattice Parameters and Theoretical Densities. (continued)

I From tabulated values corresponding to values of 2 θ from XRD analysis.

II For a cubic structure[10], $d_{hkl} = \frac{a}{\sqrt{h^2 + k^2 + l^2}} \Rightarrow a = d_{hkl}\sqrt{h^2 + k^2 + l^2}$

II For a hexagonal or trigonal structure[10], $\frac{1}{d_{hkl}} = \frac{4(h^2 + hk + k^2)}{3a^2} + \frac{l^2}{c^2}$ $\Rightarrow$ for ($h\,k\,0$) planes, $a = \sqrt{\frac{4d_{hkl}(h^2 + hk + k^2)}{3}}$

& for ($h\,k\,l$) planes, $c = \sqrt{\frac{l^2}{\left(\frac{1}{d_{hkl}} - \frac{4(h^2 + hk + k^2)}{3a^2}\right)}}$

III For a cubic structure, volume of unit cell = a^3. For a hexagonal or trigonal structure, volume of unit cell = $a^2.c.\sin 60°$.
Volume of rhombohedral unit cell = 1/3 volume of the hexagonal unit cell. (Certain trigonal crystal structures, such as Zn_2GeO_4, may be referred to rhombohedral axes with the rhombohedral unit cell defined by a cell edge and an interaxial angle)[11]

IV The spinel unit cell contains 8 formula units[11,12]. The phenacite unit cell contains 6 formula units[13].

V Calculated from atomic weights, according to the CRC Handbook of Physics and Chemistry[1]

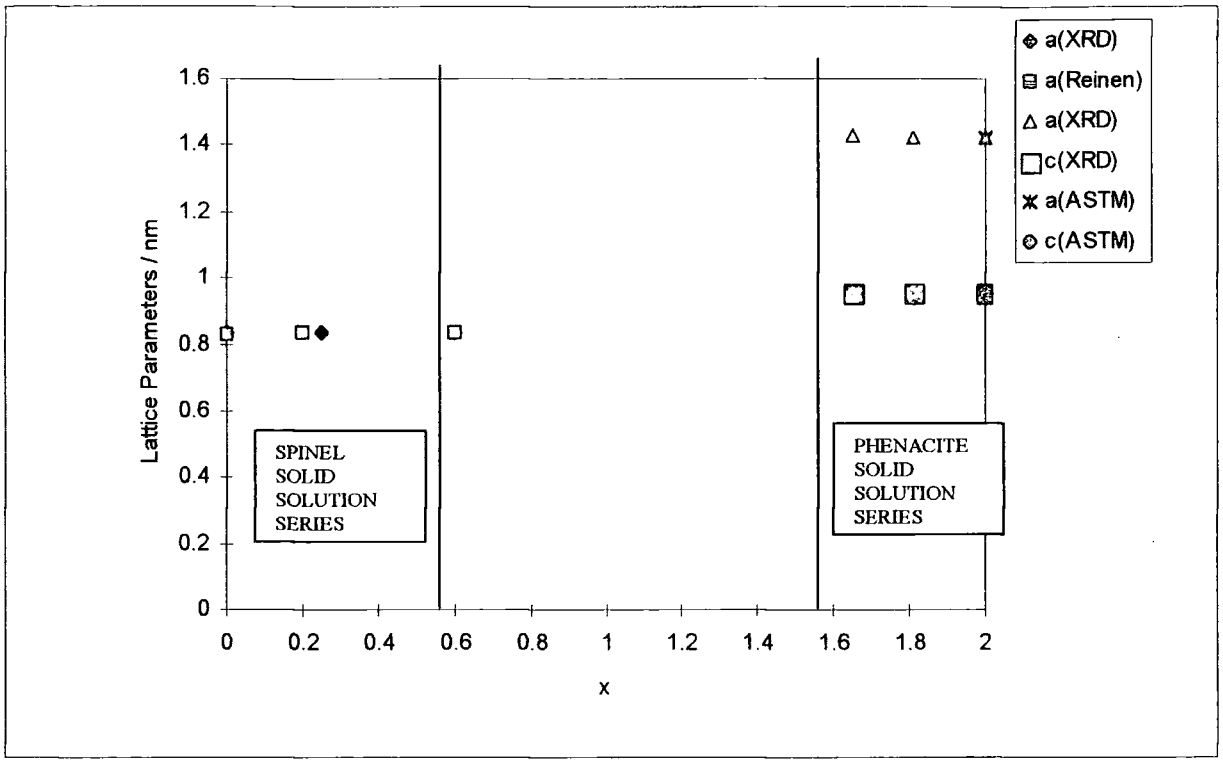

Figure 3.5 - Lattice Parameters versus composition for solid solution series, as calculated from XRD data, according to Reinen[8] and according to JCPDS data[5].

3.3.3 POROSITY

The theoretical densities of the materials were calculated from the experimentally determined lattice parameters, as shown in Tables 3.3. Figure 3.6 shows a graph of the variation of the theoretical densities with composition for the solid solution phases in the Zn_2GeO_4 - Co_2GeO_4 system.

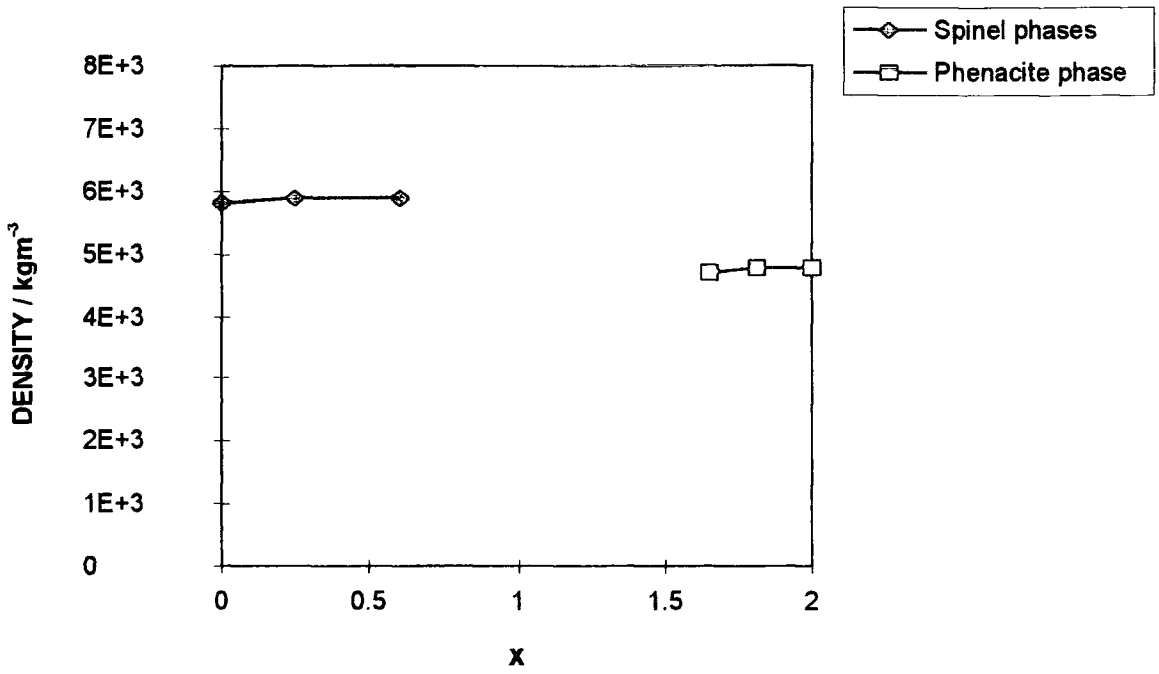

Figure 3.6 - Theoretical density versus composition for solid solution phases in the $Zn_xCo_{2-x}GeO_4$ system.

The apparent densities of the samples were measured by geometric means. Figure 3.7 shows the variation in the apparent geometric density with composition, measured in kg m^{-3} and as a percentage of the theoretical density. For compositions near the Zn_2GeO_4 end the apparent densities ranged from 47 to 50% of theoretical density and near the Co_2GeO_4 end from 57 to 52%. The percentage of theoretical density increases with increasing Co_2GeO_4 content and this is thought to be due to the liquid phase sintering mechanism, which has been found to occur in Co2GeO4 as opposed to the evaporation-condensation mechanism, found to occur in Zn_2GeO_4[14]. The percentage of theoretical density gives a good measure of the porosity of the samples. In this case porosity varies almost linearly from 53% for Zn_2GeO_4 to 43% for Co_2GeO_4.

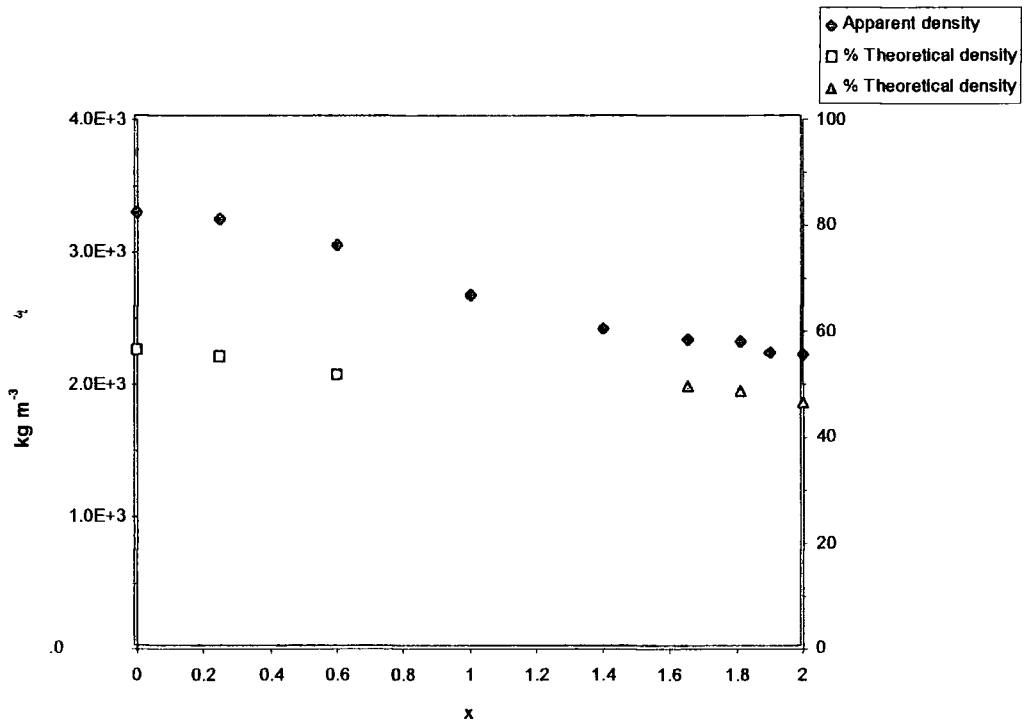

Figure 3.7 - Apparent density versus composition for $Zn_xCo_{2-x}GeO_4$ in kg m^{-3} and as a percentage of theoretical density.

3.3.4 MICROSTRUCTURE

The electron micrograph in Figure 3.8(a) shows the typical grain structure of a sample of composition x = 0.6, which is a single solid solution phase with composition towards the limit of the spinel solid solution series. The grains vary in size with diameters of between 5 and 20 μ m and are prismatic with a visible terracing, indicative of an evaporation process, as is known to occur in the sintering of Zn_2GeO_4[14]. EDX analysis showed no variation in the Zn/Co ratio between grains.

Figure 3.8(b) shows an electron micrograph of a sample of composition x =.1.18. This is a mixed phase material, consisting of both Co_2GeO_4 and Zn_2GeO_4. The material appears to show greater fusion between grains than in the previous sample, with grains varying in diameter from 5 to 40 μ m. EDX analysis shows the larger grains to have a higher Zn/Co ratio than the smaller grains, as is illustrated in Figure 3.9. This could be due to the fact that Zn_2GeO_4 undergoes an evaporation/condensation sintering mechanism, as opposed to the liquid phase sintering mechanism undergone by Co_2GeO_4[14] and the fact that the rate of evaporation from smaller grains is greater than from larger grains. The result is that more Zn_2GeO_4 will be lost during sintering by evaporation from smaller grains than from larger grains, whereas the amount of Co_2GeO_4 will remain the same in grains of all sizes, since it does not undergo evaporation during the sintering mechanism.

Figure 3.8(c) shows an electron micrograph of a sample of composition x = 1.68, which is a single solid solution phase material towards the upper limit of the Zn_2GeO_4 end solid solution series. The grains are more even in size than in the previous two samples with diameters from 5 to 15 μ m. EDX analysis showed no variation in the Zn/Co ratio between grains.

The results of the SEM and EDX analysis indicate that the single phase solid solution materials have an even distribution of zinc and cobalt whereas the mixed phase samples have areas or grains where the ratio of Zn_2GeO_4 to Co_2GeO_4 varies, probably due to varying evaporation rates from different grain sizes.

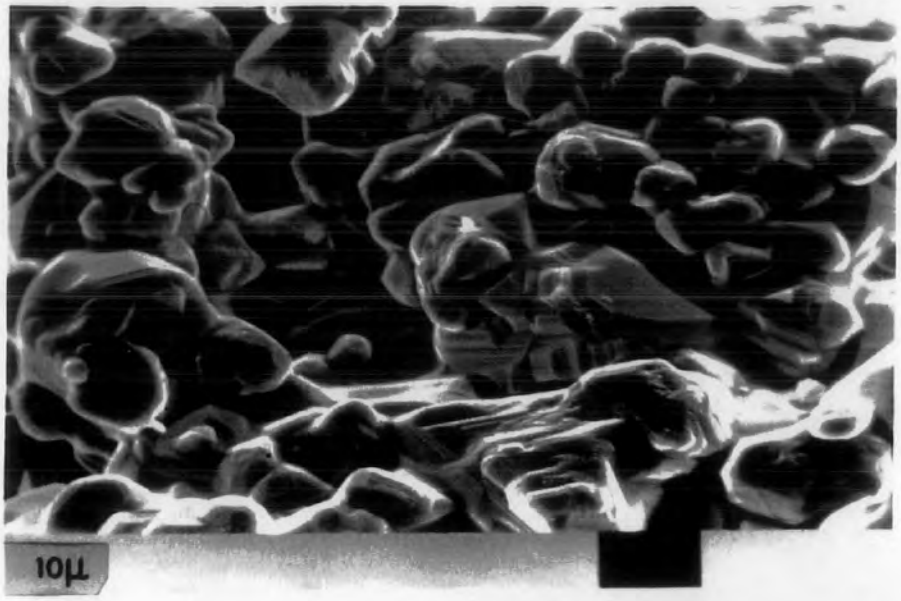

(a)

(b)

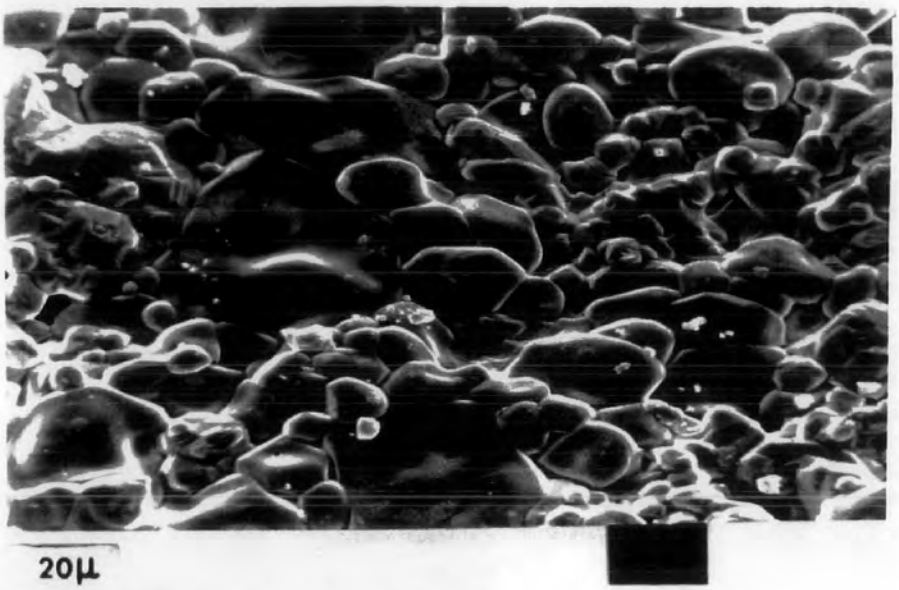

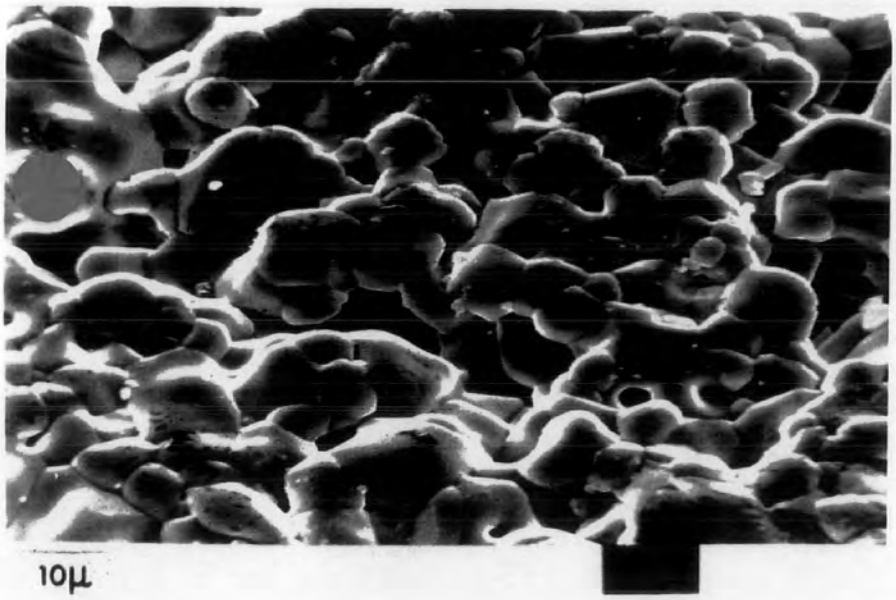

(c)

Figure 3.8 - SE micrographs of samples of composition x = (a) 0.6 (b) 1.18 (c) 1.68.

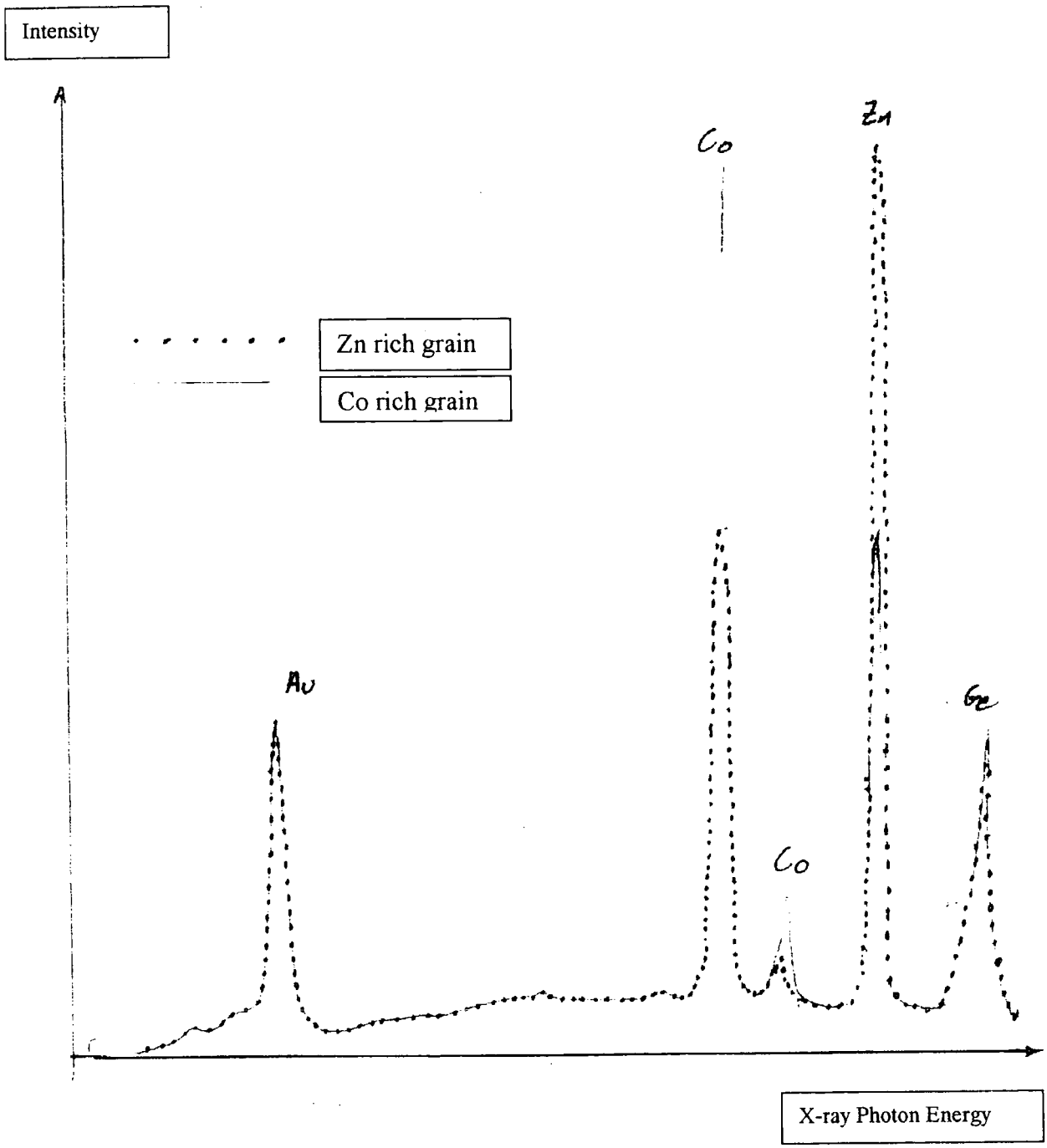

Figure 3.9 - EDX analysis of sample of composition x = 1.18.

3.4 SUMMARY

The formation of the monophase ternary oxide materials Zn_2GeO_4 and Co_2GeO_4 from the precursor oxides fired at 1200°C was confirmed by XRD analysis.

Two solid solution phases were identified in the $Zn_xCo_{2-x}GeO_4$ system. At the Zn_2GeO_4 end of the compositional range a solid solution phase was found to extend from x = 2 to $x \approx 1.68$, for material fired at 1200°C. This corresponds to the solid solution phase, with phenacite structure, known to occur from x = 2 to x = 1.6, as shown in Figure 2.7[7,8], and is in good agreement with the solution limit of 19 mole % Co_2GeO_4 in Zn_2GeO_4 at 1050°C established by Navrotsky[9]. At the Co_2GeO_4 end of the compositional range a solid solution series was detected from x = 0 to x between 0.65 and 0.78, for material fired at 1200°C. This corresponds to the upper limit of the inverse spinel solid solution phase, SII, as shown in Figure 2.7[8]. In fact this compositional range spans two solid solution series, a normal spinel solid solution phase, SI, from x = 0 to x = 0.2, and the inverse spinel solid solution phase, SII, from x = 0.6 to x = 0.9 and also a mixed phase region, from x = 0.2 to x = 0.6, consisting of both SI and SII, as shown in Figure 2.7. The two separate phases, SI and SII, were not detected because they are both cubic in structure and the difference in their lattice parameters, 0.832 nm and 0.835 nm respectively, was too small for the resolution of the measuring system.

There is little or no variation in the lattice parameters with composition across either of the solid solution series, as shown by the values calculated form the XRD analysis and by the published data[5,8].

The percentage of theoretical density increased with increasing Co_2GeO_4 content, from 47% for Zn_2GeO_4 to 57% for Co_2GeO_4. This is thought to be due to the liquid phase sintering mechanism, which has been found to occur in Co_2GeO_4, as opposed to the evaporation-condensation mechanism, found to occur in Zn_2GeO_4[14]. The percentage of theoretical density was taken as a measure of the porosity of the samples, giving a range from 53% for Zn_2GeO_4 to 43% for

Co_2GeO_4. These values however represent total porosity, which includes both open and closed pores, whereas only open pores are effective in the process of humidity sensing.

The single phase solid solution materials showed an even distribution of zinc and cobalt throughout the material whereas the mixed phase samples showed variation in Zn/Co ratio.

REFERENCES

[1]R. C. Weast, *CRC Handbook of Chemistry & Physics*, (CRC Press, Florida, 1990).

[2]A. Navrosky, *Inorganic Chemistry Series* (Butterworths, London, 1974).

[3]JCPDS card 36-1451, ZnO, 1986.

[4]JCPDS card 36-1463, GeO_2, 1986.

[5]JCPDS card 11-687, Zn_2GeO_4, 1960.

[6]JCPDS card 9-418, Co_3O_4, 1959.

[7]J. Preudhomme and P Tarte, "Studies of spinels. VII. Order - disorder transition in the inverse germanate spinels $Zn_{2-x}(Co,Ni)_xGeO_4$", J.Solid State Chem., **35**, 272-277 (1980).

[8]V.D. Reinen, Zeitschrift Anorg. Allg. Chem., **356**, 172 (1968).

[9]A. Navrotsky, "Thermodynamic relations among olivine, spinel, and phenacite structures in silicates and germanates: II. The systems NiO-ZnO-GeO_2 and CoO-ZnO-GeO_2", J. Solid State Chem., **6**, 42-47 (1973).

[10]K.W. Andrews, D.J. Dyson, and S.R. Keown, *Interpretation of electron diffraction patterns* (Hilger, London, 1968).

[11]A.F. Wells, *Structural Inorganic Chemistry* (Clarendon, Oxford, 1984).

[12]U. Muller, *Inorganic Structural Chemistry* (Wiley, 1992).

[13]W.L. Bragg, "The Structure of Phenacite, Be_2SiO_4.", Proc. Roy. Soc. Lon., **A 113**, 642-657 (1926).

CHAPTER 4

DC ELECTRICAL CHARACTERIZATION

4.1 INTRODUCTION

DC electrical measurements were conducted to investigate the humidity-resistivity characteristics of the zinc-cobalt germanate materials. The nature of the humidity dependent conduction carriers was determined and the resistivity characteristics of various compositions of zinc-cobalt germanate were measured for a variety of conditions of humidity and temperature.

4.2 EXPERIMENTAL TECHNIQUES

Zinc-cobalt germanate samples of composition $Zn_xCo_{2-x}GeO_4$, for various values of x, were prepared as described in chapter 3. The samples were in the form of disc-shaped pellets, 11.9 to 14.3 mm in diameter and 2.0 to 2.77 mm in thickness. (Dimensions varied due to differences in density with composition and due to variation in the amount of powder material used to form each pellet.) Gallium - indium alloy electrical contacts were applied to the discs in two strips on one side at a separation of approximately 5mm. Gallium - indium has a low work function, 4.2 eV[1], giving a good ohmic contact to materials which are n-type and thus have a higher electron affinity than the GaIn[1,2]. Surface states occur in ceramic materials due to the electrons in the surface atoms occupying localized energy states, different to those of the interior of the material, due to the interruption of the crystal lattice at grain boundaries and other localized energy states

surface adsorbed species. To form a good ohmic contact with the ceramic the electrode material must be able to disrupt these surface states and the high oxygen affinity of GaIn enables it to do this[1,2].

The charging characteristics of the samples were measured in order to determine the nature of the charge carriers. A potential difference of 1 V was applied to the sample and the resulting variation in current was measured over time. This was repeated at various conditions of humidity.

DC resistance-humidity characteristics of samples of $Zn_xCo_{2-x}GeO_4$, of compositions across the full range from x = 0 to 2, including samples of compositions from within both solid solution series and samples of mixed phases, were measured at various temperatures. The measurements were carried out inside a Heraeus Votsch HC4020 Climatic Test Chamber. The range of operating conditions of the chamber are shown in Figure 4.1. For most temperatures in the range 10 to 90°C the humidity is variable from 10 to 98 % *r.h.* and is measured by a dew point method to an accuracy of ± 3 %, Region 1 in Figure 4.1. At low temperatures and low humidities, below 40°C and 70% *r.h.*, additional dehumidification is required in the operation of the chamber and the accuracy of the humidity measurement is ± 4 %, Region 2 in Figure 4.1. At high humidities and the extremes of the temperature range, above 85% *r.h.*, above 60°C and above 90% *r.h.*, below 35°C, a capacitive system is used for humidity measurements, with an accuracy of ± 3 %, Regions 3 and 4 in Figure 4.1.

The temperature was varied across the full range, from 10 to 90°C, at intervals of 10°C. The humidity was similarly cycled from 10 to 98% *r.h.* in increments of approximately 10% *r.h.* After each change in the temperature and/or humidity conditions the system was allowed to equilibrate for 30 minutes before measurements were made. Two point resistance measurements were made using a Keithley digital multimeter in resistance mode, which applies a certain voltage, up to 100V, from an internal power supply, to give a fixed current. Each measurement was taken 30s after the voltage was applied.

The resistance measurements from the various samples were normalized for variations in the dimensions of the samples and the separation of the electrodes. Apparent resistivities were calculated from the measured values of resistance according to the equation:

$$\rho = \frac{RA}{l} \tag{4.1}$$

where ρ is resistivity, R is resistance, l is the separation of the contacts and A is the cross-sectional area of the sample between the contacts. This assumes that the material is solid, i.e. it does not take into account the porosity of the material. It also assumes that the entire thickness of the sample is effective in conduction, whereas with the electrode configuration used conduction will mainly occur in the surface layer between the contacts.

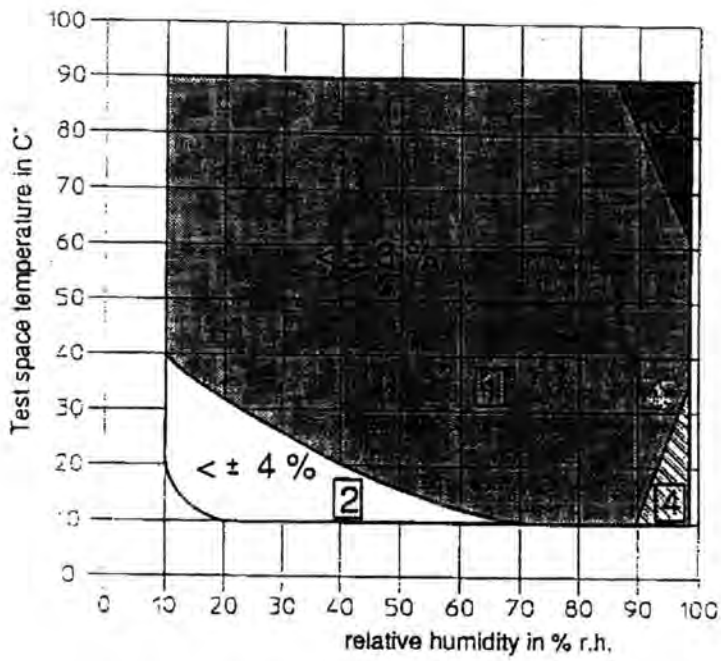

1 Normal operation, dew point control.

2 Additional dehumidification, dew point control.

3 & 4 Normal operation, capacitive humidity measuring system.

Figure 4.1 - Operating Humidity ranges of the Heraeus Votsch HC4020 Climatic Test Chamber.

4.3 RESULTS

4.3.1 CHARGING CHARACTERISTICS

The nature of the charge carriers in a material can be determined from its charging characteristics[4,5]. If the charge carriers are ions then, on the application of a potential difference, a large current will flow initially, then as the material becomes polarized the charging current will decay exponentially to zero. Conversely if the charge carriers are electrons then no charging occurs and the current will be constant.

The charging currents were measured for samples of various compositions of $Zn_xCo_{2-x}GeO_4$. The charging currents in all samples were found to decrease rapidly in the first few seconds, then to decay more slowly over a period of tens of minutes and to reach a steady state value after about 40 minutes. The values of charging current were greater with higher relative humidity at all time intervals. Figure 4.2 shows the typical charging characteristics at room temperature and humidities of 65, 85 and 95% *r.h.*, in this case for a sample of composition x = 0.1.

The charging currents in $Zn_xCo_{2-x}GeO_4$ did not decrease in a simple exponential manner and did not decay to zero. It was concluded that the charge carriers were both ions and electrons. Other ceramic oxide materials are known to exhibit both ionic and electronic humidity dependent conduction, such as TiO_2 - $K_2Ti_{16}O_{13}$[4] and $Ba_{0.5}Sr_{0.5}TiO_3$[4-6].

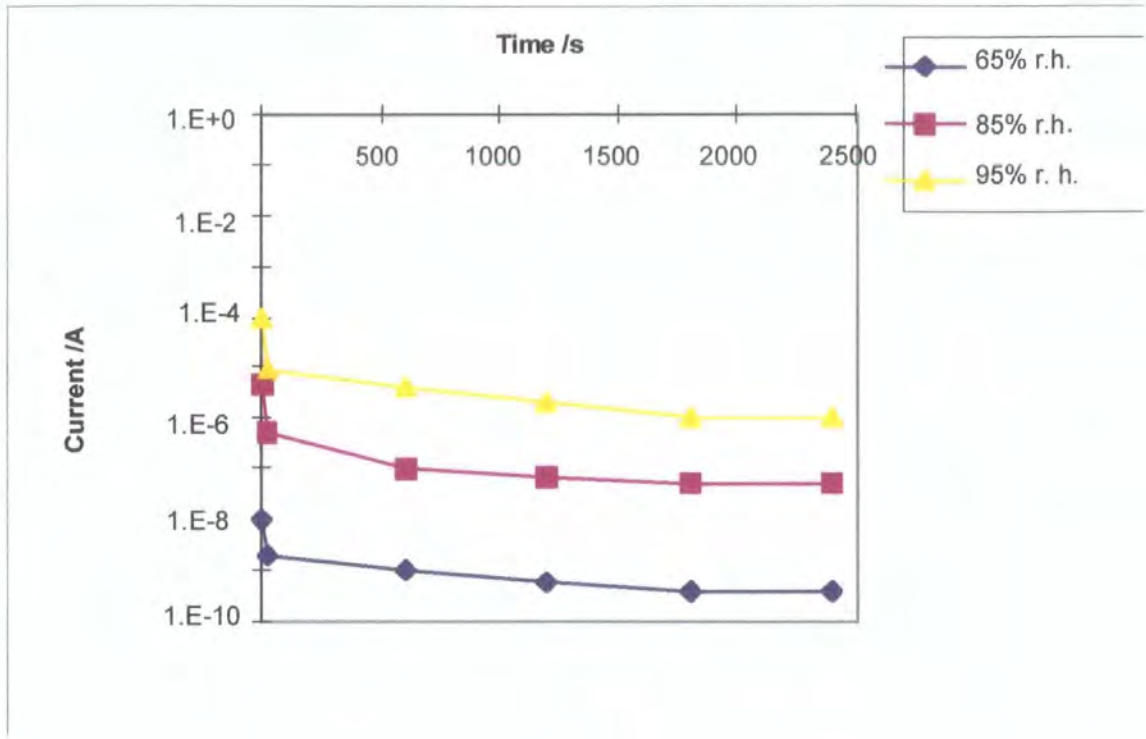

Figure 4.2 – Charging characteristics for a sample of composition x = 0.1, at room temperature and humidities of 65, 85 and 95% r.h.

4.3.2 RESISTIVITY-HUMIDITY CHARACTERISTICS

Figures 4.3, 4.4 and 4.5 show the variation in resistivity with relative humidity for samples of $Zn_xCo_{2-x}GeO_4$, for x = 0, 1.6 and 2 respectively. The resistivity decreases with increasing humidity, by 4 to 5 orders of magnitude for a change in humidity from 10 to 98% *r.h.* The decrease in resistivity is greatest in the middle of the humidity range, from 40 to 70% *r.h.* Over this humidity range the resistivity decreases exponentially. This type of resistivity behaviour is shown by certain other ceramic oxide materials, such as TiO_2 - $K_2Ti_{16}O_{13}$[4], $Ba_{0.5}Sr_{0.5}TiO_3$[5], $MgAl_2O_4$[14], $MgFe_2O_4$[15] and $CaTiO_3$[16].

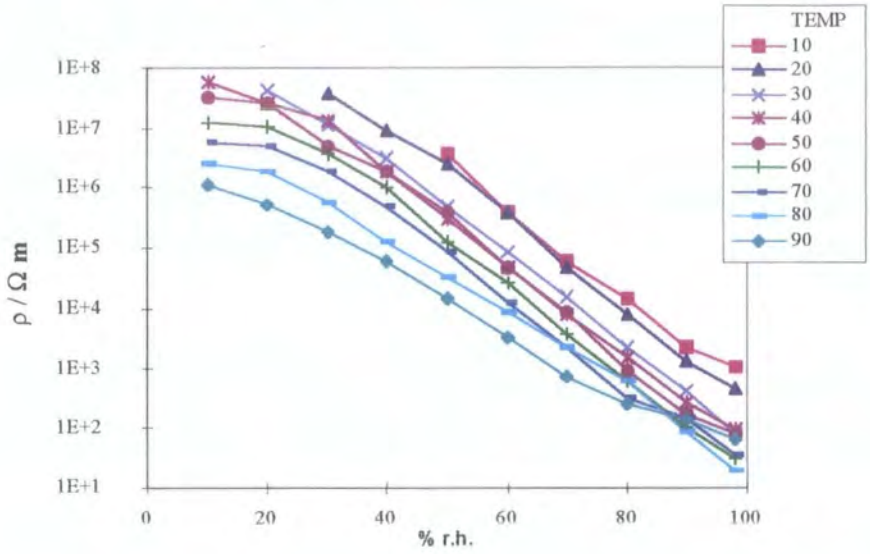

Figure 4.3 - Resistivity versus relative humidity for sample of composition $Zn_xCo_{2-x}GeO_4$, x = 0, at temperatures of 10 to 90°C.

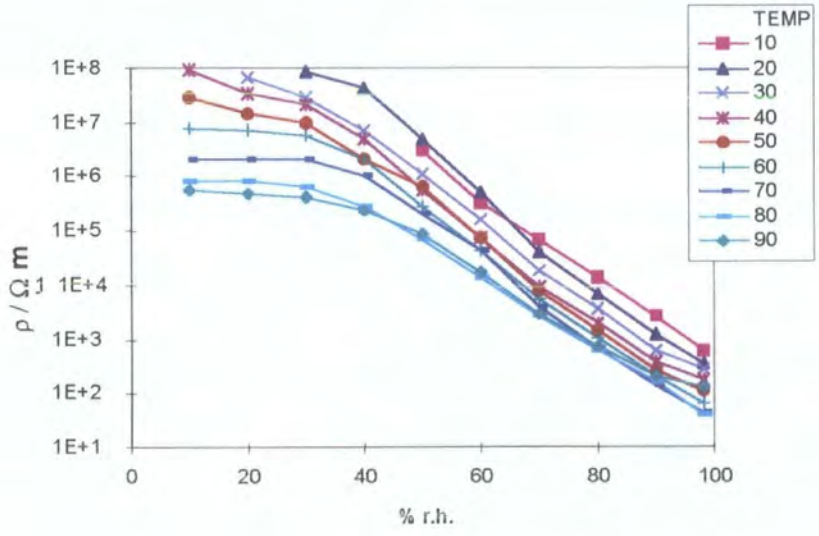

Figure 4.4 - Resistivity versus relative humidity for sample of composition $Zn_xCo_{2-x}GeO_4$, x = 1.6, at temperatures of 10 to 90°C.

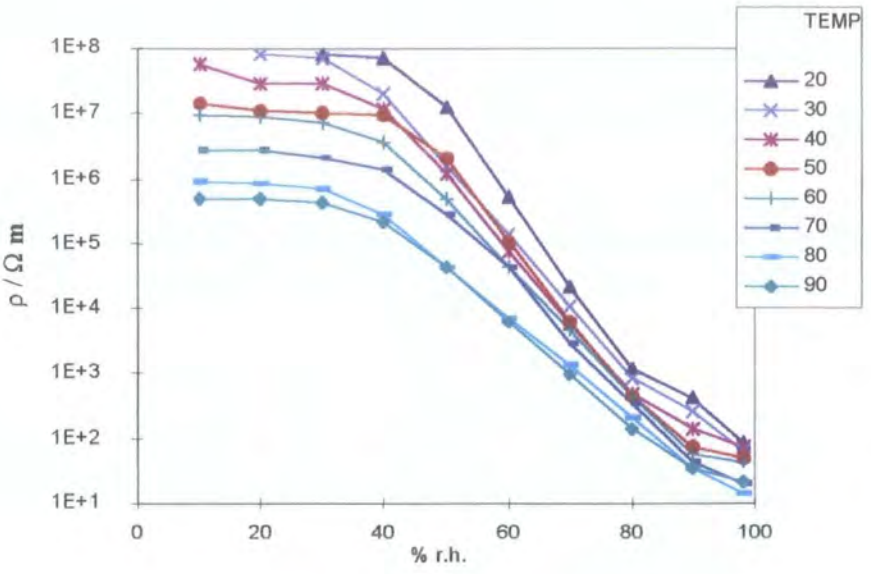

Figure 4.5 - Resistivity versus relative humidity for sample of composition $Zn_xCo_{2-x}GeO_4$, x = 2, at temperatures of 10 to 90°C.

The resistivity-humidity characteristics of samples of various other nominal compositions (x = 0.2, 0.4, 0.6, 1, 1.4, 1.7, 1.8 and 1.9) are shown in Appendix 1, all exhibiting similar behaviour to that described above.

4.3.3 RESISTIVITY-TEMPERATURE CHARACTERISTICS

Figures 4.6, 4.7 and 4.8 show the variation in resistivity with temperature for samples of $Zn_xCo_{2-x}GeO_4$, for x = 0, 1.6 and 2 respectively. Resistivity decreases with increasing temperature, as is typical for most impurity semiconductors. Resistivity decreased by 1 to 2 orders of magnitude from 20°C to 80°C for relative humidities in the range 10 to 50% *r.h.*, whilst in the range 60 to

98% *r.h.* resistivity decreased by approximately 1 order of magnitude from 10 to 80°C. In most cases the resistivity appeared to increase from 80°C to 90°C. This effect was noticeable at higher humidities, especially at 98% *r.h.* This was probably due to an artefact of the system as these measurements were made under conditions approaching the operating limits of the humidity chamber.

The resistivity-temperature characteristics of samples of various other nominal compositions (x = 0.2, 0.4, 0.6, 1, 1.4, 1.7, 1.8 and 1.9) are shown in Appendix 2, all exhibiting similar behaviour to that described above.

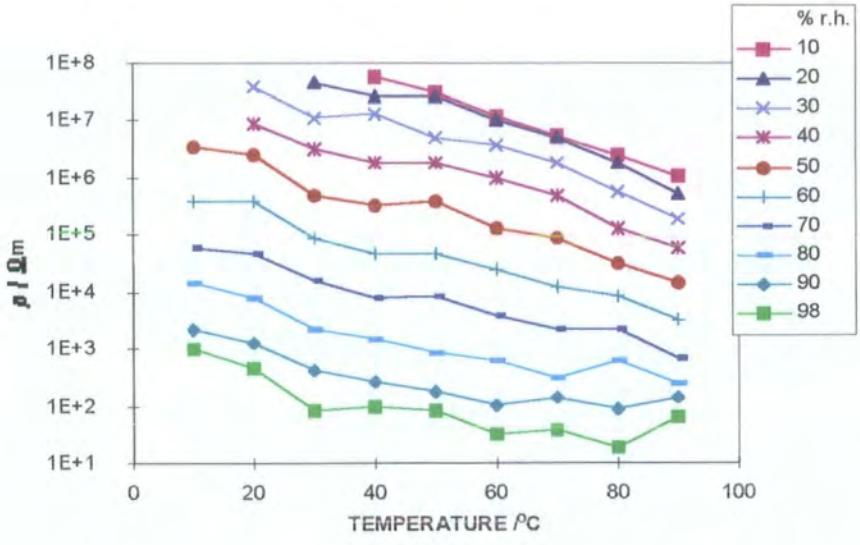

Figure 4.6 - Resistivity versus temperature for samples of composition $Zn_xCo_{2-x}GeO_4$, x = 0, at humidities of 10 to 98% *r.h.*

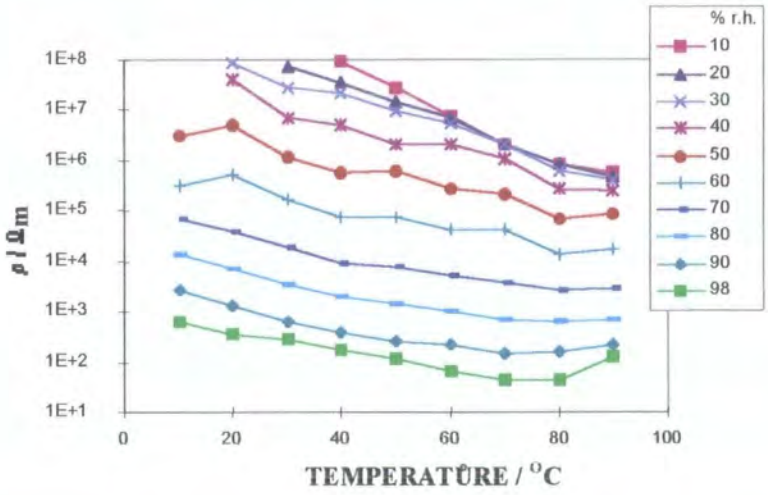

Figure 4.7 - Resistivity versus temperature for samples of composition $Zn_xCo_{2-x}GeO_4$, x = 1.6, at humidities of 10 to 98% *r.h.*

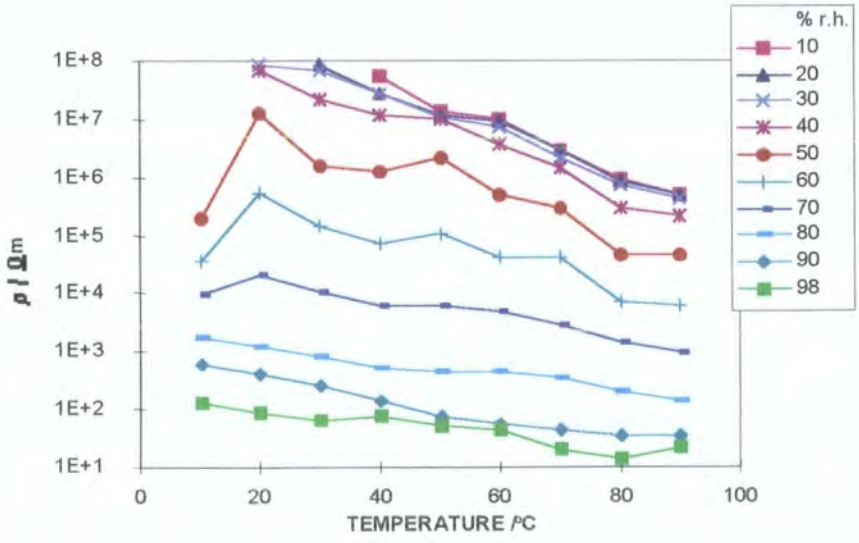

Figure 4.8 - Resistivity versus temperature for samples of composition $Zn_xCo_{2-x}GeO_4$, x = 2, at humidities of 10 to 98% *r.h.*

4.3.4 VARIATION IN HUMIDITY CHARACTERISTICS WITH COMPOSITION

Figures 4.9 and 4.10 show the variation in resistivity with composition, x, of samples of $Zn_xCo_{2-x}GeO_4$, for x = 0 to 2 at temperatures of 40°C and 80°C respectively. There are distinctive variations in the resistivities in the two solid solution phase regions. These variations do not to seem to form any particular trend (it is possible that they could be due to a systematic variation in the preparation of the samples). In the mixed phase region the resistivities are fairly independent of composition. Graphs of resistivity versus composition at various other temperatures (10, 20, 30, 50, 60, 70 and 90°C) are shown in Appendix 3, these all show very similar behaviour.

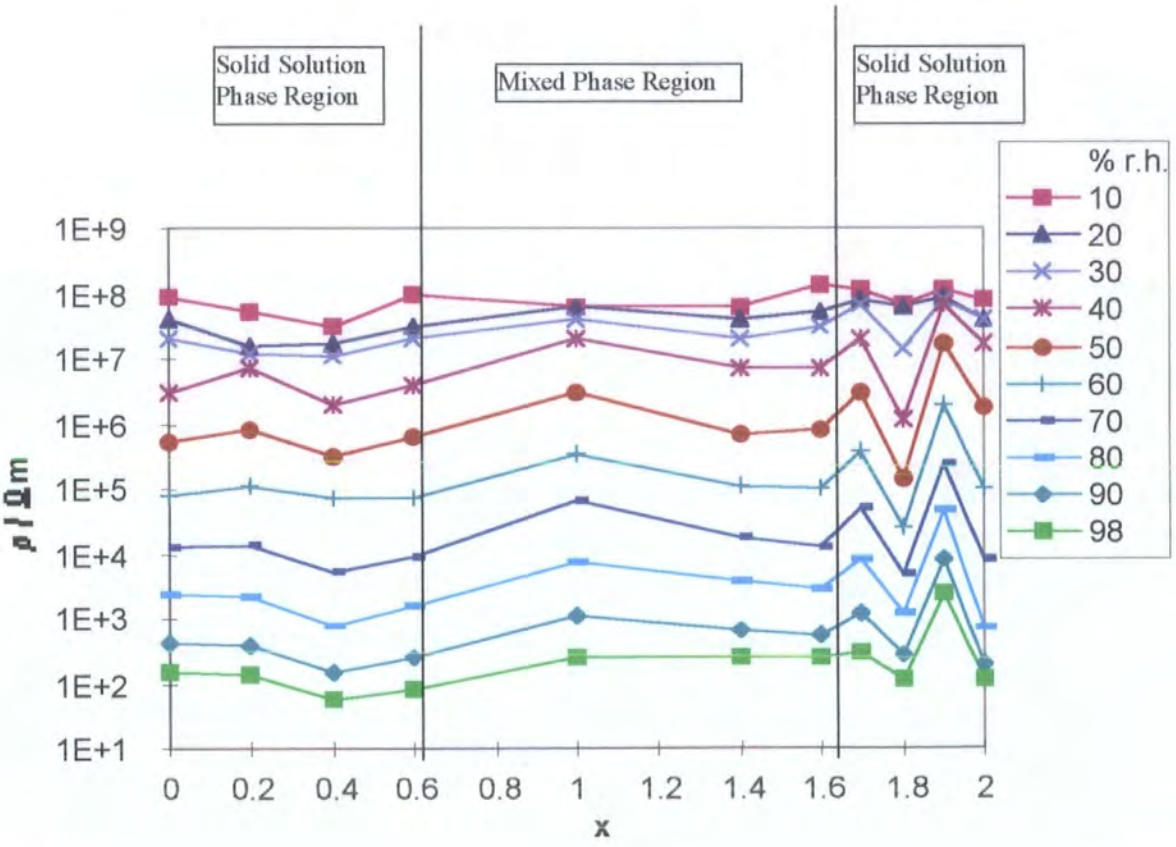

Figure 4.9 - Resistivity versus composition for samples of $Zn_xCo_{2-x}GeO_4$, at 40°C and various humidities.

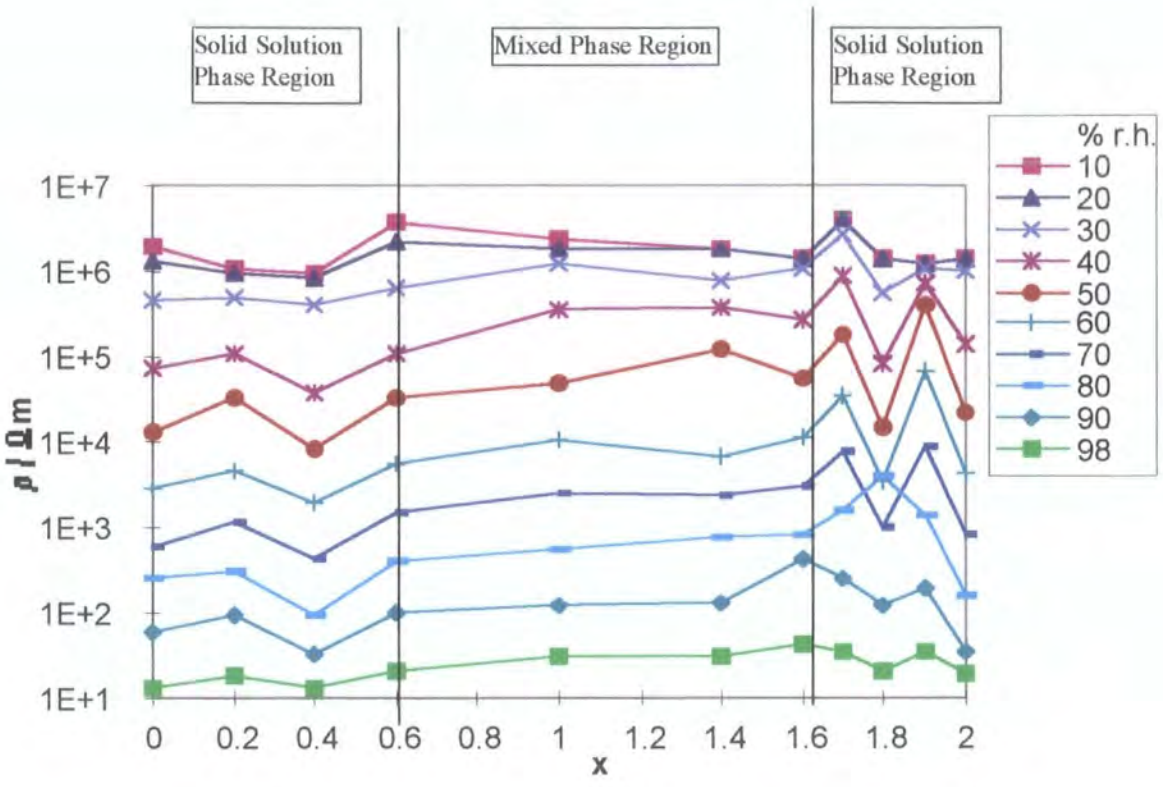

Figure 4.10 - Resistivity versus composition for samples of $Zn_xCo_{2-x}GeO_4$, at 80°C and various humidities.

4.3.5 ACTIVATION ENERGY

Assuming that the total resistivity consists of a humidity-dependent component and a component independent of humidity, due to the $Zn_xCo_{2-x}GeO_4$ ceramic matrix, then in totally dry conditions since the humidity dependent component of resistivity will be infinite, any current will result from conduction by the $Zn_xCo_{2-x}GeO_4$ ceramic matrix. Values of resistivity at 0% *r.h.*, $\rho(0)$, were extrapolated from the graphs of resistivity versus relative humidity in Figures 4.3, 4.4, 4.5 and

Appendix 1. Figure 4.11 shows the extrapolated values of ρ(0) for each composition of material versus the reciprocal of absolute temperature.

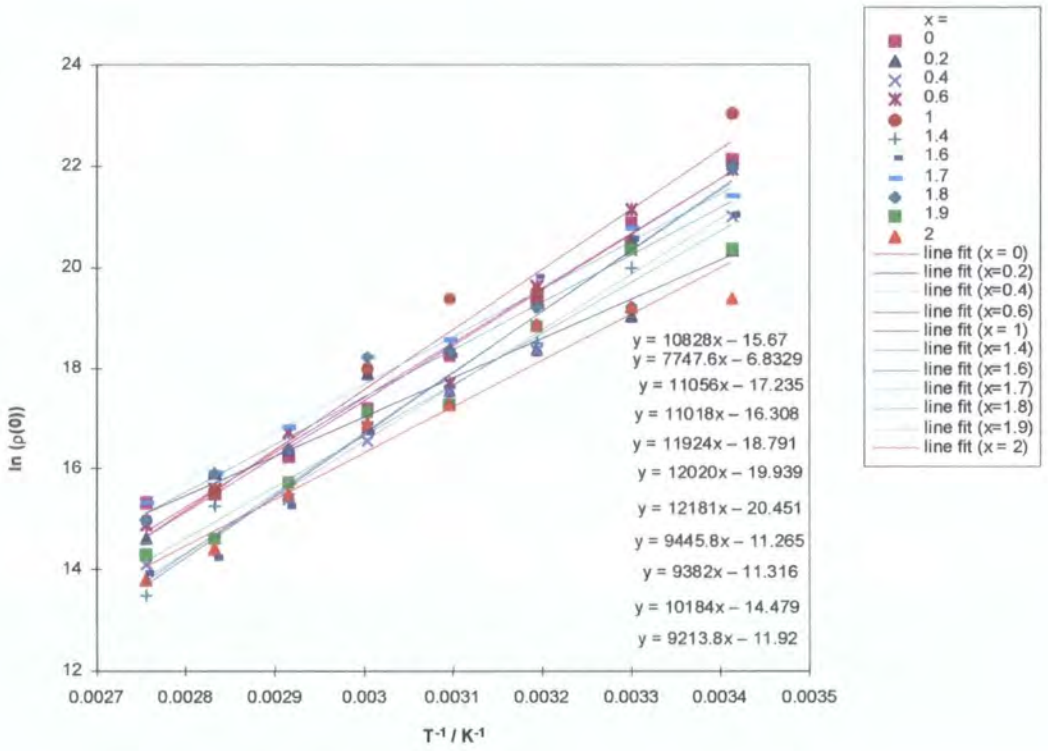

Figure 4.11 - Log of resistivity (at 0% *r.h.*) versus 1 / temperature, for various compositions.

The Arrhenius plots in Figure 4.11 indicate that ρ(0) varied exponentially with the reciprocal of temperature:

$$\rho(0) = A\exp\left(\frac{E}{kT}\right) \qquad \textbf{(4.2)}$$

where A is a constant, E is the activation energy, k is the Boltzman constant and T is absolute temperature. Figure 4.12 shows the activation energies for each sample, calculated from the

gradients of the Arrhenius plots in Figure 4.11, versus composition. The activation energies are fairly scattered but vary little with composition, being approximately 0.9 eV for all compositions. The activation energy is relatively high compared to the typical activation energy of an NTC-thermistor, which is 0.2 to 0.5 eV (corresponding to a temperature coefficient of 2000 - 6000 K)[17].

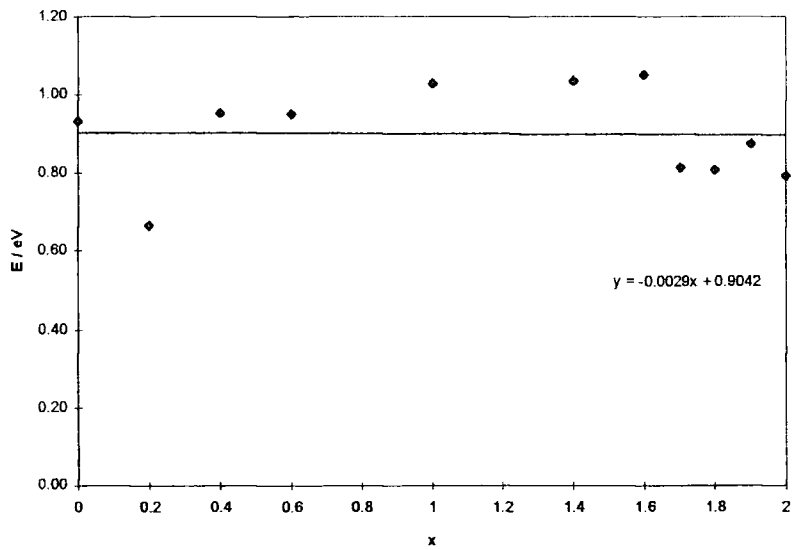

Figure 4.12 - Activation energy versus composition, x, for samples of $Zn_xCo_{2-x}GeO_4$.

4.4 SUMMARY

The charging currents resulting from the application of a potential difference to samples of $Zn_xCo_{2-x}GeO_4$ were found to decrease rapidly in the first few seconds, then to decay more slowly over a period of tens of minutes and to reach a steady state value after about 40 minutes. The

over a period of tens of minutes and to reach a steady state value after about 40 minutes. The conduction carriers in a humid atmosphere were determined to be both ions and electrons, as is the case in materials such as TiO_2 - $K_2Ti_{16}O_{13}$[4] and $Ba_{0.5}Sr_{0.5}TiO_3$[4-6].

The resistivity of $Zn_xCo_{2-x}GeO_4$ decreased with increasing relative humidity, by 4 to 5 orders of magnitude, from 10% to 98% *r.h.* and decreased exponentially from 40 to 70% *r.h.* This type of resistivity behaviour is shown by certain other ceramic oxide materials, such as TiO_2 - $K_2Ti_{16}O_{13}$[4], $Ba_{0.5}Sr_{0.5}TiO_3$[5], $MgAl_2O_4$[14], $MgFe_2O_4$[15] and $CaTiO_3$[16].

The resistivity of $Zn_xCo_{2-x}GeO_4$ does not appear to vary in any systematic way with composition.

The resistivity of $Zn_xCo_{2-x}GeO_4$ has a negative temperature coefficient (NTC). The resistivity decreased by 1 to 2 orders of magnitude for an increase in temperature from 10 to 80°C. The activation energy of the humidity independent conductivity of the material is 0.9 eV and varies little with composition. The activation energy is relatively high compared to the typical activation energy of an NTC-thermistor, which is 0.2 to 0.5 eV.

REFERENCES

[1]B.M. Kulwicki, "Ceramic sensors and transducers", J. Phys. Chem. Solids, **45 (10),** 1015-1031 (1984).

[2]E. Traversa and A. Bearzotti, "A novel humidity detection mechanism for ZnO dense pellets", Sens. & Act. B, **23**, 181-186 (1995).

[3]A. J. Moulson and J. M. Herbert, *Electroceramics: Materials, Properties, and Applications* (Chapman and Hall, London, 1990).

[4]Y-C. Yeh, T-Y. Tseng, and D-A. Chang, "Electrical properties of TiO_2-$K_2Ti_6O_{13}$ porous ceramic humidity sensor", J. Am. Ceram. Soc., **73 (7),** 1992-1998 (1990).

[5]Y.C. Yeh and T.Y. Tseng, "Analysis of the D.C. and A.C. properties of K_2O - doped porous $Ba_{0.5}Sr_{0.5}TiO_3$ ceramic humidity sensor", J. Mater. Sci., **24**, 2739-2745 (1989).

[6]Y-C. Yeh, T-Y. Tseng, and D-A. Chang, "Electrical properties of porous titania ceramic humidity sensors", J. Am. Ceram. Soc., **72 (8),** 1472-1475 (1989).

[7]J.H. Anderson and G.A. Parks, "The electrical conductivity of silica gel in the presence of adsorbed water", J. Phys. Chem, **72,** 3662-3668 (1968).

[8]E. Traversa, "Ceramic sensors for humidity detection: the state-of-the-art and future developments", Sens. & Act. B, **23,** 135-156 (1995).

[9]J.G. Fagan and V.R.W. Amarakoon, "Reliability and reproducibility of ceramic sensors: part III, humidity sensors", Am. Ceram. Soc. Bull., **72 (3),** 119-130 (1993).

[10]W. J. Fleming, "A physical understanding of solid-state humidity sensors", Proc. Int. Auto. Meet., SAE, Detroit, USA, Paper No. 810432, 51-62 (1981).

[11]T. Seiyama, N. Yamazoe, and H. Arai, "Ceramic Humidity Sensors", Sens. & Act., **4 (1),** 85-96 (1983).

[12]Y. Shimizu, H. Arai, and T. Seiyama, "Theoretical studies on the impedance-humidity characteristics of ceramic humidity sensors", Sens. & Act., **7**, 11-22 (1985).

[13]N. Yamazoe and Y. Shimizu, "Humidity sensors - principles and applications", Sens. & Act., **10 (3-4),** 379-398 (1986).

[14]G. Gusmano, G. Montesperelli, E. Traversa et al., "Magnesium aluminium spinel thin film as a humidity sensor", Sens. & Act., **7**, 160-463 (1992).

[15]G. Gusmano, G. Montesperelli, P. Nunziante et al., "Humidity sensitive electrical response of sintered $MgFe_2O_4$", J. Mater. Sci., **28**, 6195-6198 (1993).

[16]D. A. Chang and T. Y. Tseng, "Humidity-sensitive characteristics of $CaTiO_3$ porous ceramics", J. Mater. Sci. Lett., **9**, 943-944 (1990).

[17]T.G. Nenov and S.P. Yordanov, *Ceramic Sensors: Technology and Applications*, (Technomic Publishing AG, Basel, 1996).

CHAPTER 5

IMPEDANCE SPECTROSCOPY

5.1 INTRODUCTION

Impedance spectroscopy is a powerful technique for characterising the electrical behaviour of materials, especially for systems where the time dependent electrical response is governed by a number of different processes[1]. It is particularly useful in characterizing electroceramics in which many interfaces occur - at grain boundaries, both between crystal grains and pore spaces and between grains themselves[2]. At these interfaces physical properties - crystallographic, mechanical, compositional and particularly electrical - may change abruptly. When a potential difference is applied to the system each interface will become polarized and these polarizations will affect the electrical response of the system. When the applied voltage is oscillatory the rate of change of these polarizations will vary in a way that is characteristic of the type of interface. The rate of change of the polarizations is also characteristic of the type of charge carriers involved - i.e. electronic, ionic or mixed electronic-ionic. Therefore information gained from impedance spectra can reveal much about how electrical transport (translative motion of charge carriers) and displacement (reorientation of dipole moments) processes occur within the system.

When interpreting impedance spectra it is useful to represent the experimental impedance data by an equivalent circuit made up of ideal resistors, capacitors and various dispersive elements. An ideal resistor may represent a conductive path such as the bulk conductivity of the material whilst a capacitor may be associated with a space charge polarization region or adsorption process. A dispersive element may represent a frequency dependent process. For any given impedance

spectra there may be a number of equivalent circuits which would fit the data. The important consideration is that the circuit model must also be representative of the physical situation.

In this study impedance spectroscopy was conducted with three aims :

1. to extend the knowledge of the electrical behaviour of the material from that gained in direct current experiments,

2. to suggest an equivalent electrical circuit model to represent the impedance spectroscopy data,

3. to explain the electrical behaviour of the material in physical terms.

5.2 EXPERIMENTAL TECHNIQUES

Measurements were carried out using a Hewlett Packard 4192A LF Impedance Analyser capable of automatically measuring impedance as a function of frequency in the range 5Hz to 13MHz. The Impedance Analyser increases the frequency across a given region of the operating range, in a chosen number of steps. (In these experiments 25 steps were made.) At each step the Impedance Analyser applies a monochromatic voltage signal, $v(t)$, to the sample and measures the resulting steady state small signal current, $i(t)$. The voltage signal is given by:

$$v(t) = V \sin(\omega t) \qquad \textbf{(5.1)}$$

where ω is the angular frequency and V the amplitude. The current is given by:

$$i(t) = I \sin(\omega t + \theta), \qquad \textbf{(5.2)}$$

where θ is the phase difference between the voltage and the current and I is the amplitude. The impedance, Z, is determined from i and v, with the real and imaginary components of the impedance given by:

$$Re(Z) = Z'(\omega) = |Z| \cos(\theta) \quad \textbf{(5.3)}$$

$$Im(Z) = Z''(\omega) = |Z| \sin(\theta) \quad \textbf{(5.4)}$$

During measurement of the impedance spectra, the sample was contained in a purpose-built chamber so that the humidity of the atmosphere surrounding it could be controlled. The chamber, as shown in Figure 5.1, consisted of a sealed cylinder with two inlet valves, a gas mixing chamber, an outlet valve, a recess into which was sealed the probe from a humidity meter, a copper stage with a thermocouple and temperature control circuit and electrical connections for two point resistance measurements on four samples. The two inlet valves were connected to dry and water-saturated gas supplies respectively. Bottled nitrogen was used for the dry gas and compressed air bubbled through water at room temperature for the saturated gas. (Since these measurements were performed at room temperature the reduced oxygen atmosphere produced by the use of nitrogen gas would cause no appreciable change in the oxygen stoichiometry of the materials in the time scale of the experiment.) The humidity in the chamber was controlled by passing a mixture of the two gases through the chamber until the required humidity was achieved. The system was then isolated and allowed to equilibrate for approximately 30 minutes. This is to allow for diffusion within the chamber to produce as near uniform distribution of humidity as possible. The humidity in the chamber was measured using a Thermal Measurement Systems THP 338 digital Thermo-Hygro recorder. This was capable of measuring relative humidity in the range 2% to 98% with an accuracy of ±7% for temperatures between 15°C and 40°C. Impedance spectra were measured at various humidities, within the range 2 to 98% *r.h.*, at room temperature.

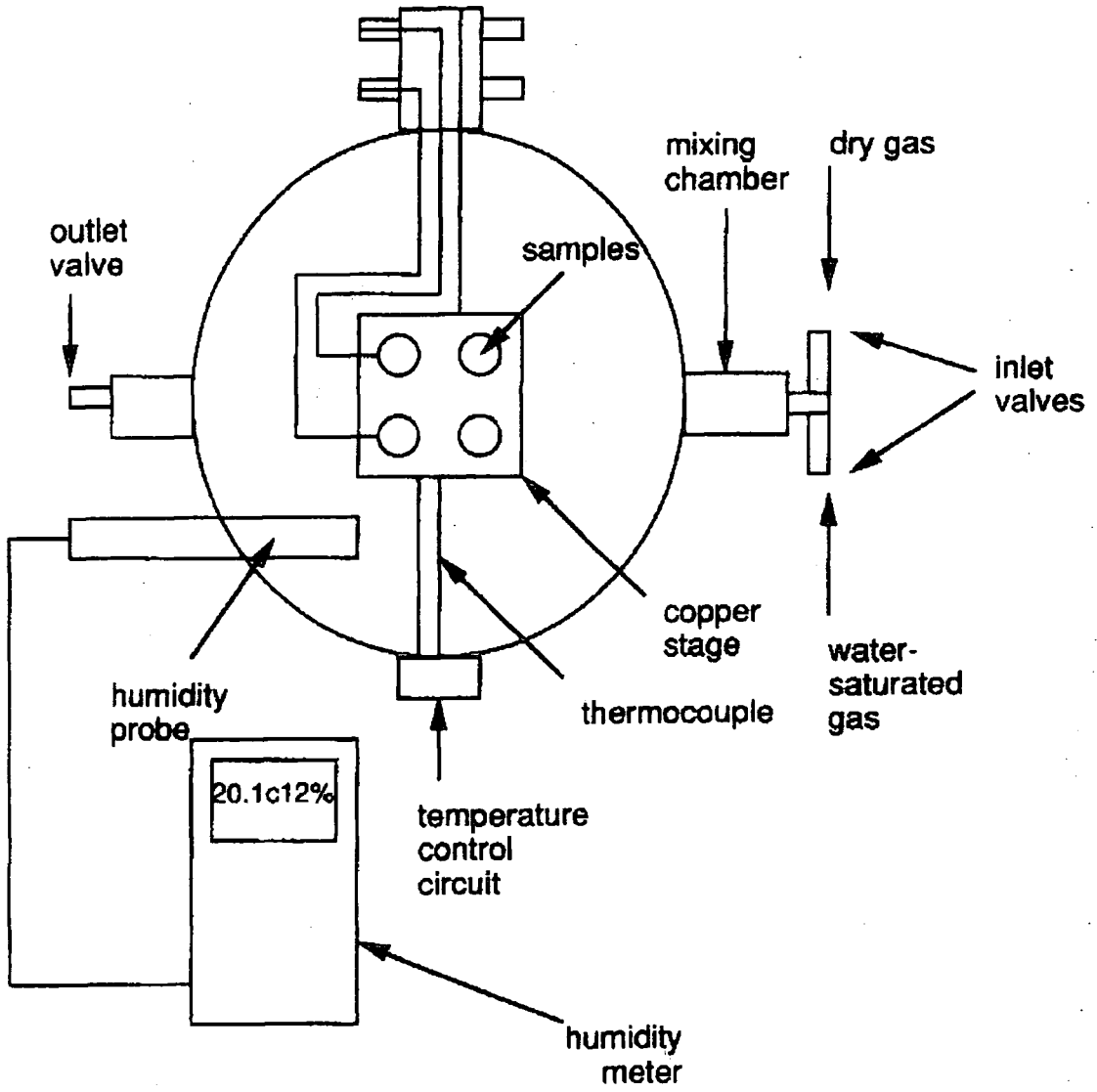

Figure 5.1 - Humidity control chamber.

The samples were in the shape of flat cylindrical discs, typically 13 mm in diameter and 3 mm in thickness. The exact dimensions of each sample disc varied as explained in see Chapter 3. Ga - In electrodes were applied on a single flat surface of the samples, in an interleaved pattern, approximately 1mm apart, as shown in Figure 5.2.

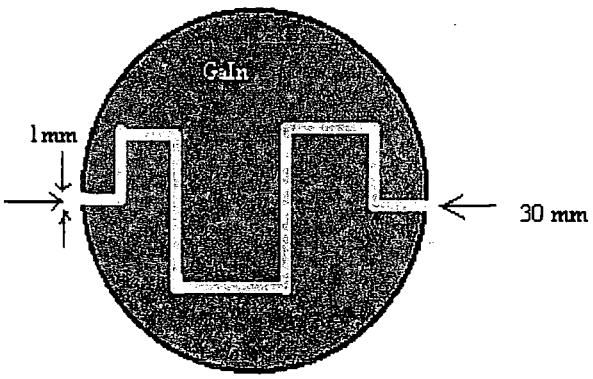

Figure 5.2 – Electrode arrangement.

5.3 RESULTS

5.3.1 IMPEDANCE - FREQUENCY CHARACTERISTICS

Figures 5.3 (a), (b), (c) and (d) show plots of the magnitude of impedance, | Z |, versus frequency at a range of humidities for solid solution phase samples of compositions $Zn_xCo_{2-x}GeO_4$, x = 2, 1.8, 0.2 and 0 respectively. The impedance spectra show a superficial resemblance to the characteristics of a simple RC low pass filter – constant attenuation at low frequency and progressive attenuation (proportional to ω^{-1}) at high frequency.

At low frequencies the impedance is independent of frequency. In this region the impedance is a function of humidity, decreasing with increasing humidity, from 10^9 Ω at 2% *r.h.* to 10^5 Ω at 93% *r.h.* This suggests that the resistive component of the impedance is humidity dependent. At lower humidities, 30% *r.h.* and below, the data points become scattered. This is due to the fact that as the impedance of the material increases the signal becomes smaller and noise in the signal becomes more significant, producing the scattering observed here. Under these relatively dry conditions the impedance of the material approaches the measurement limit of the instrumentation. At higher humidities, 90% *r.h.* and above the impedance shows a slight increase towards the low frequency limit of the data.

At high frequencies impedance is independent of humidity, exhibiting a characteristic roll off, forming a limiting characteristic in which the impedance is inversely proportional to ω. This suggests a capacitive component of impedance which is independent of humidity. The break point frequency is a function of humidity, increasing with decreasing humidity, and represents the point at which the frequency dependent behaviour becomes dominant over the humidity dependent behaviour. In some cases it can be observed that the impedance reaches a small maximum at a frequency just before the break point frequency, particularly noticeable, for example, in Figure 5.3 (d). This behaviour is characteristic of an inductive component of the impedance. The effect

becomes more pronounced as humidity decreases, suggesting that the inductive effect is humidity sensitive.

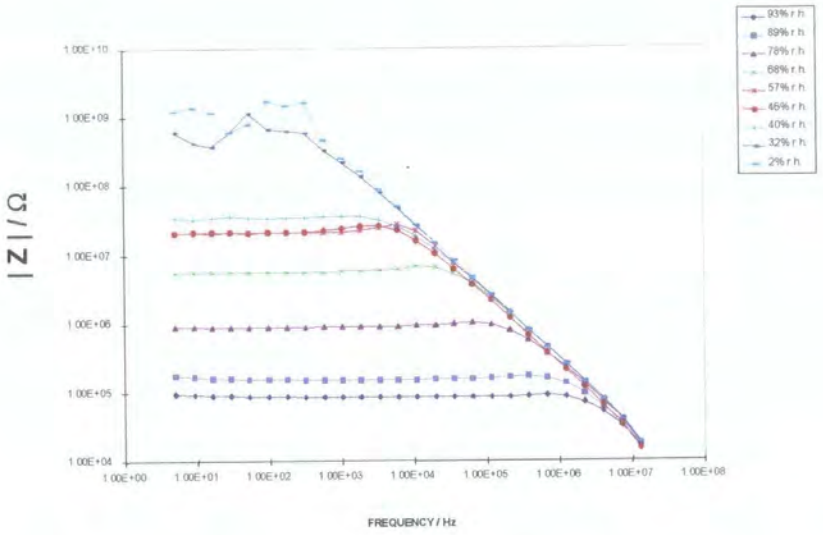

Figure 5.3 (a) - Impedance versus frequency for sample of composition $Zn_xCo_{2-x}GeO_4$, x = 2, at various humidities.

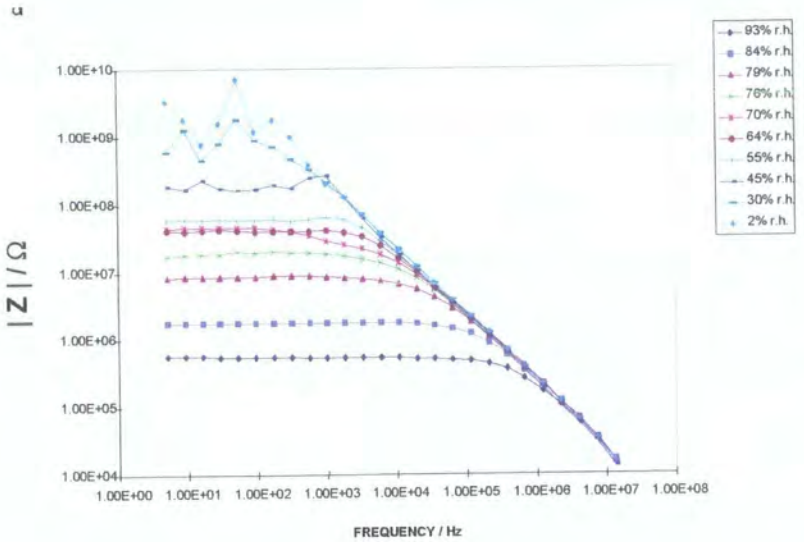

Figure 5.3 (b) - Impedance versus frequency for sample of composition $Zn_xCo_{2-x}GeO_4$, x = 1.8, at various humidities.

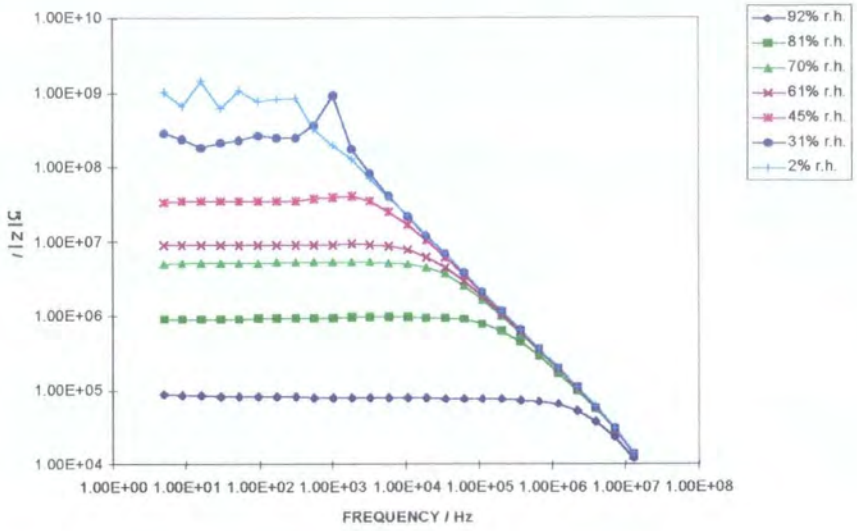

Figure 5.3 (c) - Impedance versus frequency for sample of composition $Zn_xCo_{2-x}GeO_4$, x = 0.2, at various humidities.

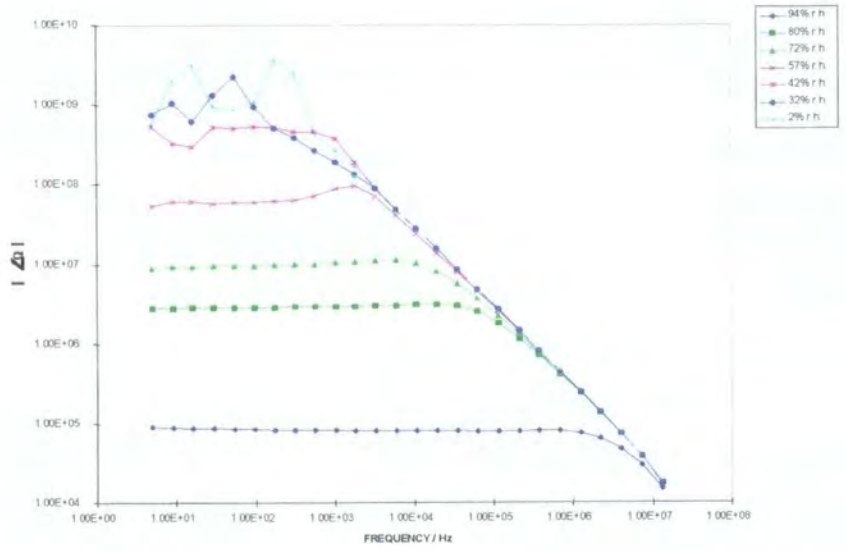

Figure 5.3 (d) - Impedance versus frequency for sample of composition $Zn_xCo_{2-x}GeO_4$, x = 0, at various humidities.

In Figures 5.3 (a) to (d) there appears to be no systematic variation in the impedance with composition, with impedances of all compositions falling in the range from 10^9 Ω at 2% *r.h.* to 10^5 Ω at 93% *r.h.*

Figure 5.4 shows impedance, | Z |, for a frequency of 173 Hz, versus relative humidity for samples of various compositions. This frequency correlates to the frequency independent, humidity dependent region of the frequency spectrum. The characteristics shown here closely resemble those obtained in the DC analysis in Chapter 4, as would be expected from the frequency independent region, with impedance decreasing with increasing humidity by roughly 4 orders of magnitude. This also confirms the lack of systematic variation in impedance with composition.

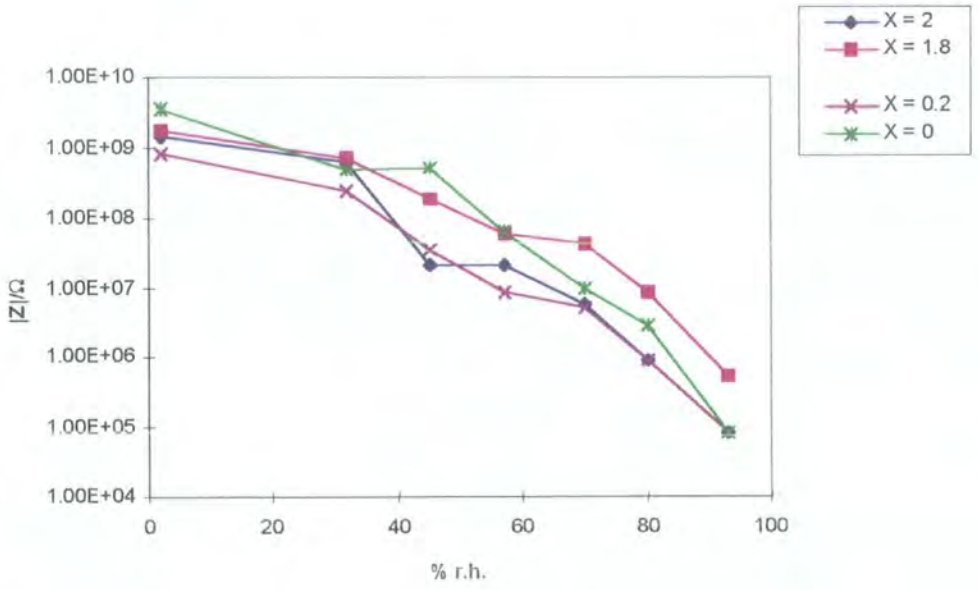

Figure 5.4 - Impedance versus humidity for sample of compositions $Zn_xCo_{2-x}GeO_4$, for various x, at 173 Hz.

5.3.2 COMPLEX IMPEDANCE CHARACTERISTICS

Previously the variation in the magnitude of impedance with both frequency and humidity has been discussed but this does not include any information about electrical phase angle. The real and imaginary parts of impedance (equations **5.3** and **5.4**), which reveal characteristics of the phase angle, were examined in more detail.

Figures 5.5 (a) and (b) show the real and imaginary parts of impedance, Z′ and Z″, versus frequency for a sample of composition Zn_2GeO_4 at various humidities.

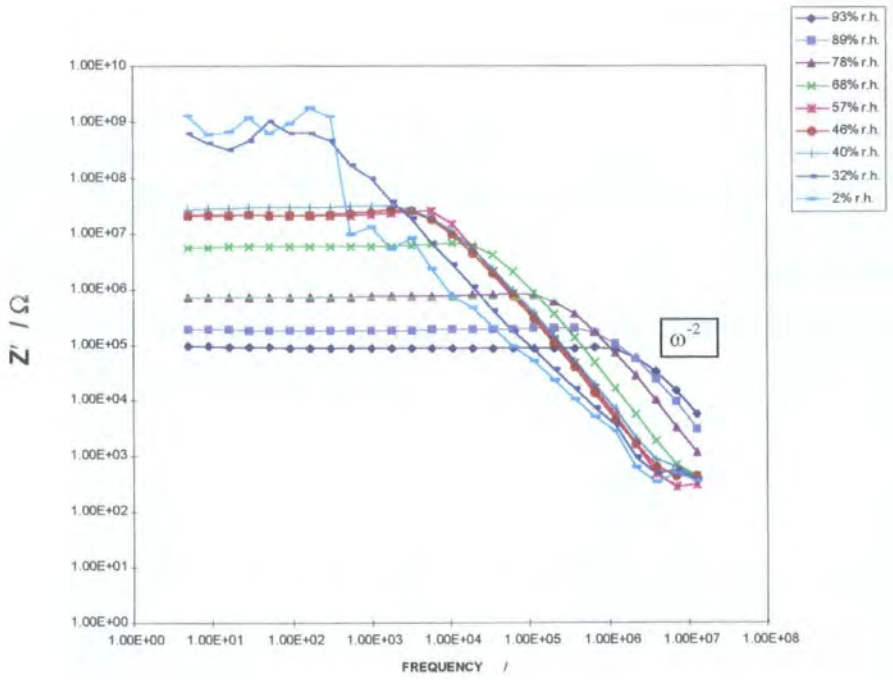

Figure 5.5 (a) - Z' versus frequency for a sample of composition Zn_2GeO_4 at various humidities.

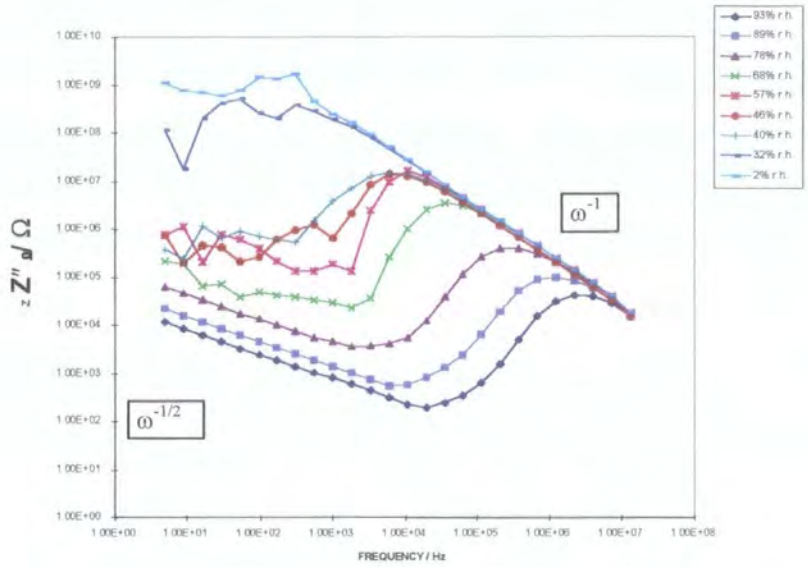

Figure 5.5 (b) - Z'' versus frequency for a sample of composition Zn_2GeO_4 at various humidities.

Equivalent circuit models have been suggested to represent the complex impedance data for many ceramic systems with humidity dependent impedance[2-6,8-10,12]. These are mostly of the form of a resistor representing the grain bulk, a parallel RC component representing the grain surface and a parallel RC component representing the electrode surface, as shown in Figure 5.6.

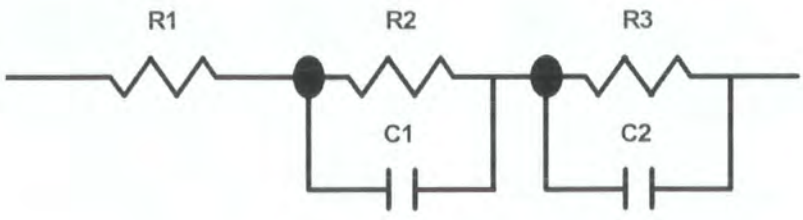

Figure 5.6 – Equivalent circuit model representative of various ceramic systems[9,10].

The characteristics shown by Z' in Figure 5.5 (a) are as would be expected from a simple parallel RC circuit, where the impedance is given by:

$$Z = \frac{R}{1+\omega^2 C^2 R^2} - j\frac{\omega C R^2}{1+\omega^2 C^2 R^2} \qquad (5.5)$$

where R is dependent on humidity, decreasing with increasing humidity, and C is independent of humidity. The real part of the impedance in equation **5.5** is given by:

$$Z' = \frac{R}{1+\omega^2 C^2 R^2}, \qquad (5.6)$$

which would give an impedance at low frequencies, as $\omega \rightarrow 0$, $Z' \approx R$, with Z' independent of frequency, as is the case in Figure 5.5 (a). Also since R is humidity dependent, decreasing with increasing humidity, Z' also decreases with increasing humidity. For high frequencies,

$$Z' \approx \frac{1}{\omega^2 C^2 R}, \qquad (5.7)$$

so for high frequencies Z' would be proportional to ω^{-2} and dependent on humidity, decreasing with decreasing humidity since R increases with decreasing humidity. This behaviour is also observed in Figure 5.5 (a). The break point frequency, that at which the response changes from being frequency independent to proportional to ω^{-1}, is given by:

$$\omega_o = \frac{1}{RC} \qquad (5.8)$$

so that the break point frequency is also humidity dependent, as observed in Figure 5.5 (a).

The imaginary part of the impedance in equation **5.5** is given by:

$$Z'' = \frac{\omega C R^2}{1 + \omega^2 C^2 R^2} \qquad \textbf{(5.9)}$$

The imaginary part of the impedance at high frequencies (i.e. large ω) could be approximated by

$$Z'' \approx \frac{1}{\omega C} \qquad \textbf{(5.10)}$$

which gives a limiting curve, independent of humidity and inversely proportional to ω, as is observed in Figure 5.5 (b). At low frequencies, as $\omega \rightarrow 0$, the imaginary impedance could be approximated by:

$$Z'' \approx \omega C R^2 \qquad \textbf{(5.11)}$$

so, at low frequencies, Z'' would be proportional to ω. However in Figure 5.5 (b) Z'' is proportional to $\omega^{-1/2}$ at low frequencies, so equation **5.5** does not represent the behaviour of Z'' at low frequencies.

In the transition region between low and high frequency behaviour, Z'' is proportional to ω^{μ}, where $\mu \approx 2$ and is humidity dependent. This behaviour also cannot be explained by a simple RC circuit.

The behaviour of Z' can be explained quite well by a simple RC equivalent circuit, however the characteristics of Z'' indicate non-ideal, or non-Debye, capacitive behaviour and require the use of a more sophisticated equivalent circuit.

5.3.3 COMPLEX PLANE ANALYSIS

An alternative method of representing the impedance data is in the complex plane, as Z' versus Z", sometimes referred to as Cole-Cole plots. Since it has already been shown that there is little variation in impedance with composition the results are presented here for one single composition. The same general behaviour was observed for all compositions.

Figures 5.7 (a) to (g) show the locus of the impedance with frequency on the complex plane for a sample of composition Zn_2GeO_4 at humidities of 40 to 93 % *r.h.* (At humidities below 40% the data becomes too scattered to be meaningful.) These plots generally form a distorted semicircle at the high frequency end and a tail at the low frequency end. The low-frequency intercept of the high frequency semi-circle with the real axis gives the value of the real component of resistance. This value increases from 8 x 10^4 Ω at 93% *r.h.* to 3 x 10^7 Ω at 40% *r.h.* These values correspond to the values of impedance at low frequency in Figure 5.3 (a), since, as $\omega \rightarrow 0$, $Z'' \rightarrow 0$ and therefore $|Z| \rightarrow Z'$.

The presence of a high frequency semicircle in the complex plane representation is typical of the behaviour of a parallel RC-like section. The distortion of the semicircle in this case is indicative of more complicated behaviour involving dispersive elements. A dispersive element is one in which the electrical response is frequency dispersive, i.e. it is characterized by a distribution of relaxation times, as opposed to a non-dispersive element, in which electrical response is characterized by a single relaxation time. The intersection between the high frequency semicircle and the low frequency tail is apparent as a loop which becomes more pronounced as humidity decreases. This behaviour is an indication of an inductive-type phase shift, producing resonance with the capacitive components. This behaviour was also observed in the |Z| versus frequency plots in Figures 5.3 (a) as a small maximum at the break point frequency. This inductive behaviour was seen to increase with decreasing humidity. At the low frequency end the tail appears as an almost straight line, inclined at approximately 45° for high humidities, 89 - 93% *r.h.*, Figures, 5.7 (a) and (b). This corresponds to a frequency dependence of $\omega^{-1/2}$, as was observed for Z" in Figure 5.5 (b). This is characteristic of a Warburg-type impedance, typically

due to diffusive type transport processes. At humidities of 40 to 78% *r.h.* this straight line tail is not apparent but the inductive loop is present.

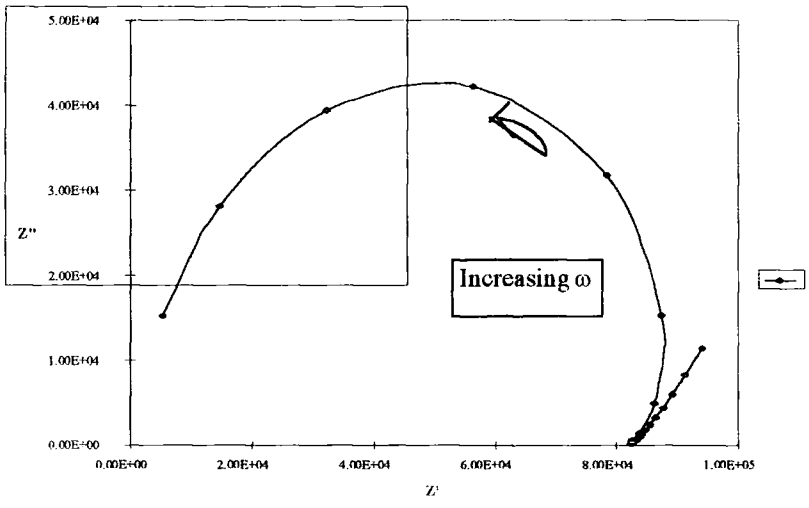

Figure 5.7 (a) - Locus of impedance with frequency in complex plane for sample of Zn_2GeO_4 at 93% *r.h.*

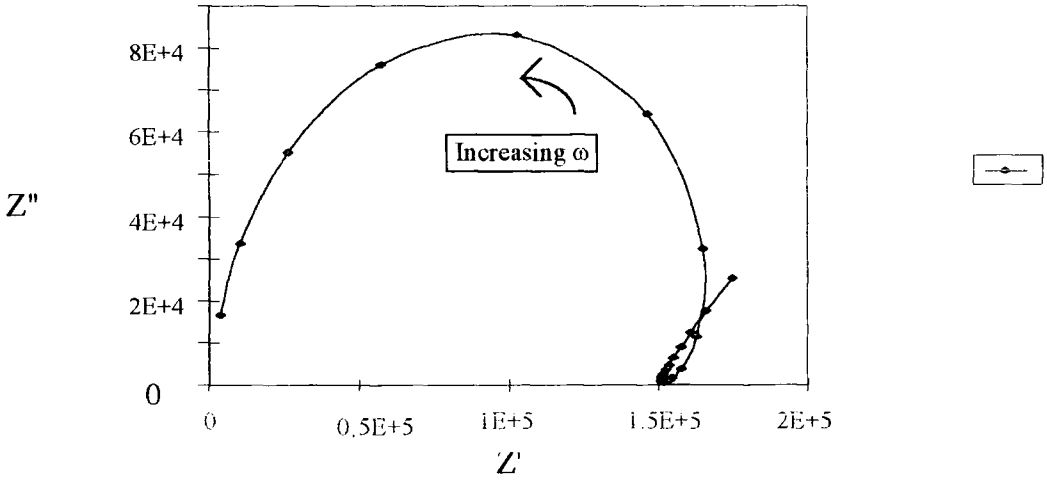

Figure 5.7 (b) - Locus of impedance with frequency in complex plane for sample of Zn_2GeO_4 at 89% *r.h.*

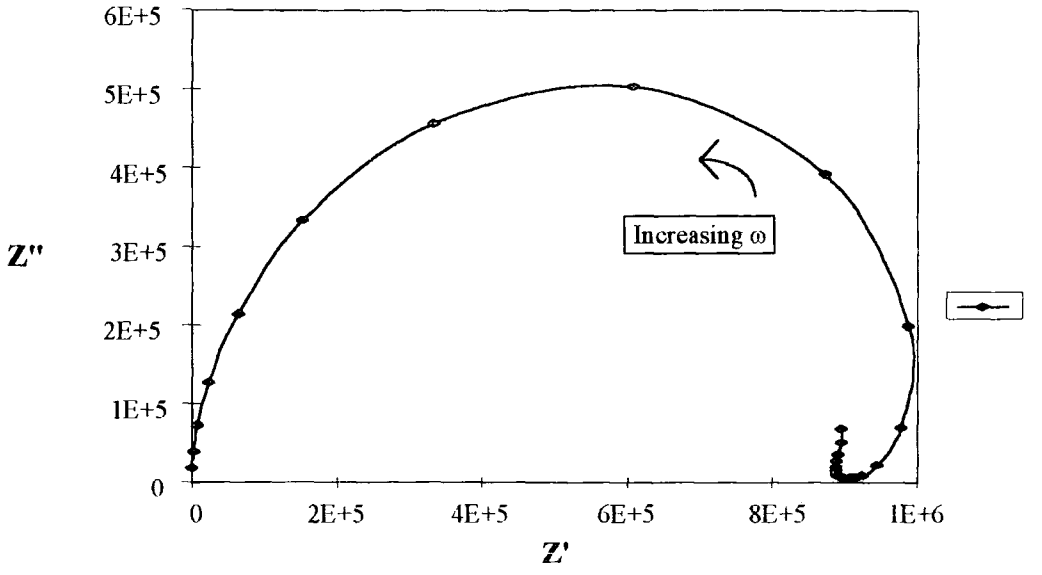

Figure 5.7 (c) - Locus of impedance with frequency in complex plane for sample of Zn_2GeO_4 at 78% *r.h.*

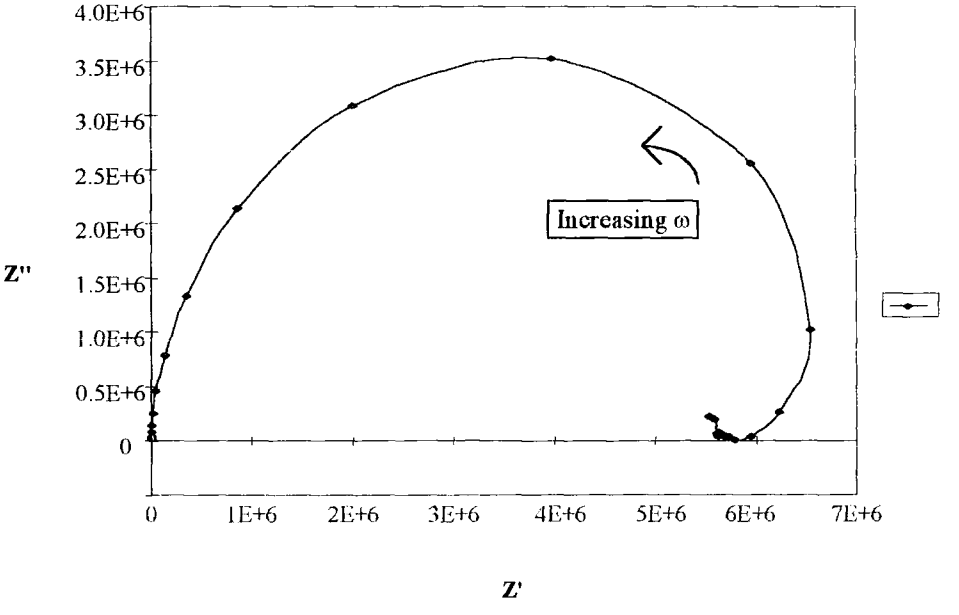

Figure 5.7 (d) - Locus of impedance with frequency in complex plane for sample of Zn_2GeO_4 at 68% *r.h.*

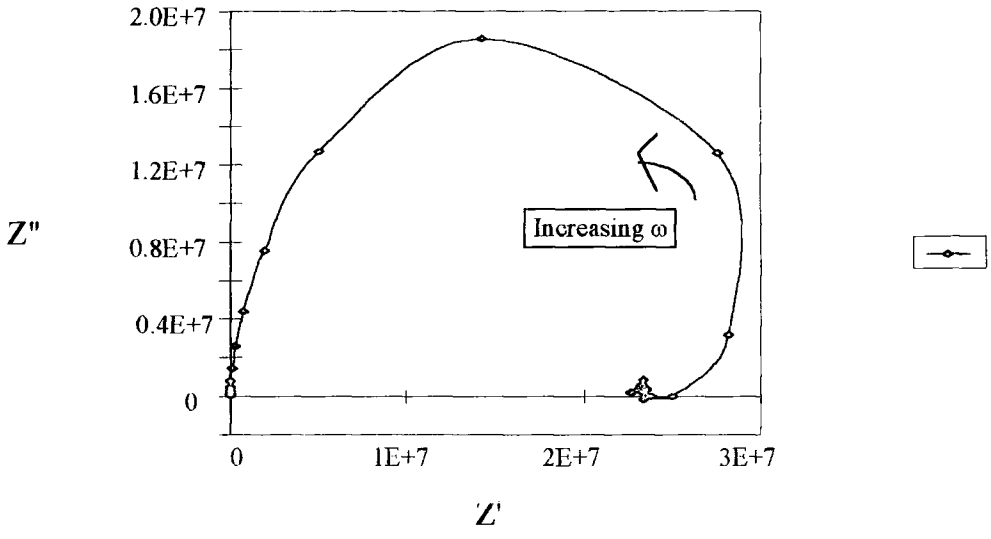

Figure 5.7 (e) - Locus of impedance with frequency in complex plane for sample of Zn_2GeO_4 at 57% *r.h.*

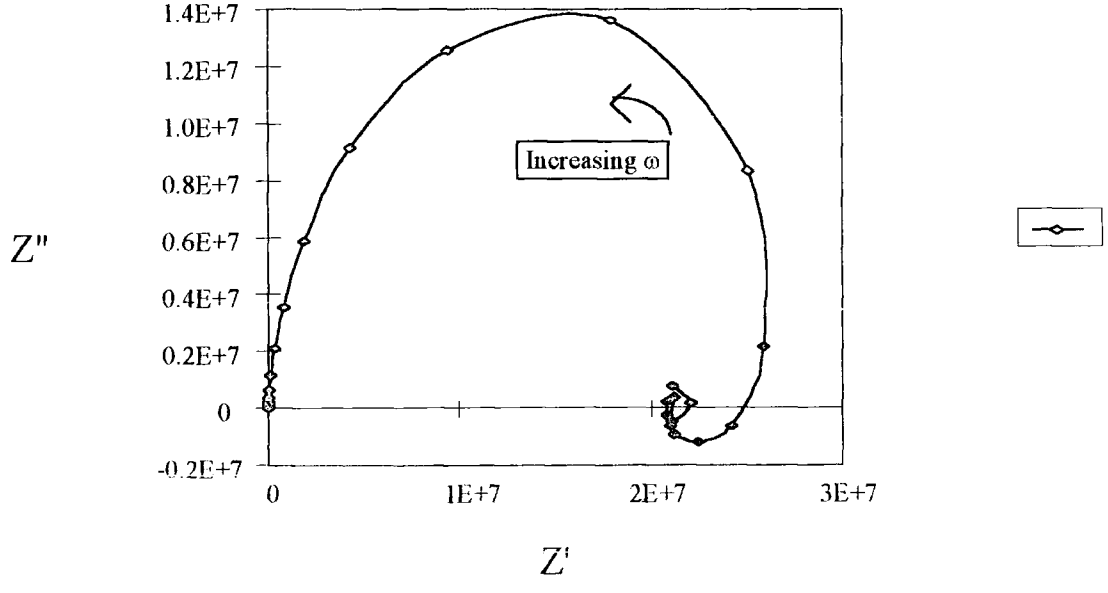

Figure 5.7 (f) - Locus of impedance with frequency in complex plane for sample of Zn_2GeO_4 at 46% *r.h.*

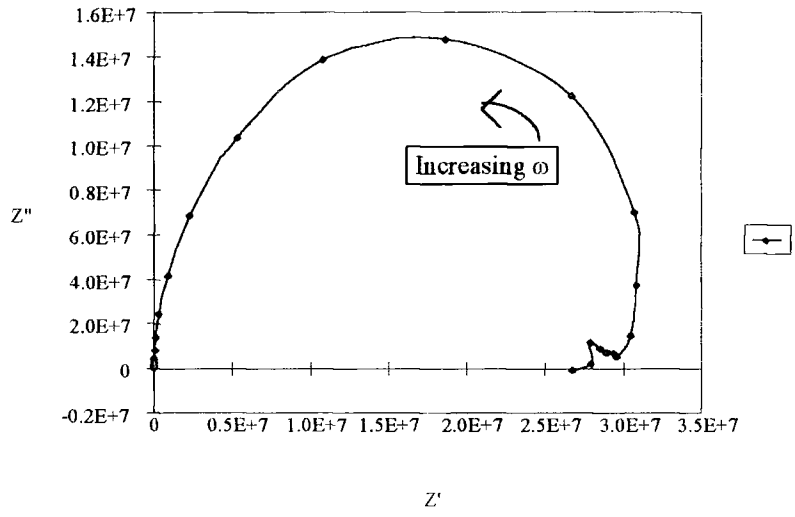

Figure 5.7 (g) - Locus of impedance with frequency in complex plane for sample of Zn_2GeO_4 at 40% *r.h.*

5.4 EQUIVALENT CIRCUIT MODEL

Although the impedance exhibits evidence of resistive and capacitive components it cannot be adequately represented by a simple RC circuit. At frequencies near the break point there is evidence in both the impedance spectra and the complex impedance plane representation of more complicated behaviour suggesting the presence of inductive components. Also in the complex impedance plane the distorted semi-circle, apparent at high frequencies, and the straight-line tail, apparent at low frequencies, are indicative of the behaviour of non-ideal, distributed components[4,8,9,11].

Ideal, or Debye-type, electrical elements, such as resistors capacitors and inductors, are non dispersive and correspond to systems with a single, non-frequency dependent, relaxation time. In non-Debye, or dispersive systems a distribution of relaxation times occurs, making them frequency dispersive[1]. These systems give rise to straight-line behaviour (usually over a limited frequency range) in the complex Z plane, characterized by the phase angle, θ. The frequency response of such a system is proportional to some power of ω and this is termed a Constant Phase Element (CPE). The impedance of a CPE is given by:

$$Z_{cpe} = \frac{1}{A(j\omega)^{\alpha}} \qquad (5.12)$$

and, since $$j^n = \cos\frac{n\pi}{2} + j\sin\frac{n\pi}{2} \qquad (5.13)$$

$$Z_{cpe} = \frac{1}{A\omega^{\alpha}}\left[\cos\frac{\alpha\pi}{2} - j\sin\frac{\alpha\pi}{2}\right] \qquad (5.14)$$

where A and α are constants with $0 \leq \alpha \leq 1$. For $\alpha = 1$ this describes the behaviour of a capacitor and for $\alpha = -1$ this describes the behaviour of an inductor. Where $\alpha = 0.5$, the frequency response is proportional to $\omega^{-1/2}$ and the phase angle ($\theta = \alpha\ \pi\ /\ 2$) is equal to 45°. This is termed a Warburg Impedance and describes the typical behaviour of diffusive type processes.

5.4.1 EQUIVALENT CIRCUIT

After extensive trials an equivalent circuit was found to represent the experimental data reasonably well. The circuit, as shown in Figure 5.8, consists of a resistor, R_1, representing the bulk conductivity of the material, a capacitor, C_1, representing the bulk capacitance of the material plus any capacitance arising due to the measuring system, the constant phase elements

CPE_1 and CPE_2, representing the frequency dependent capacitive and inductive effects arising from space charge polarizations and adsorption processes within the material and a Warburg Impedance, CPE_3, (a constant phase element with $\alpha = 0.5$) representing diffusion at the electrodes. The impedance of each of these elements are given in Table 5.1, where R_1 and C_1 are the values of the resistor and the capacitor respectively, T_1 and T_2 are constants describing the behaviour of CPE_1 and CPE_2, P_1 and P_2 are the exponents describing the behaviour of CPE_1 and CPE_2 and T_3 is a constant describing the behaviour of CPE_3.

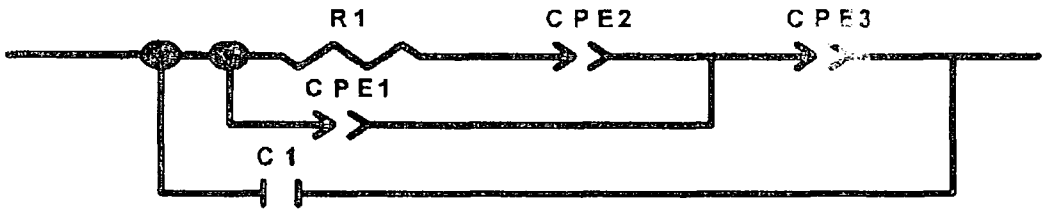

Figure 5.8 - Equivalent circuit model.

ELEMENT	R_1	CPE_1	CPE_2	CPE_3	C_1
Z	R_1	$\frac{1}{T_1(j\omega)^{P_1}}$	$\frac{1}{T_2(j\omega)^{P_2}}$	$\frac{1}{T_3(j\omega)^{1/2}}$	$\frac{1}{j\omega C_1}$

Table 5.1 - Impedances of elements in equivalent circuit

5.4.2 FIT OF EQUIVALENT CIRCUIT TO EXPERIMENTAL DATA

The impedance of the equivalent circuit shown in Figure 5.8 was fitted to the experimental impedance data for Zn_2GeO_4 at humidities above 40% *r.h.* A Complex Non-Linear Least Squares fitting procedure was used, as written by J.R. Macdonald and incorporated in the ZView Software by Schribner Associates (1998). The parameters for the circuit elements were calculated to give the best fit at each value of humidity and these are given in Figures 5.10 (a) to (h) as will be discussed later.

In order to check the quality of the fit, the impedance of the equivalent circuit was then simulated over the frequency range 0.5 Hz to 130 MHz for each value of humidity. A wider frequency range was used for the simulations than that of the experimental data in order to check that the model would produce the expected response in the extended frequency range.

Figures 5.9 (a) to (g) show the simulated impedance and the experimental data in the complex Z plane at various humidities. In the high frequency range the simulated impedance gives a fairly good fit to the distorted semicircle at all the humidity values shown. The extended frequency range of the simulated impedance shows that the semicircle does intersect with the origin at higher frequency. In the low frequency region the fit is not quite so good for all humidities. At 93% *r.h.*, Figure 5.9 (a), and 89% *r.h.*, Figure 5.9 (b), the 45° low frequency tail in the simulated impedance is a good fit to the experimental data, whereas at 78% *r.h.*, Figure 5.9 (c), the simulated impedance deviates from the experimental data where the data forms a tail inclined at > 45°. For humidities below 78% the low frequency experimental data becomes scattered and the tail is not apparent. The inductive loop is clearly shown in the simulated impedance for humidities of 89% *r.h.*, Figure 5.9 (b), to 46% *r.h.*, Figure 5.9 (f), in fairly good agreement with the experimental data, except where at 68%, Figure 5.9 (d) and 57%, 5.9 (e), where the loop in the simulated impedance appears exaggerated with respect to the experimental data. The inductive loop is not present in either the simulated impedance or the experimental data at 40% *r.h.*, Figure 5.9 (g). In the case of the experimental data this could be due to scattering hiding the effect, but the absence of any loop in the simulated plots suggests that this may be a real effect.

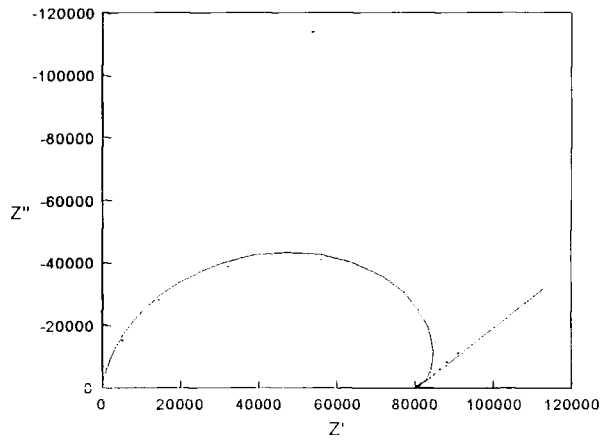

Figure 5.9 (a) - Locus of impedance with frequency in the complex plane with points showing experimental data and line showing simulated impedance of equivalent circuit for sample of Zn_2GeO_4 at 93% *r.h.*

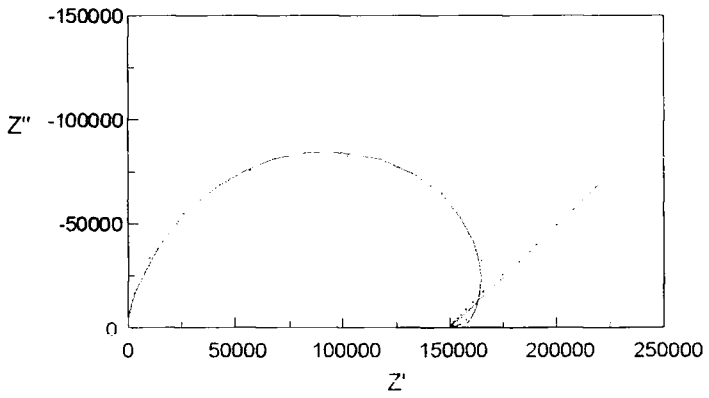

Figure 5.9 (b) - Experimental data and simulation for sample of Zn_2GeO_4 at 89% *r.h.*

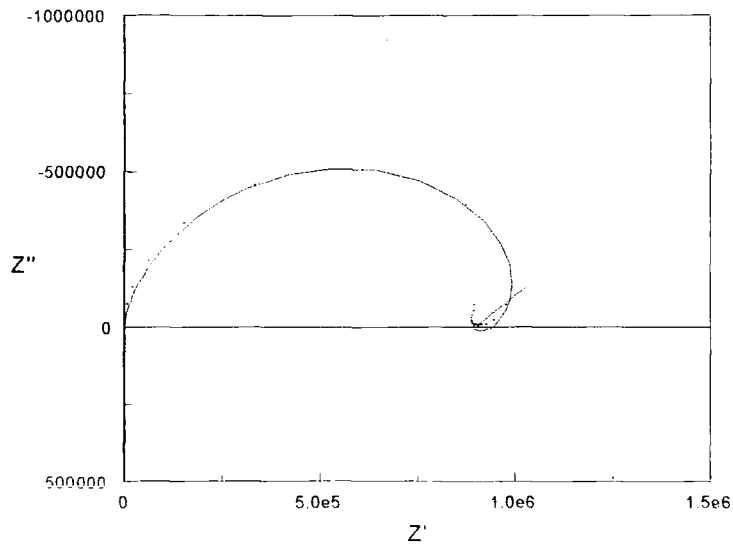

Figure 5.9 (c) - Experimental data and simulation for sample of Zn_2GeO_4 at 78% *r.h.*

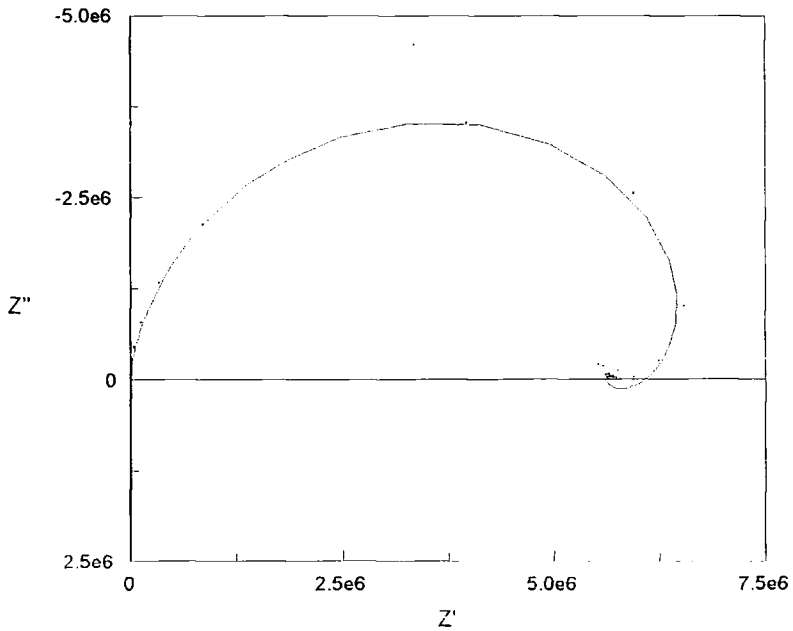

Figure 5.9 (d) - Experimental data and simulation for sample of Zn_2GeO_4 at 68% *r.h.*

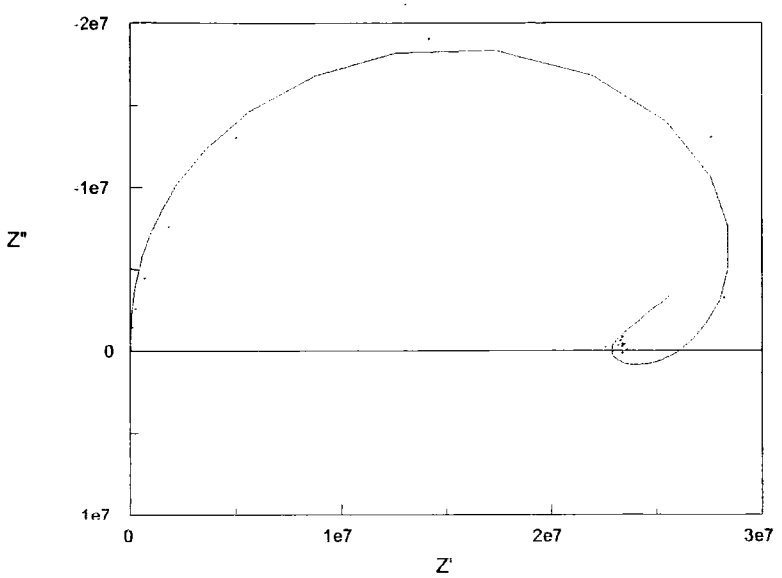

Figure 5.9 (e) - Experimental data and simulation for sample of Zn_2GeO_4 at 57% *r.h.*

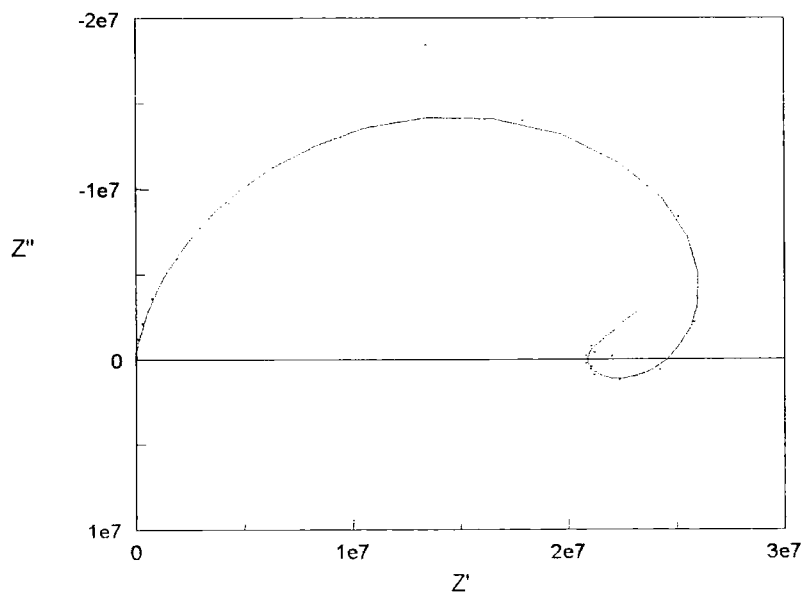

Figure 5.9 (f) - Experimental data and simulation for sample of Zn_2GeO_4 at 46% *r.h.*

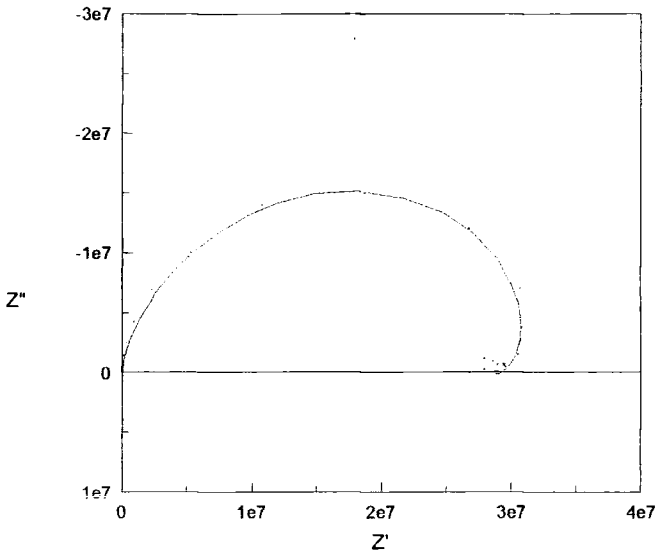

Figure 5.9 (g) - Experimental data and simulation for sample of Zn_2GeO_4 at 40% *r.h.*

The fit of the simulated impedances to the experimental data for samples of compositions $Zn_xCo_{2-x}GeO_4$, x = 1.8 and 0.2, at various humidities are shown in Appendix 4.

5.4.3 VARIATION OF EQUIVALENT CIRCUIT PARAMETERS WITH HUMIDITY

Figures 5.10 (a) to (g) show how the values of the parameters of the components in the equivalent circuit, C_1, R_1, P_1, T_1, P_2, T_2 and T_3, varied with humidity for the fit to experimental data for a sample of composition Zn_2GeO_4.

Figure 5.10 (a) shows C_1 independent of humidity, approximately 10^{-12} F for all compositions. Figure 5.10 (b) shows the values of R_1 decreasing by approximately 2 orders of magnitude with increasing humidity from approximately 3 x 10^7 Ω at 40% *r.h.* to 1 x 10^5 Ω at 93% *r.h.*

Figure 5.10 (c) shows that the values of P_1, the exponent describing the behaviour of CPE_1, were nearly constant for all humidities, with a value of 0.48. Figure 5.10 (d) shows the trend in the values of T_1, the constant describing the behaviour of CPE_1. T_1 increases with increasing humidity from 10^{-10} Ω^{-1} at 40 % *r.h.* to 10^{-9} Ω^{-1} at 93% *r.h*, with a dip at around 57% *r.h.* The impedance of CPE_1 is inversely proportional to T_1, therefore decreases with increasing humidity, with a peak at around 57% *r.h.*

Figure 5.10 (e) shows the values of P_2, the exponent describing the behaviour of CPE_2, nearly constant for all humidities, with a value of -0.63. The negative sign of P_2 indicates that CPE_2 has inductive type characteristics. Figure 5.10 (f) shows the trend in the values of T_2, the constant describing the behaviour of CPE_2. T_2 increases by 4 orders of magnitude with increasing humidity, from 10^{-5} Ω^{-1} at 40 % *r.h.* to approximately 10^{-1} Ω^{-1} at 93% *r.h.* The impedance of CPE_2 is inversely proportional T_2, therefore decreases by 4 orders of magnitude with increasing humidity.

Figure 5.10 (g) shows the trend in the values of T_3, the constant describing the behaviour of CPE_3. T_3 increases with increasing relative humidity from approximately 10^{-7} Ω^{-1} for humidities below 57% *r.h.* to 10^{-5} Ω^{-1} for humidities above 60% *r.h.*, in an almost stepwise function. The impedance of CPE_3 is inversely proportional to T_3, therefore it will decrease with increasing humidity, by 2 orders of magnitude at around 57 % *r.h.*

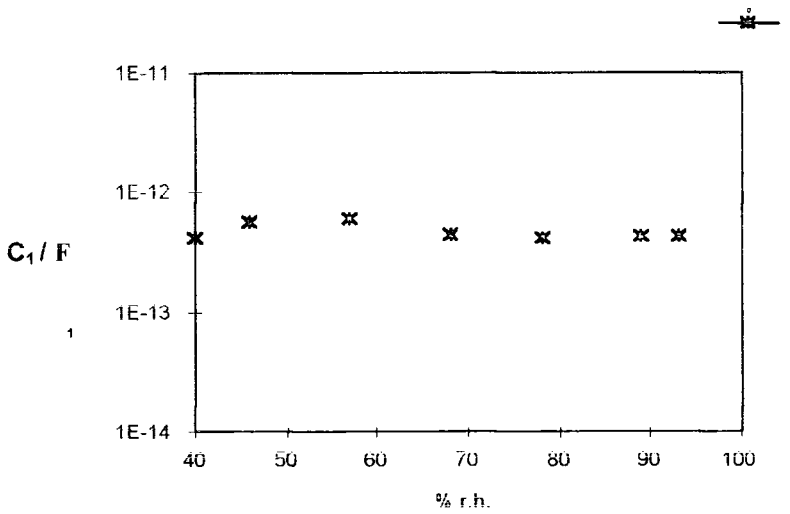

Figure 5.10 (a) - C_1 versus relative humidity for sample of Zn_2GeO_4

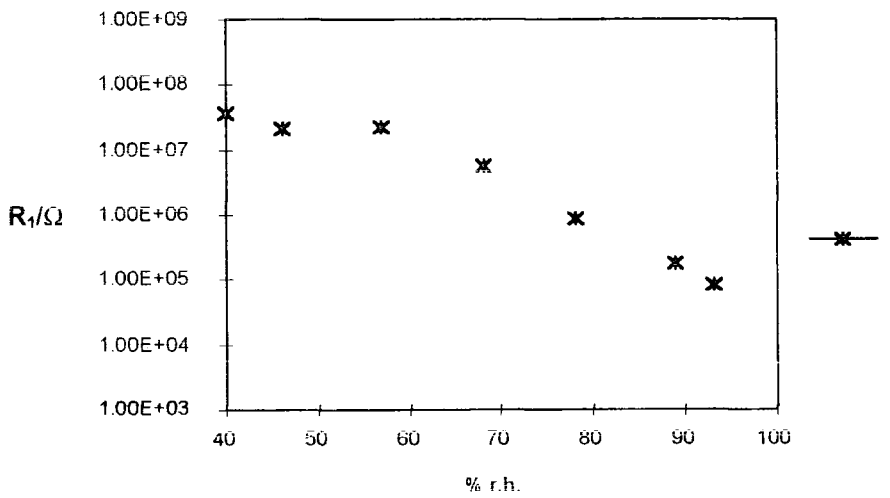

Figure 5.10 (b) - R_1 versus relative humidity.

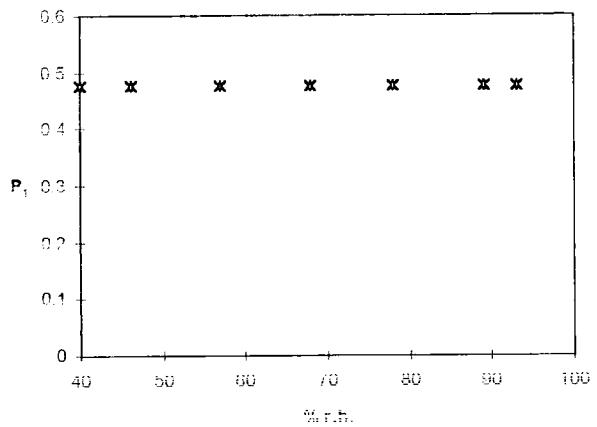

Figure 5.10 (c) - P_1 versus relative humidity

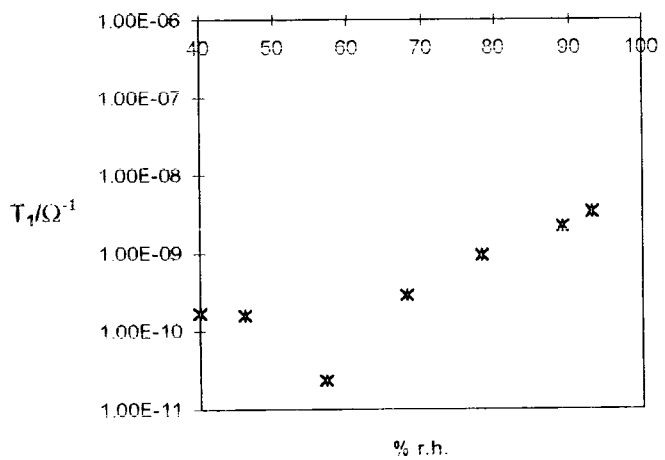

Figure 5.10 (d) - T_1 versus relative humidity

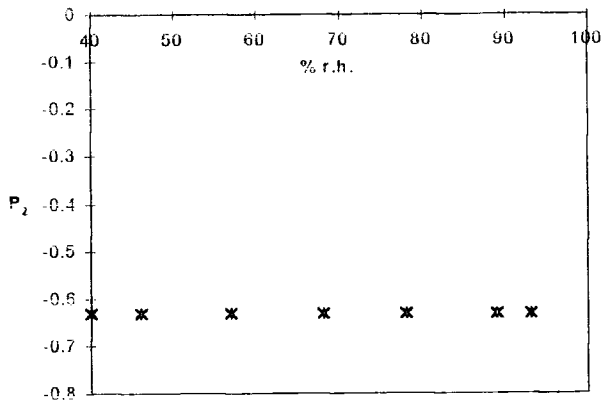

Figure 5.10 (e) - P_2 versus relative humidity

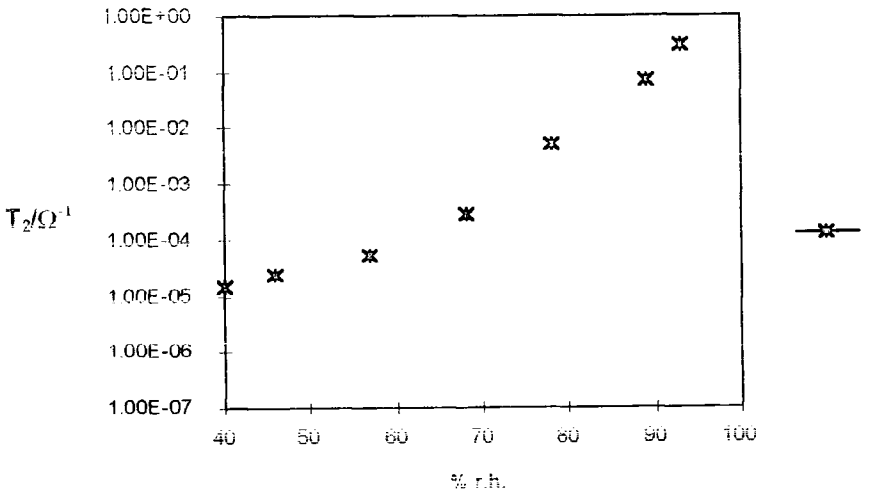

Figure 5.10 (f) - T_2 versus relative humidity.

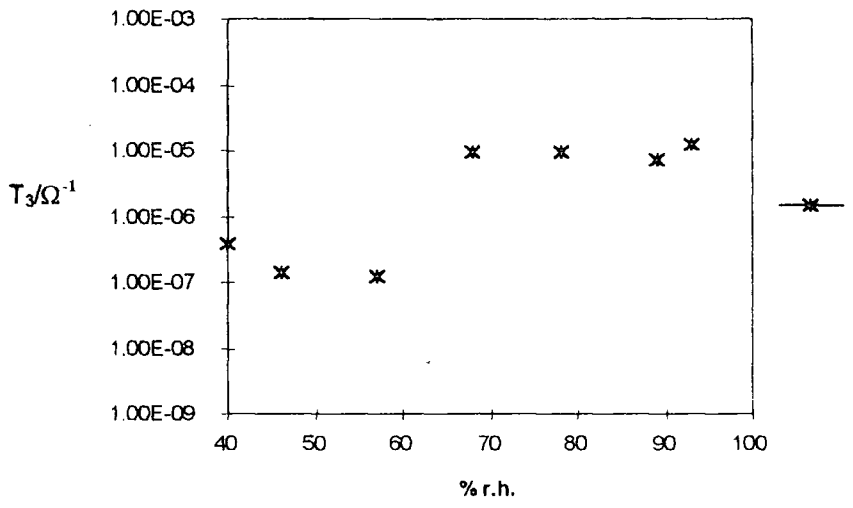

Figure 5.10 (g) - T_3 versus relative humidity

5.5 PHYSICAL MODEL FOR THE CONDUCTION MECHANISM

It is commonly accepted that humidity dependent ionic conduction within certain ceramic materials results from the chemisorption and physisorption of water molecules at the surface of the material. At low humidities, conduction occurs by hopping of protons between adjacent hydroxyl groups formed at the surface by the dissociative chemisorption of water molecules[13,14]. At intermediate humidities conduction takes place predominantly by diffusion of physisorbed H_3O^+ ions, formed by the dissociation of physisorbed water molecules, between neighbouring hydroxyl groups[13,14]. At higher humidities conduction occurs by hopping of protons from H_3O^+ ions to water molecules in the physisorbed layers[14,15,13]. The change from conduction by diffusion of H_3O^+ ions to conduction by proton hopping is gradual and takes place

as the number of adsorbed water molecules increases. Electrolytic conduction also occurs at higher humidities in layers of water condensed in capillary pores[14,16]. Electronic conductivity also takes place by the release of electrons from chemisorbed oxygen ions and /or surface defects which occurs when water molecules are adsorbed onto the oxide surface[17,18].

The elements of the equivalent circuit model, Figure 5.8, which was shown to represent the experimental impedance data, and the variation in the parameters of these elements with humidity, as shown in Figures 5.10 (a) to (g), can be related to the physical model for humidity dependent conduction.

It is proposed that in the equivalent circuit model the combination of R_1 and CPE_2 in series, with CPE_1 in parallel represents the humidity dependent conductivity of the material. R_1 represents the ideal, resistive components of the humidity dependent conduction, decreasing with increasing humidity. CPE_1 and CPE_2 represent the dispersive, non-Debye components of the humidity-dependent conduction.

CPE_1, with an exponent of close to 0.5, represents diffusive transport processes[1]. Its impedance decreases with increasing humidity, consistent with increasing humidity dependent conduction at higher humidities.

CPE_2 has a negative exponent, therefore representing an inductive-type process. In fact the occurrence of an inductance is only an apparent effect, since a real inductance would involve the storage of energy in a magnetic field and there is no appreciable magnetic field energy present in low-current IS measurements[1]. Yeh et al state that such an inductive effect, as observed in other ceramic systems, is consistent with the regeneration of adsorption sites on the sample surface, which occur due to a water vapour desorption reaction[9]. However it is not clear that desorption would result in such an effect. This behaviour in fact represents an inductive type phase shift and could be due to any process which causes the current to lags the voltage. Such an effect could arise from the trapping of electrons by defects, giving rise to a delay in current response and

resonance between trapping rates and polarization. The inductive effects of CPE_2 are notably stronger at lower humidities, which could be due to such trapping effects becoming more significant as the number of charge carriers is lower.

The distributed element CPE_3 was chosen to represent diffusive transport at the material-electrode interface. Such processes typically give rise to an impedance which is proportional to $\omega^{-1/2}$ and can therefore be represented by a Warburg Impedance[1]. The impedance of CPE_3 was found to decrease with increasing humidity, in an almost step-wise function at 57% *r.h.*, suggesting a change in electrode behaviour at about this humidity. Increasing humidity can also lower the activation energy of the material causing more electrons to pass through the electrode interface[10,19], although this process could be expected to be continuous rather than step-wise.

The capacitance of a parallel plate capacitor is given by:

$$C = \frac{\varepsilon_0 \varepsilon_r A}{l} \qquad (5.15)$$

where ε_0 is the permittivity of free space, 8.854×10^{-12} F m^{-1}, ε_r is the relative permittivity of the material between the plates, typically ≈ 10 for a ceramic material[2], A is the area of the plates and l their separation distance. Considering a pellet sample of Zn_2GeO_4, with the electrode arrangement as shown in Figure 5.2, l is 1 mm and A is 15 mm^2 (30 mm, times the thickness of the surface layer in which conduction takes place, $\approx$ 0.5 mm). This gives a value of 1.3×10^{-12} F, in good agreement with the value of the ideal capacitor in the equivalent circuit, C_1. This could indicate that C_1 is almost entirely due to the bulk capacitance of the material. However C_1 was found to be constant for all humidities and the capacitance of the ceramic material could be expected to vary with the adsorption of water. So it is thought that this capacitance arises mainly from artifactual effects of the measuring system, which would not be dependent on atmospheric humidity.

5.6 SUMMARY

The impedance spectra show a superficial resemblance to the characteristics of a simple RC low pass filter. At low frequencies the impedance is independent of frequency and decreases with increasing humidity. At high frequencies the impedance is independent of humidity, exhibiting a characteristic roll off, forming a limiting characteristic inversely proportional to ω. The break point frequency is also a function of humidity. A small maximum is observed just before the break point frequency, becoming more pronounced as humidity decreases. As with the DC resistivity behaviour there is no systematic variation in the impedance with composition.

Complex impedance analysis revealed that the behaviour of Z' can be explained quite well by a simple RC equivalent circuit, however the characteristics of Z" cannot and these indicate non-Debye capacitive behaviour, leading to a more complex equivalent circuit. Z' is proportional to ω^{-2} at high frequencies and is independent of ω at low frequencies whilst Z" is inversely proportional to ω at high frequencies, proportional to $\omega^{-1/2}$ at low frequencies and in the transition region it is proportional to ω^{μ}, where $\mu \approx 2$.

Plots of the locus of the impedance with frequency on the complex plane were generally in the form of a distorted semicircle at the high frequency end and a tail at low frequencies, where the distorted semicircle is indicative of the behaviour of dispersive circuit elements. The intersection between the high frequency semicircle and the low frequency tail is apparent as a loop which becomes more pronounced with decreasing humidity. This is indicative of a process producing an inductive-type phase shift and resulting in resonance with the capacitive components of the system. The inductive-type behaviour also accounts for the shallow maximum at the break point frequency in the impedance spectra. At high values of humidity the low frequency tail appears as an almost straight line, inclined at approximately 45°, corresponding to a Warburg impedance, characteristic of diffusive type transport processes. At lower humidities the straight line tail is not apparent.

An equivalent circuit, as shown in Figure 5.8, was found to represent the experimental data. The equivalent circuit consists of a series combination of a resistor, R_1, and a constant phase element, CPE_2, with a constant phase element, CPE_1, in parallel representing the humidity dependent conductivity of the material. R_1 represents the ideal, resistive components of the humidity dependent conduction, decreasing with increasing humidity. CPE_1 and CPE_2 represent the dispersive, non-Debye components of the humidity-dependent conduction. CPE_1, with an exponent of close to 0.5, represents humidity dependent diffusive transport processes[1]. CPE_2 has a negative exponent and represents an inductive-type process, such as charge trapping at defect sites. The inductive effects of CPE_2 are notably stronger at lower humidity.

A third constant phase element in the equivalent circuit, CPE_3, is in series with the combination described above. It is characterized by an exponent of 0.5, typical of a Warburg impedance, and represents the diffusive transport which occurs at the material-electrode interface[1]. The impedance of CPE_3 decreases with increasing humidity, consistent with the adsorption of water molecules at the electrode interface giving rise to an increase in conductivity with increasing humidity.

An ideal capacitor, C_1, is in series with the other elements in the circuit. It represents the overall geometric capacitance of the material-electrode system plus any artifactual effects due to the measuring system. This is a system effect which is not affected by atmospheric humidity, and has a value of approximately 10^{-12} F.

REFERENCES

[1]J. R. Macdonald, *Impedance Spectroscopy* (Wiley, New York, 1987).

[2]J.T.S. Irvine, D.C. Sinclair, and A.R. West, "Electroceramics: Characterisation by impedance spectroscopy", Advanced materials, **2**, 132-138 (1990).

[3]M. J. Hogan, A. W. Brinkman, and T. Hashemi, "Humidity dependant impedance in porous spinel nickel germanate ceramic", App. Phys. Lett., **72** (23), 3077-3079 (1998).

[4]M. J. Hogan, A. W. Brinkman, and T. Hashemi, "Sintering and humidity dependent resistivity of spinel Ni_2GeO_4", J. Am. Ceram. Soc., **In Press** (1998).

[5]G. Gusmano, G. Montesperelli, P. Nunziante and E. Traversa,"Study of the conduction mechanism of $MgAl_2O_4$ at different environmental humidities", Electrochim. Acta, **38** (17), 2617-2621 (1993).

[6]G. Gusmano, G. Montesperelli, P. Nunziante and E. Traversa, "Microstructure and electrical-properties of $MgAl_2O_4$ and $MgFe_2O_4$ spinel porous compacts for use in humidity sensors", Brit. Ceram. Trans, **92** (3), 104-108 (1993).

[7]G. Gusmano, G. Montesperelli, P. Nunziante and E. Traversa, "Humidity sensitive electrical response of sintered $MgFe_2O_4$", J. Mater. Sci., **28**, 6195-6198 (1993).

[8]M. E. V. Costa, P. Q. Mantas, and J. L. Baptista, "Effect of electrode alterations on the a.c. behaviour of Li_2O-ZnO humidity sensors", Sens. & Act., **B** (26-27), 312-314 (1995).

[9]Y-C. Yeh, T-Y. Tseng, and D-A. Chang, "Electrical properties of porous titania ceramic humidity sensors", J. Am. Ceram. Soc., **72** (8), 1472-1475 (1989).

[10]Y-C. Yeh, T-Y. Tseng, and D-A. Chang, "Electrical properties of TiO_2-$K_2Ti_6O_{13}$ porous ceramic humidity sensor", J. Am. Ceram. Soc., **73** (7), 1992-1998 (1990).

[11]A. Jonscher, "Interpretation of non-ideal dielectric admittance and impedance diagrams", Phys. Status Solidi A, **32A**, 665-676 (1975).

[12]B. M. Lacquet and P. L. Swart, "A new electrical circuit model for porous dielectric humidity sensors", Sens. & Act. B, **17** (1), 41-46 (1993).

[13]J.H. Anderson and G.A. Parks, "The electrical conductivity of silica gel in the presence of adsorbed water", J. Phys. Chem, **72**, 3662-3668 (1968).

[14]E. Traversa, "Ceramic sensors for humidity detection: the state-of-the-art and future developments", Sens. & Act. B, **23**, 135-156 (1995).

[15]J.G. Fagan and V.R.W. Amarakoon, "Reliability and reproducibility of ceramic sensors: part III, humidity sensors", Am. Ceram. Soc. Bull., **72** (3), 119-130 (1993).

[16]B. M. Kulwicki, "Humidity sensors", J. Am. Ceram. Soc., **74** (4), 697-708 (1991).

[17]T. Seiyama, N. Yamazoe, and H. Arai, "Ceramic Humidity Sensors", Sens. & Act., **4** (1), 85-96 (1983).

[18]Y. Shimizu, H. Arai, and T. Seiyama, "Theoretical studies on the impedance-humidity characteristics of ceramic humidity sensors", Sens. & Act., **7**, 11-22 (1985).

CHAPTER 6

GENERAL DISCUSSION AND CONCLUSIONS

6.1 MATERIALS

Two solid solution phases were identified in the $Zn_xCo_{2-x}GeO_4$ system. At the Zn_2GeO_4 end of the compositional range a solid solution phase was found to extend from x = 2 to $x \approx 1.68$, for materials fired at 1200°C. This corresponds to the solid solution phase, with phenacite structure, known to occur from x = 2 to x = 1.6. At the Co_2GeO_4 end of the compositional range a solid solution series was detected from x = 0 to x between 0.65 and 0.78, for material fired at 1200°C. In fact this compositional range spans two solid solution series, a normal spinel solid solution phase, from x = 0 to x = 0.2, and an inverse spinel solid solution phase, from x = 0.6 to x = 0.9, and also a mixed phase region, from x = 0.2 to x = 0.6, consisting of both the normal and inverse spinel phases. The lattice parameters of the two spinel phases are 0.832 nm and 0.835 nm respectively. There is little or no variation in the lattice parameters with composition across either of the solid solution series.

Co_2GeO_4 has a cubic spinel structure and Zn_2GeO_4 has a hexagonal phenacite structure. These two structural types are fairly similar, both consisting of oxygen ions in closest packing with the positive ions filling some of the octahedral and tetrahedral interstitial spaces. The occurrence of solid solutions within the system was expected due to the structural similarities of the two materials and the small difference between the ionic radii of Co^{2+} and Zn^{2+} (0.72 nm and 0.74 nm).

The theoretical density of Co_2GeO_4, 5.825×10^3 kg m^{-3}, is greater than that of Zn_2GeO_4, 4.709×10^3 kg m^{-3}, (see section 3.3.3) in spite of the lower mass number of Co, and therefore can only be attributed to their respective structures. The hexagonal,

phenacite structure of Zn_2GeO_4 is more open than the cubic spinel structure of Co_2GeO_4 and is consequently less dense.

The percentage of the theoretical density was found to increase with increasing Co_2GeO_4 content, from 47% for Zn_2GeO_4 to 57% for Co_2GeO_4. This is due to the fact that Co_2GeO_4 undergoes liquid phase sintering, which is a more effective sintering mechanism than the evaporation/ condensation mechanism undergone by Zn_2GeO_4. The percentage of theoretical density was taken as a measure of the porosity of the samples, giving a range from 53% for Zn_2GeO_4 to 43% for Co_2GeO_4. These values represent total porosity, which includes both open and closed pores, although only open pores are effective in the process of humidity sensing.

6.2 ELECTRICAL PROPERTIES

The charge carriers in a humid atmosphere were determined to be both ions and electrons. The charging currents resulting from the application of a potential difference to samples of $Zn_xCo_{2-x}GeO_4$ were found to decrease rapidly in the first few seconds, then to decay more slowly over a period of tens of minutes and to reach a steady state value after about 40 minutes. The charging process observed is thought to involve defect traps and polarization sites in the material, which on the application of a direct current will accumulate a small amount of charge.

The resistivity of $Zn_xCo_{2-x}GeO_4$ decreased by 1 to 2 orders of magnitude with increasing temperature from 10 to 80°C. The activation energy of the humidity independent conductivity of the material was 0.9 eV and varied little with composition. The activation energy was relatively high compared to the typical activation energy of an NTC-thermistor, 0.2 to 0.5 eV. Zn_2GeO_4 is a dielectric material with a band gap (Eg) of 4.8 eV. (The energy gap of Co_2GeO_4 is not known but is assumed to be equally wide.) The observed conduction process cannot therefore be intrinsic, since that would

give an activation energy equal to half the band gap, i.e. 2.4 eV. A variable range hopping mechanism has been reported in other oxide materials with humidity dependent resistivity, but does not seem likely in the present case since it would give rise to a temperature dependence of $exp\ (\ E\ /\ kT^{1/4}\ )$ which was not observed in this case. Conduction is thought to be defect related and probably due to some deep donor-like level.

The resistivity of $Zn_xCo_{2-x}GeO_4$ decreased with increasing relative humidity, by 4 to 5 orders of magnitude, from 10% to 98% *r.h.* and decreased exponentially from 40 to 70% *r.h.* The humidity dependent resistivity of $Zn_xCo_{2-x}GeO_4$ showed no systematic variation with composition.

It was initially thought that the variation in structural phases with composition would affect the resistivity. However this was not found to be the case, probably because the dry conductivity of the material was negligibly small, compared with the humidity-dependent conductivity. The latter is governed by those properties of the material which determined the amount of water adsorption, i.e. surface area and porosity.

The impedance spectra for $Zn_xCo_{2-x}GeO_4$ were resistance-dominated at low frequencies and capacitance-dominated at high frequencies. At low frequencies the impedance was a function of humidity, behaving in a similar way to the DC resistivity, decreasing almost exponentially with increasing humidity and showing no systematic variation with composition. At high frequencies the impedance was independent of humidity, exhibiting a first order roll off, forming a limiting characteristic inversely proportional to ω. The break point frequency appeared to be a function of humidity, however this was determined eventually, by the RC constant of the device, to be a consequence of the strong humidity dependence of the resistive part of the characteristic.

A small maximum was observed just before the break point frequency, indicative of inductive-type behaviour, which become more pronounced as the humidity decreased. The reason for this apparent inductive behaviour was not clear. Such maxima are

generally the result of resonance between capacitive-like and inductive-like effects. None of the components in the system are ferromagnetic, so 'magnetic' effects can probably be ruled out. Similarly the material is not thought to be piezoelectric, so electrically induced strain effects can also be ruled out. However resonance arises in LC circuits from the opposite phase relationships of the two components and one could speculate that some of the charge transfer and charge storage processes involved in the system here do become out of phase with each other, particularly when dispersive components exist.

Complex impedance analysis revealed that the behaviour of Z', its independence of ω at low frequencies and its dependence on ω^{-1} at high frequencies, could be explained quite well by a simple RC equivalent circuit. However, the characteristics of Z'' at low frequencies, where it was proportional to $\omega^{-1/2}$, indicated non-Debye capacitive behaviour, leading to a more sophisticated equivalent circuit.

6.3 MODEL FOR HUMIDITY - DEPENDENT CONDUCTIVITY

The complex impedance plots for $Zn_xCo_{2-x}GeO_4$ have three distinct characteristics, a distorted semicircle at high frequencies, a tail at low frequencies, which for high humidities forms a straight line inclined at approximately 45°, and, at the intersection between the high frequency-semicircle and the low frequency-tail, a loop, indicative of an inductive-type process, becoming more pronounced with decreasing humidity.

An equivalent circuit, as shown in Figure 5.8, was developed to represent the experimental data. The equivalent circuit consisted of a series combination of a resistor, R_1, and a constant phase element, CPE_2, in parallel with a constant phase element, CPE_1, representing the humidity dependent conductivity of the material. R_1 represents the ideal, resistive components of the humidity dependent conduction, decreasing with increasing humidity. CPE_1 and CPE_2 represent the dispersive, non-

Debye components of the humidity-dependent conduction. CPE_1, with an exponent of close to 0.5, would indicate a humidity dependent diffusive transport processes operating in addition to the Warburg impedance CPE_3, chosen to account for expected contact effects. CPE_2 has a negative exponent and corresponds to an inductive-type process, in the sense that it has opposite phase to the normal capacitive processes. It has been suggested in the literature that this could arise from the regeneration of adsorption sites on the sample surface due to a water vapour desorption reaction. However it is not clear how desorption could result in such an effect. The behaviour represented by CPE_2 could however result from any process giving rise to an inductive-type phase shift. Such an effect could arise from the trapping of electrons by defects which would give rise to a delay in the current response and resonance between trapping rates and polarization. The inductive effects of CPE_2 are notably stronger at lower humidities which could be due to the trapping effects becoming more significant as the number or charge carriers becomes smaller.

A third constant phase element in the equivalent circuit, CPE_3, is in series with the combination described above. This was chosen to represent the diffusive transport processes believed to occurs at the material-electrode interface. It is characterized by a frequency dependence of $\omega^{-1/2}$, typical of a Warburg impedance. The impedance of CPE_3 decreases with increasing humidity, consistent with the adsorption of water molecules at the electrode interface giving rise to an increase in conductivity with increasing humidity.

An ideal capacitor, C_1, with a value of approximately 10^{-12} F, is in parallel with the other elements in the circuit. This was proposed to represent the overall geometric capacitance of the material-electrode system plus any artifactual effects due to the measuring system. It was thought there could also be a contribution form the material capacitance. However, it is expected that the capacitance of the material would vary with humidity due to the large difference between the relative permittivity of the ceramic ($\approx$10) and that of water ($\approx$80). Since C_1 does not vary with humidity it cannot involve a significant contribution from the capacitance of the material. Hence it was concluded that C_1 is entirely a system effect.

The equivalent circuit was shown to give a good fit to the experimental data for various sample compositions. It is proposed that the mechanism of conduction results from the chemisorption and physisorption of water molecules at the surface of the material. At low humidities conduction occurs by hopping of protons between adjacent hydroxyl groups formed at the material surface by the dissociative chemisorption of water molecules. At intermediate humidities conduction takes place predominantly by diffusion of physisorbed H_3O^+ ions, formed by the dissociation of physisorbed water molecules, between neighbouring hydroxyl groups. At higher humidities conduction occurs by hopping of protons from H_3O^+ ions to water molecules in the physisorbed layers. The change from conduction by diffusion of H_3O^+ ions to conduction by proton hopping is gradual and takes place as the number of adsorbed water molecules increases. Electrolytic conduction can also occur at higher humidities in layers of water condensed in capillary pores, but this is hardly significant compared to adsorption effects. Electronic conductivity also takes place by the release of electrons from chemisorbed oxygen ions and /or surface defects when water molecules are adsorbed onto the oxide surface.

6.4 COMMERCIAL POTENTIAL

Evaluation of the commercial potential of these materials would require investigation into reproducibility and ageing. Reproducibility is of utmost importance for a device to be mass produced and fitted to standard circuitry.

The main factors affecting reproducibility are the precise composition of the material, the dimensions of the samples and the porosity of the final bodies. The composition of the material can be controlled by accurate measurement of the relative proportions of the constituents, minimization of contamination during processing and the purity of the starting materials. The dimensions of the sample are controlled by processing methods and must be kept within tolerances for reproducible results. Porosity can be affected by

the particle size of the starting materials, duration and temperature of firing process and the presence of any additives. Variation in porosity can greatly affect the humidity characteristics so it must to be optimized for the required performance of the device and then controlled to give standard, reproducible results.

Ageing is also a significant factor in the performance of a device. It is important to determine the effects on the response of the material of long-term exposure to extremes of temperature, humidity and the types of contaminants to which the devices are likely to be exposed. The effects of repeated cycling through the range of operating conditions must also be evaluated.

Cost is a significant factor in a commercial device. This can be reduced by reducing the quantities of material needed in a device and is often achieved by manufacturing devices in thick film form. However this does introduce other problems such as contamination from binding vehicles. Other considerations are the optimization of electrode arrangement, the design of the circuitry and finally the housing of the device.

APPENDIX 1

Figures A1.1 to A1.8 - Resistivity versus relative humidity at temperatures of 10 to 90°C for samples of $Zn_xCo_{2-x}GeO_4$, for compositions of x = 0.2, 0.4, 0.6, 1, 1.4, 1.7, 1.8 and 1.9.

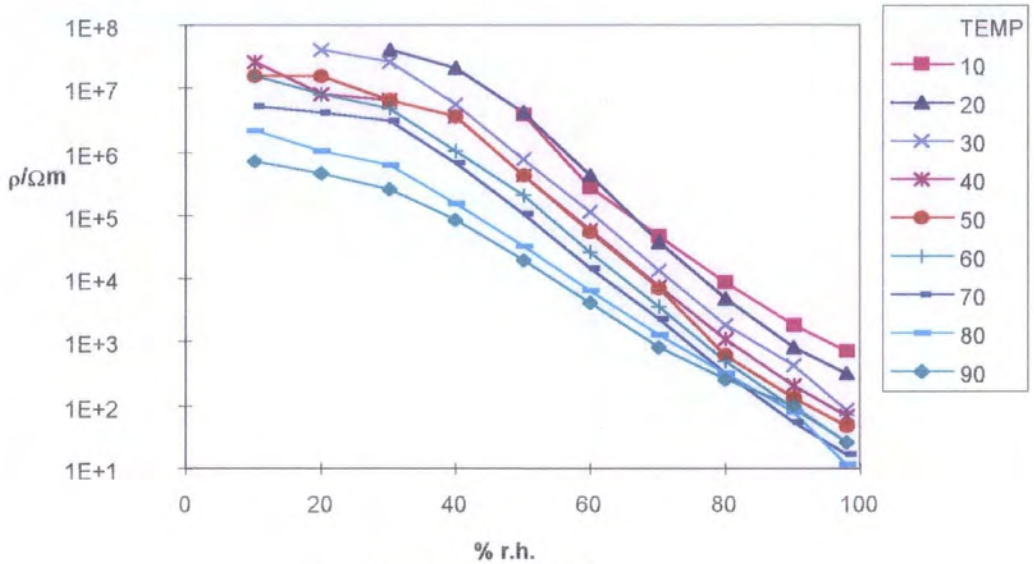

Figure A1.1 - x = 0.2

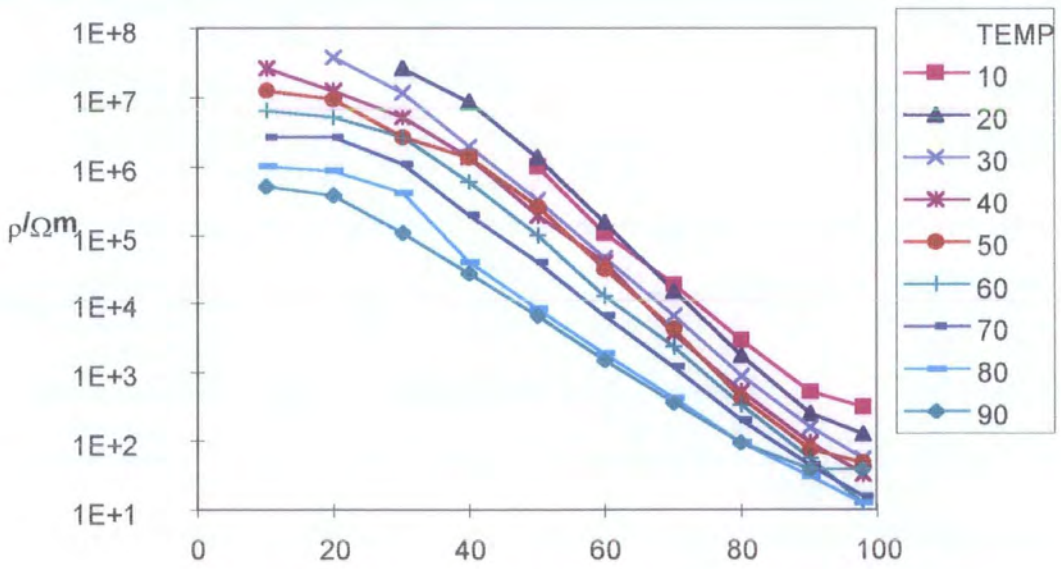

Figure A1.2 - x = 0.4

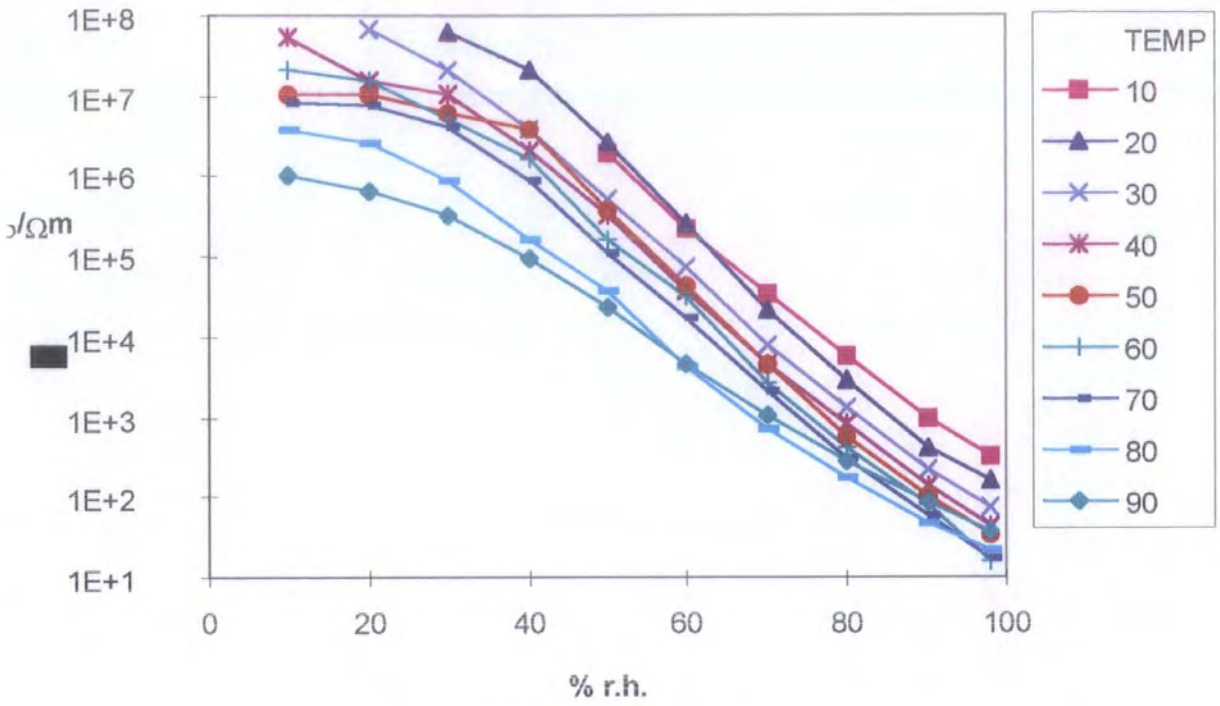

Figure A1.3 - x = 0.6

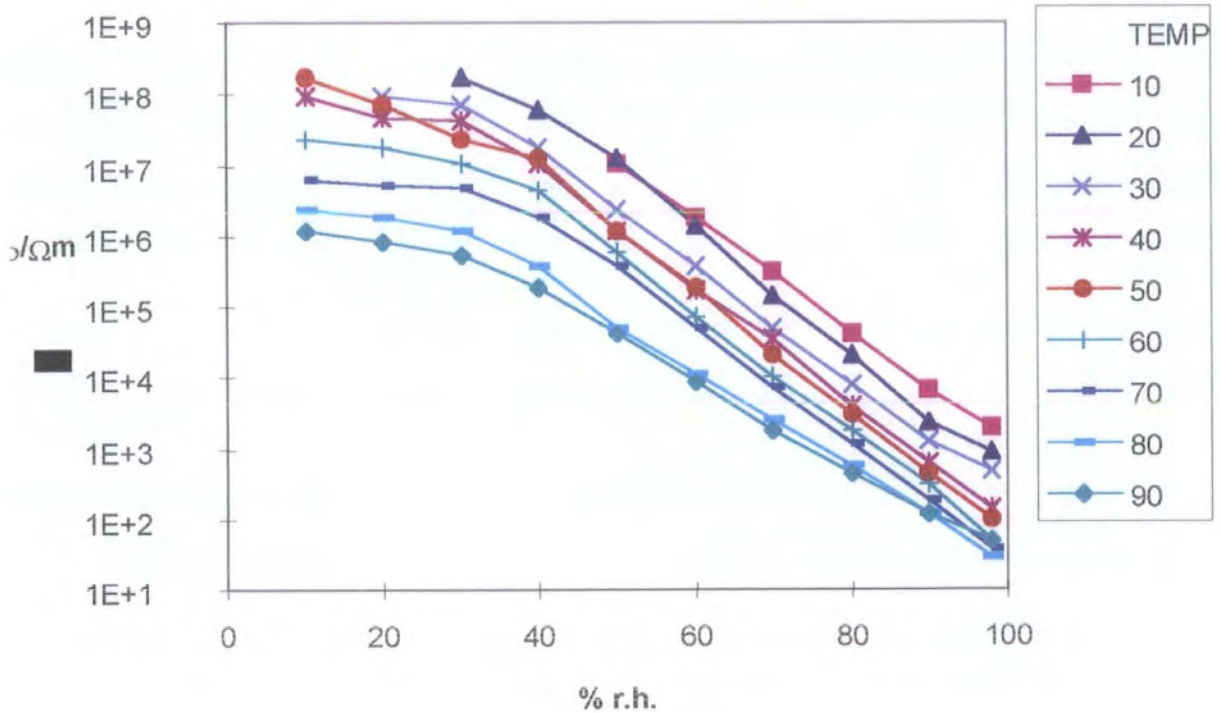

Figure A1.4 x = 1

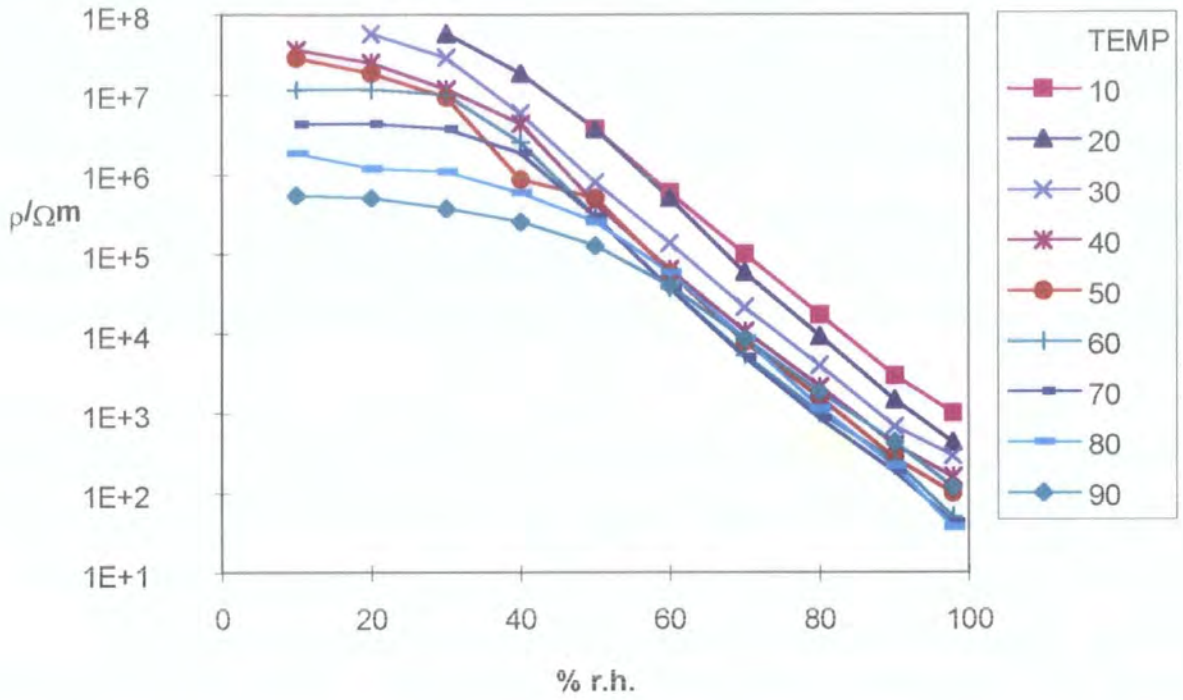

Figure A1.5 - x = 1.4

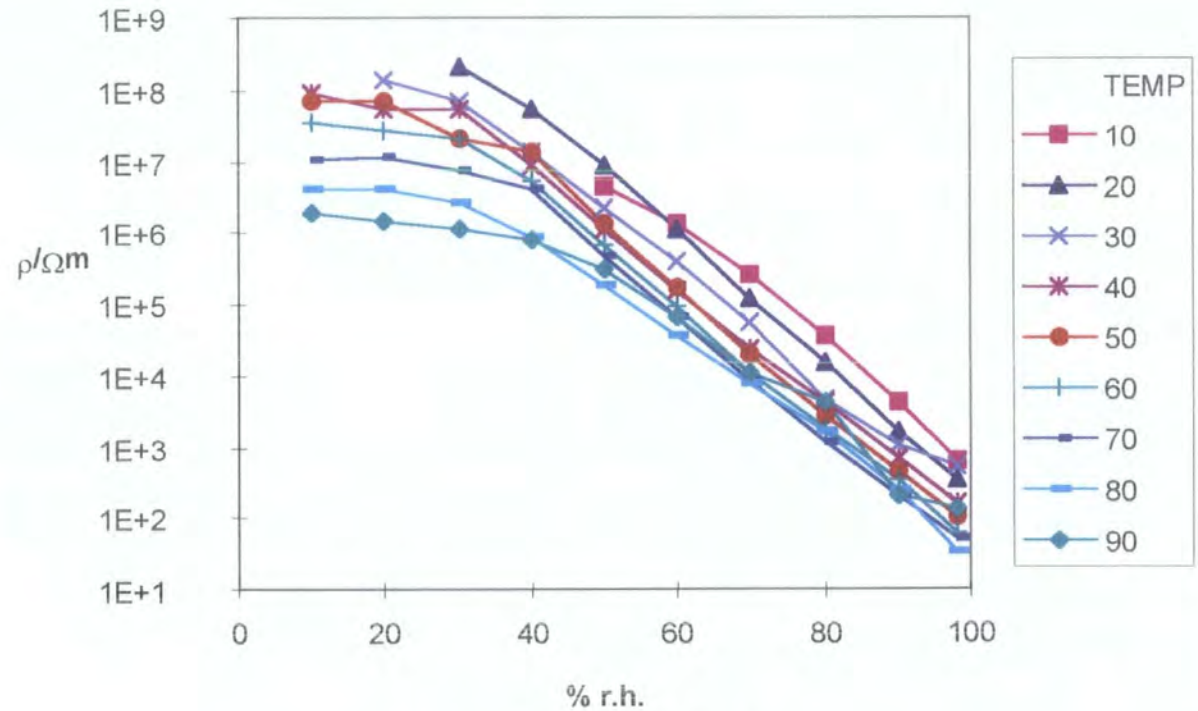

Figure A1.6 - x = 1.7

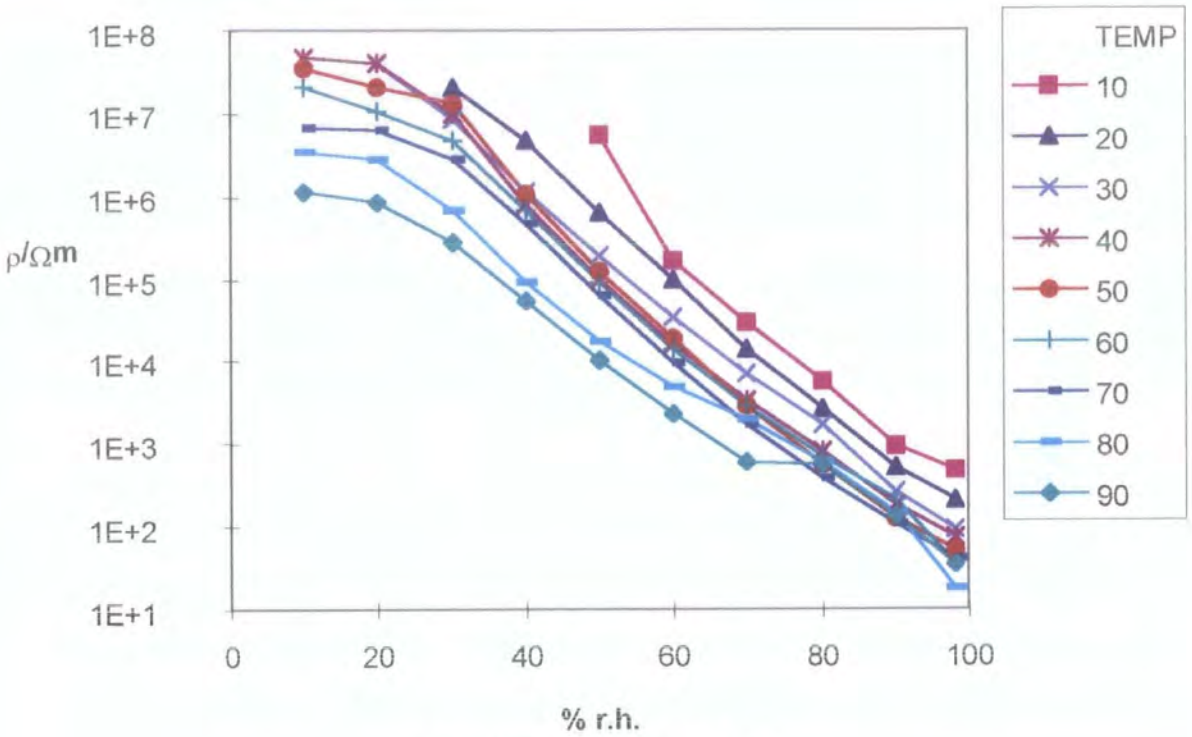

Figure A1.7 - x = 1.8

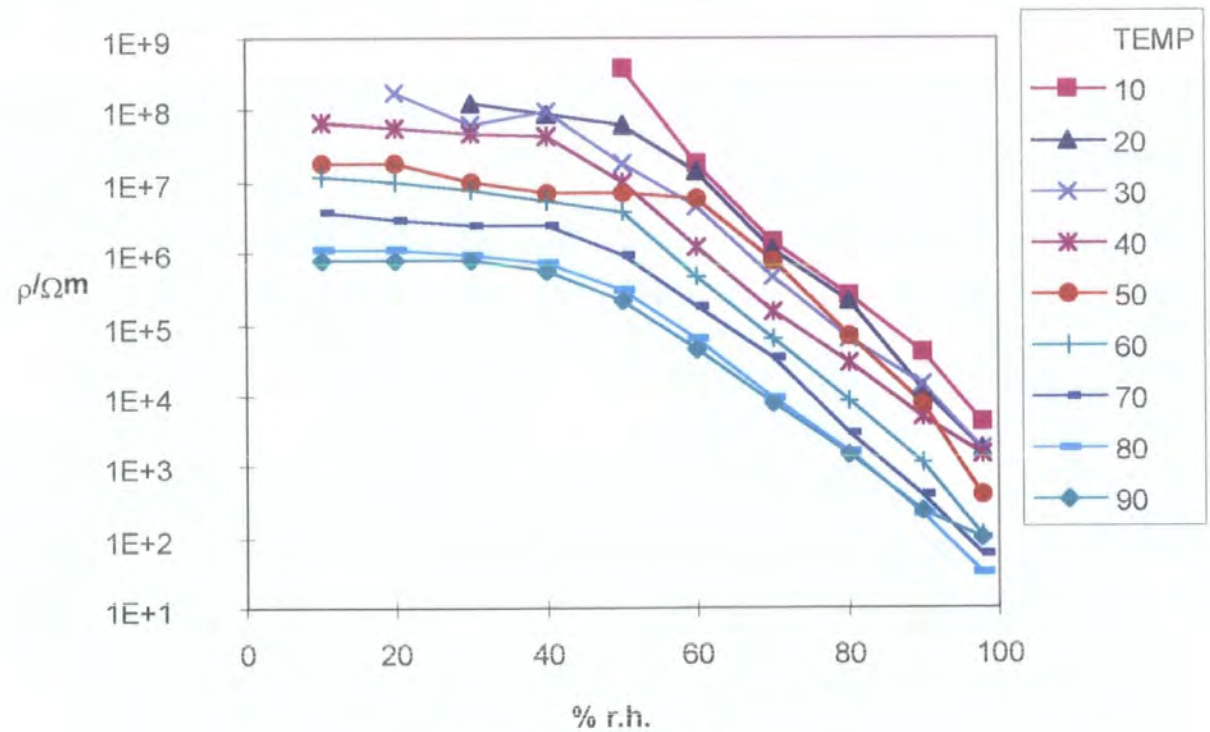

Figure A1.8 - x = 1.9

APPENDIX 2

Figures A2.1 to A2.8 - Resistivity versus temperature at humidities of 10 to 90% r.h. for samples of $Zn_xCo_{2-x}GeO_4$, for compositions of x = 0.2, 0.4, 0.6, 1, 1.4, 1.7, 1.8 and 1.9.

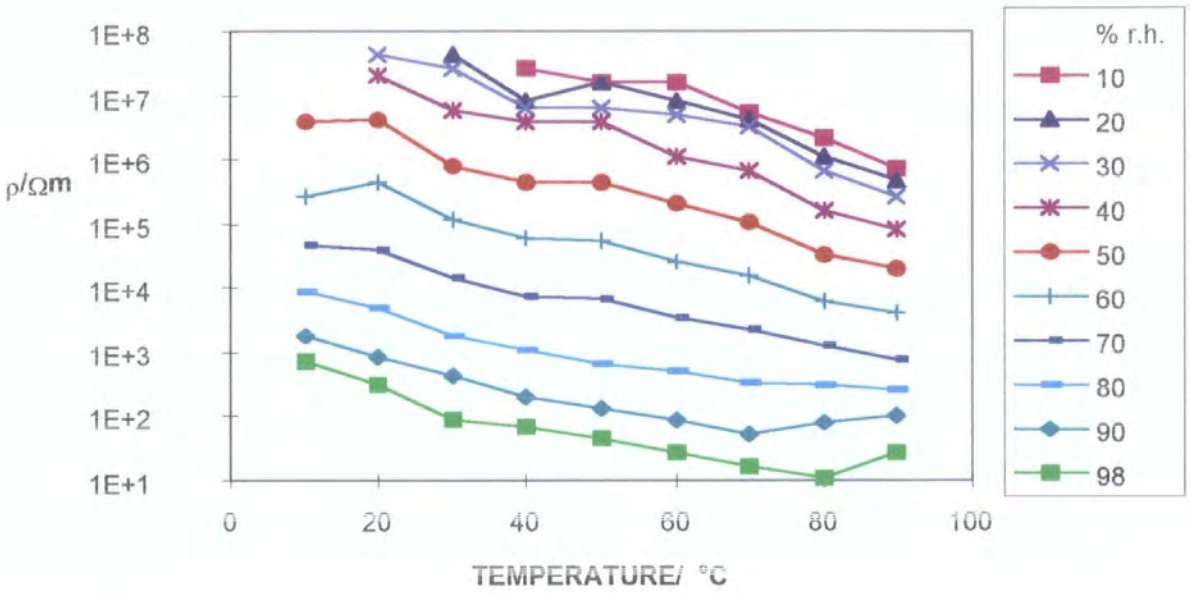

Figure A2.1 - x = 0.2

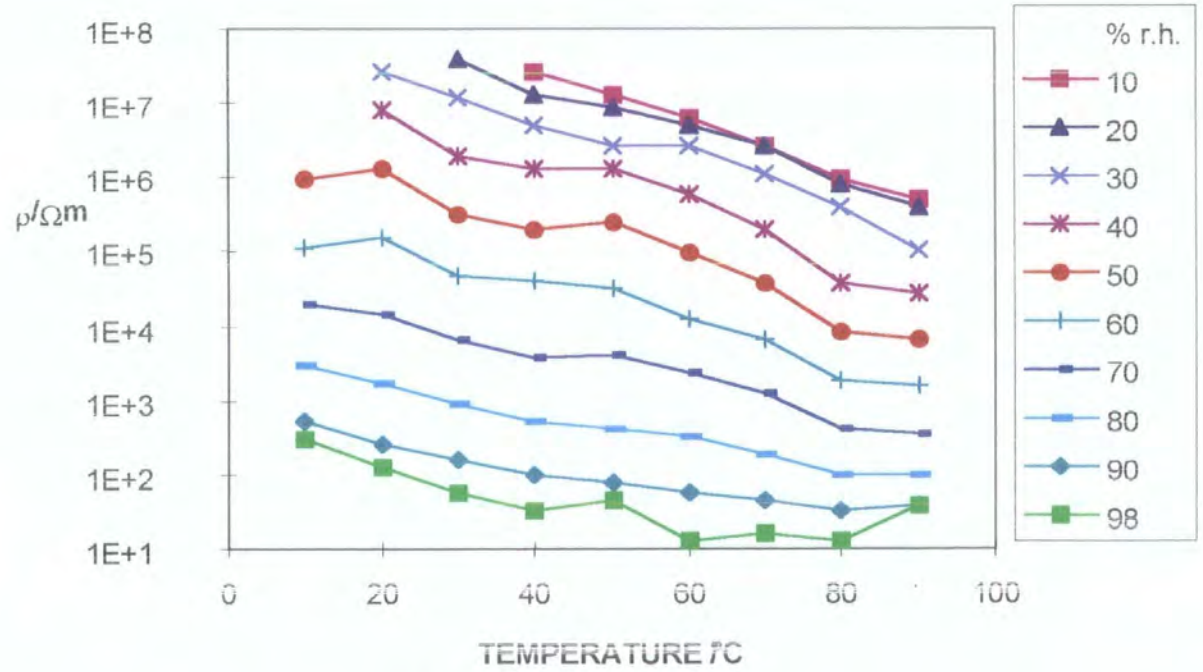

Figure A2.2 - x = 0.4

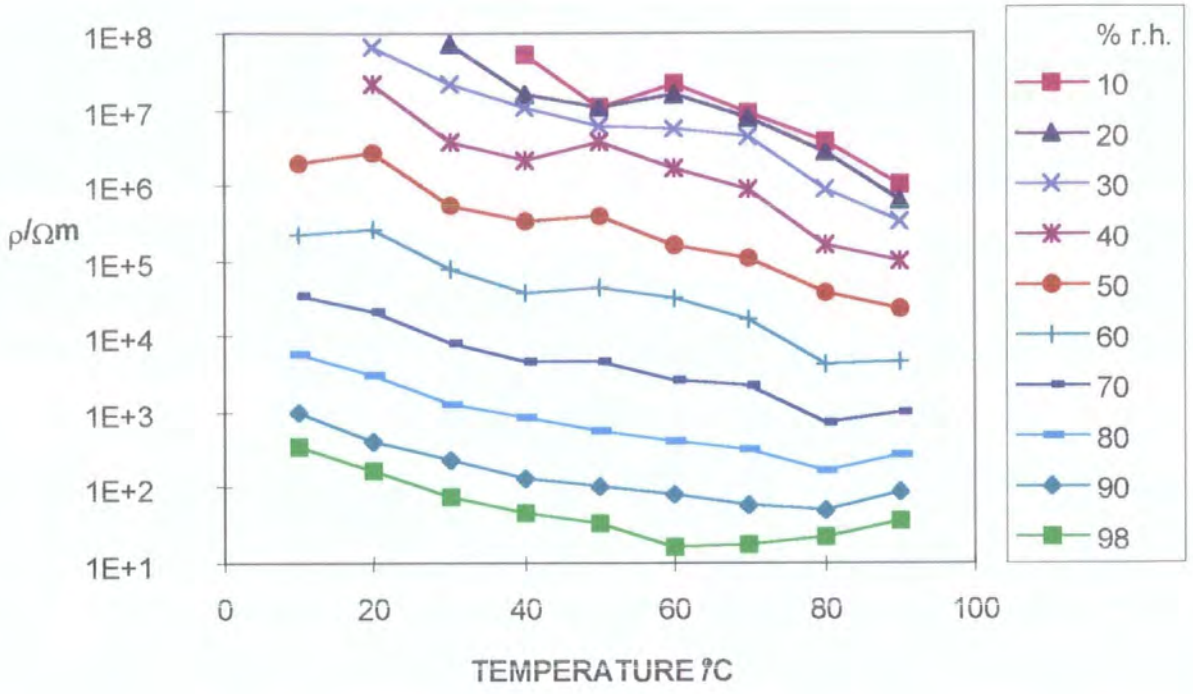

Figure A2.3 - x = 0.6

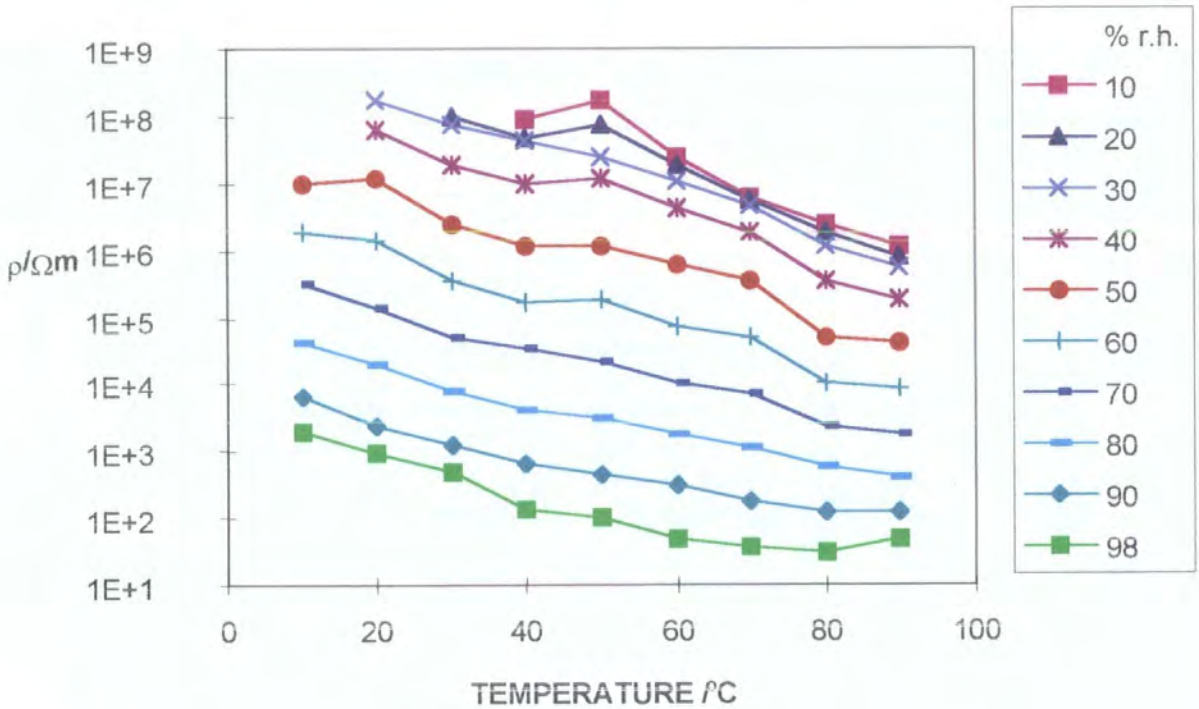

Figure A2.4 - x = 1

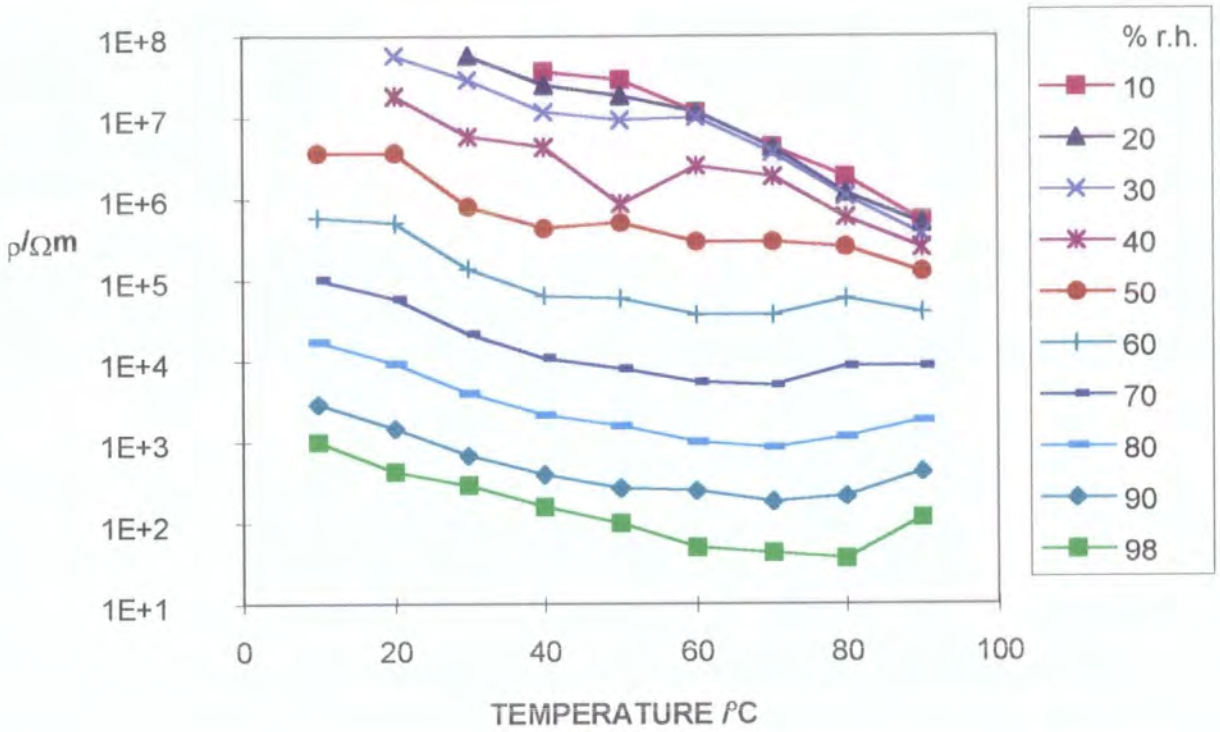

Figure A2.5 - x = 1.4

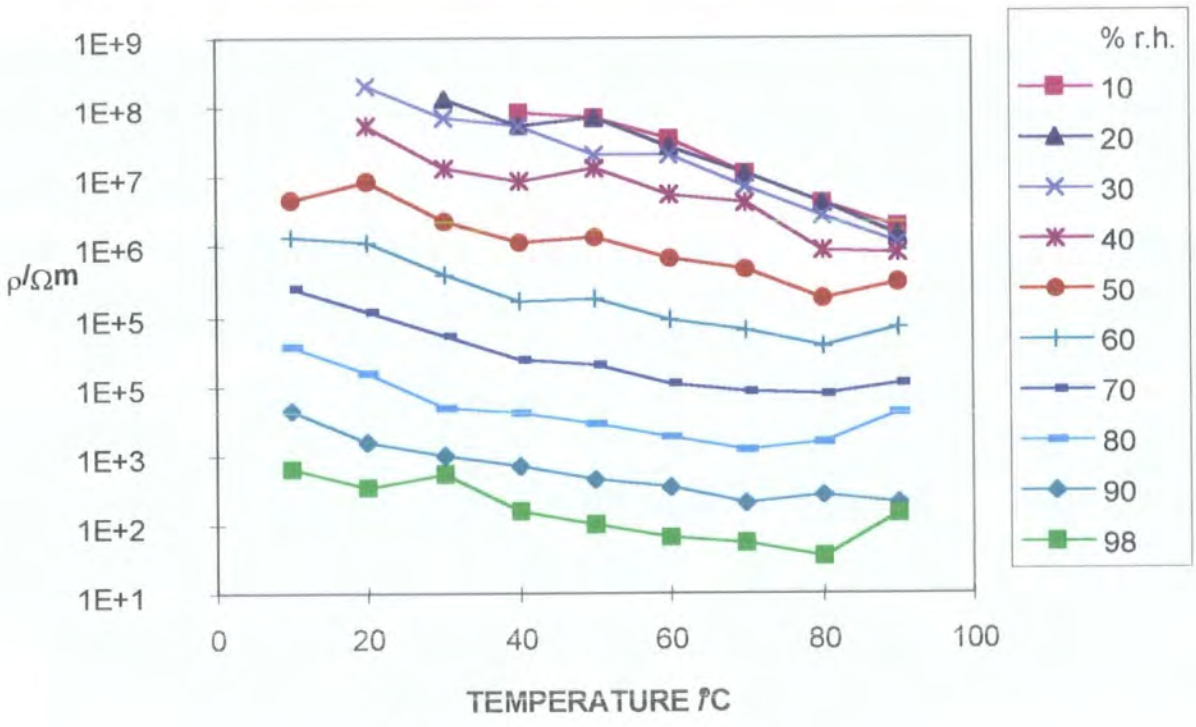

Figure A2.6 - x = 1.7

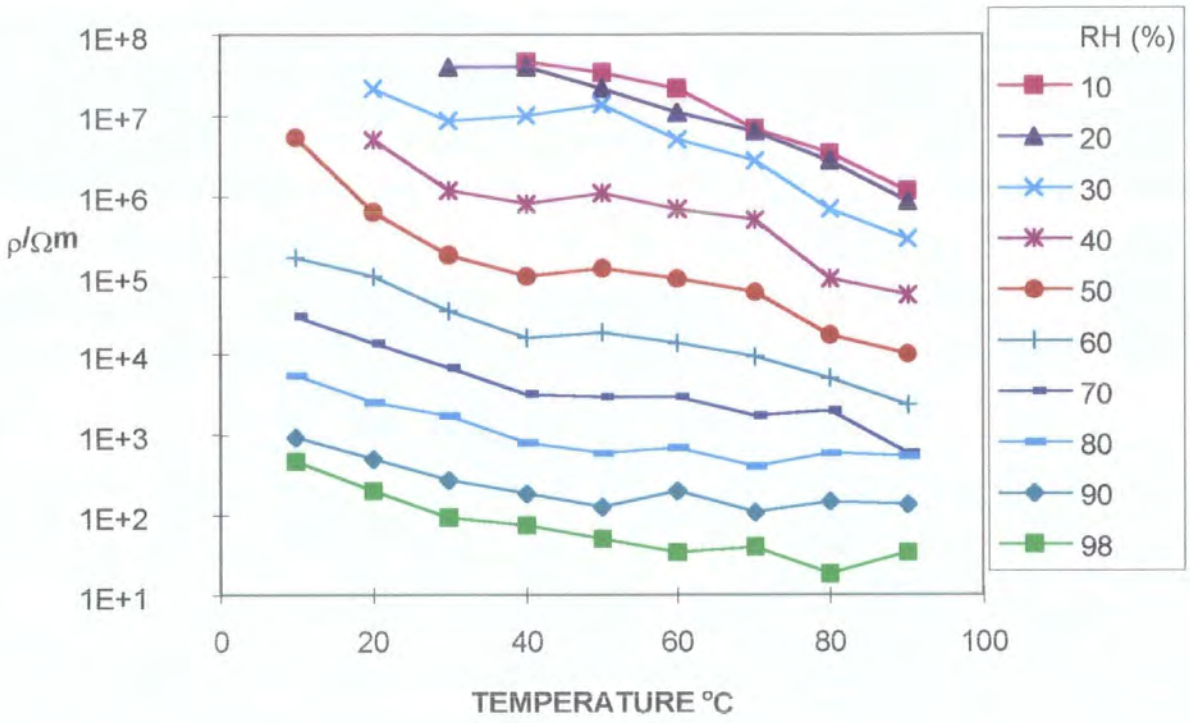

Figure A2.7 - x = 1.8

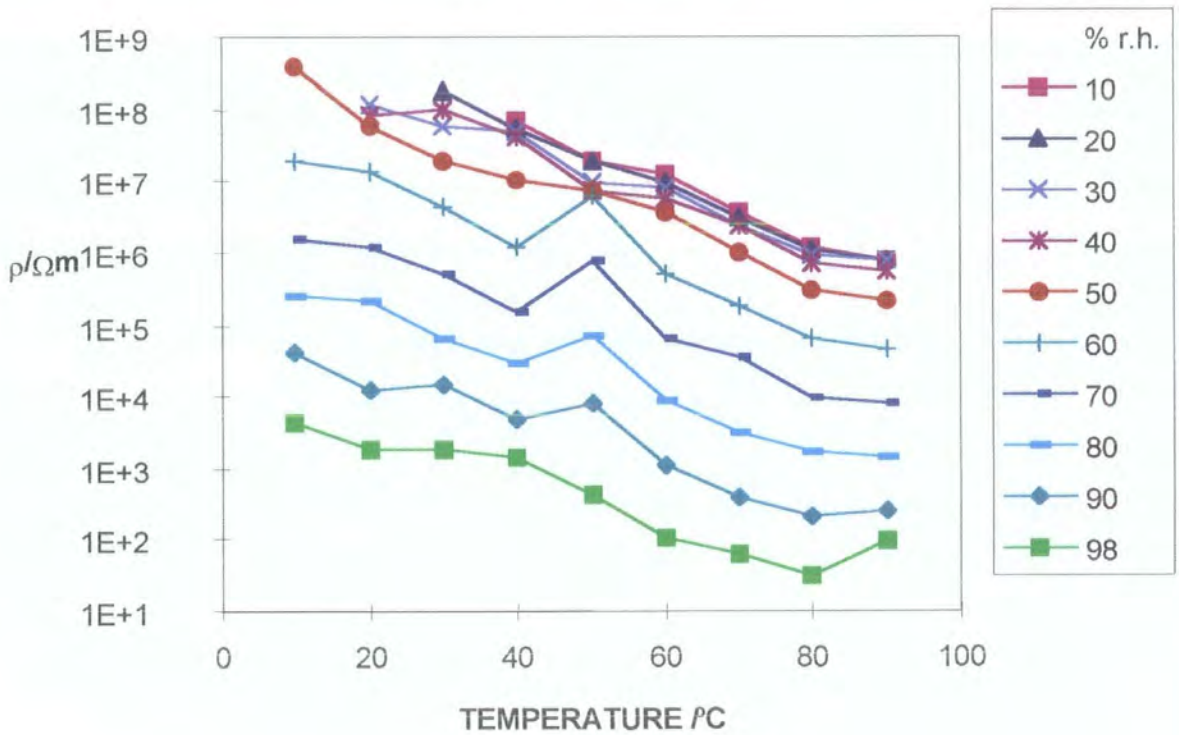

Figure A2.8 - x = 1.9

APPENDIX 3

Figures A3.1 to A3.7 - Resistivity versus composition, x, for samples of $Zn_xCo_{2-x}GeO_4$ at various humidities, for temperatures of 10 to 90°C

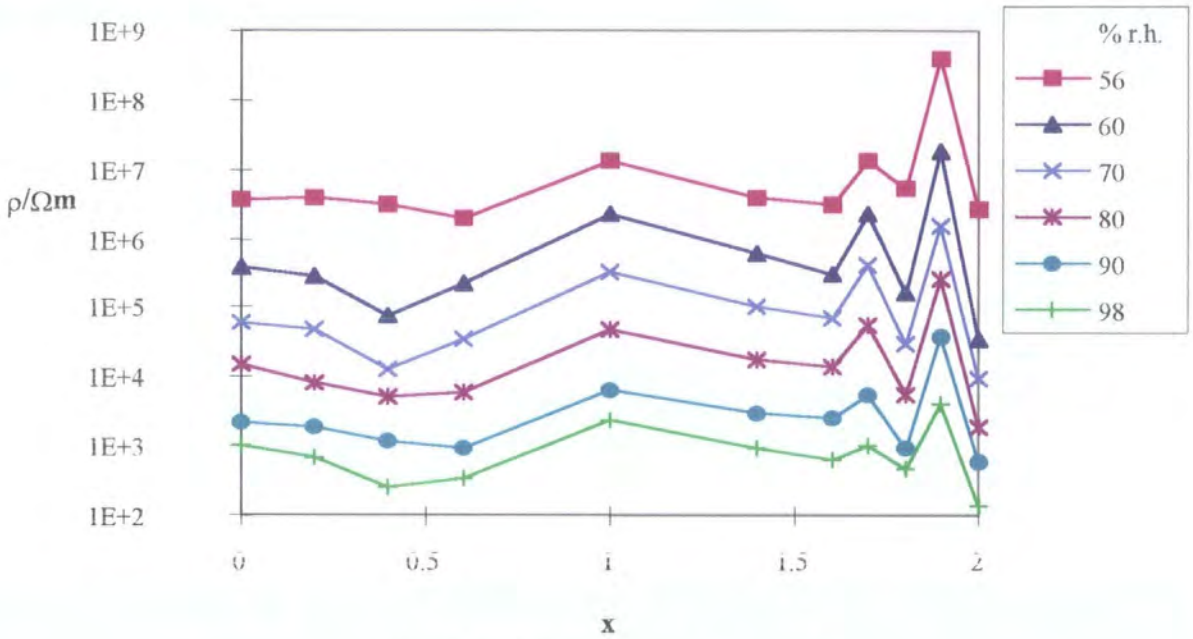

Figure A3.1 - Temperature 10 °C

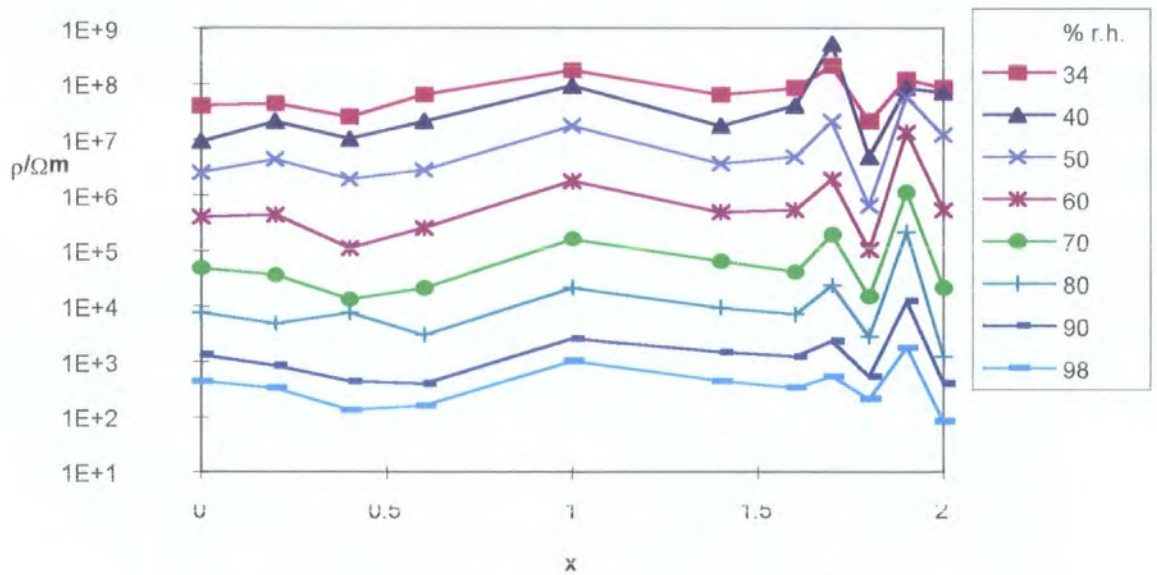

Figure A3.2 - Temperature 20 °C

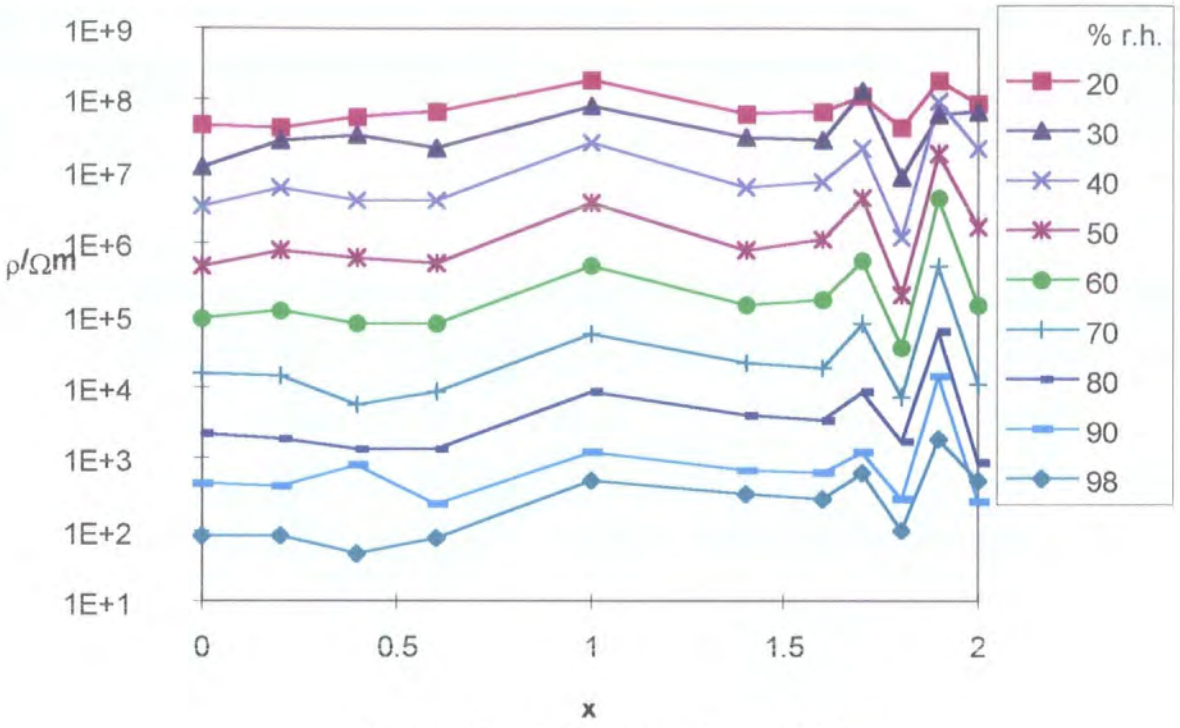

Figure A3.3 -Temperature 30 °C

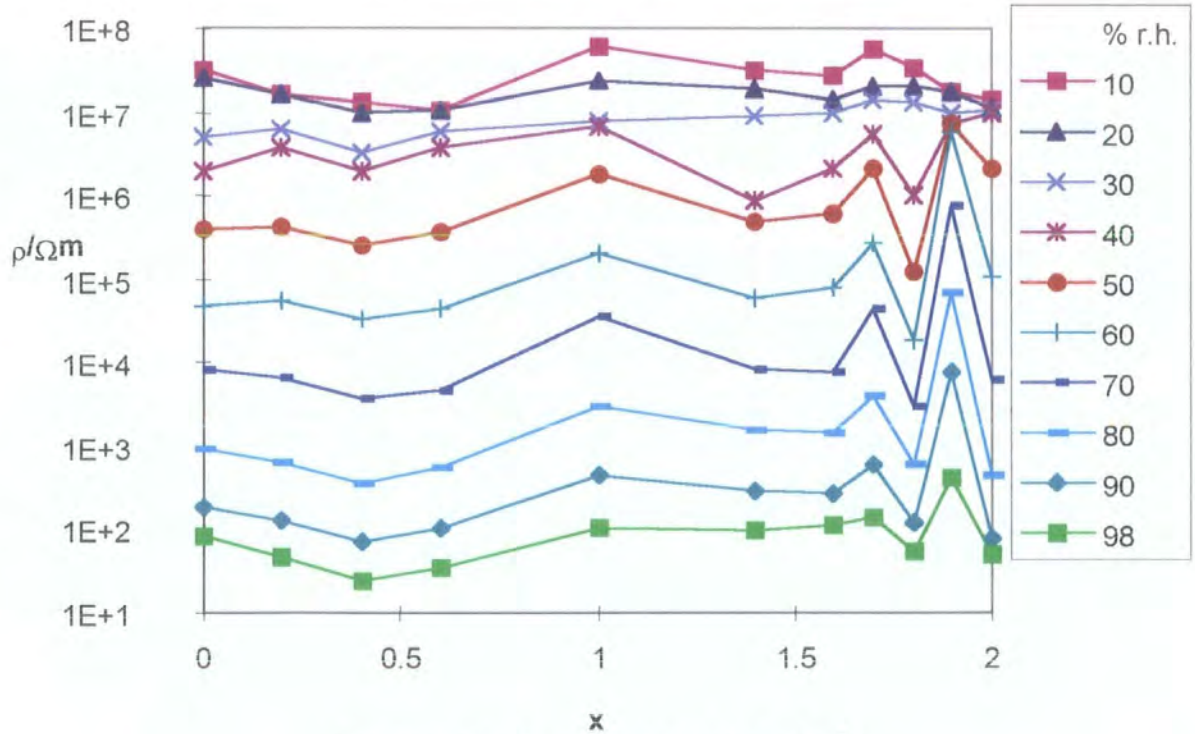

Figure A3.4 - Temperature 50 °C

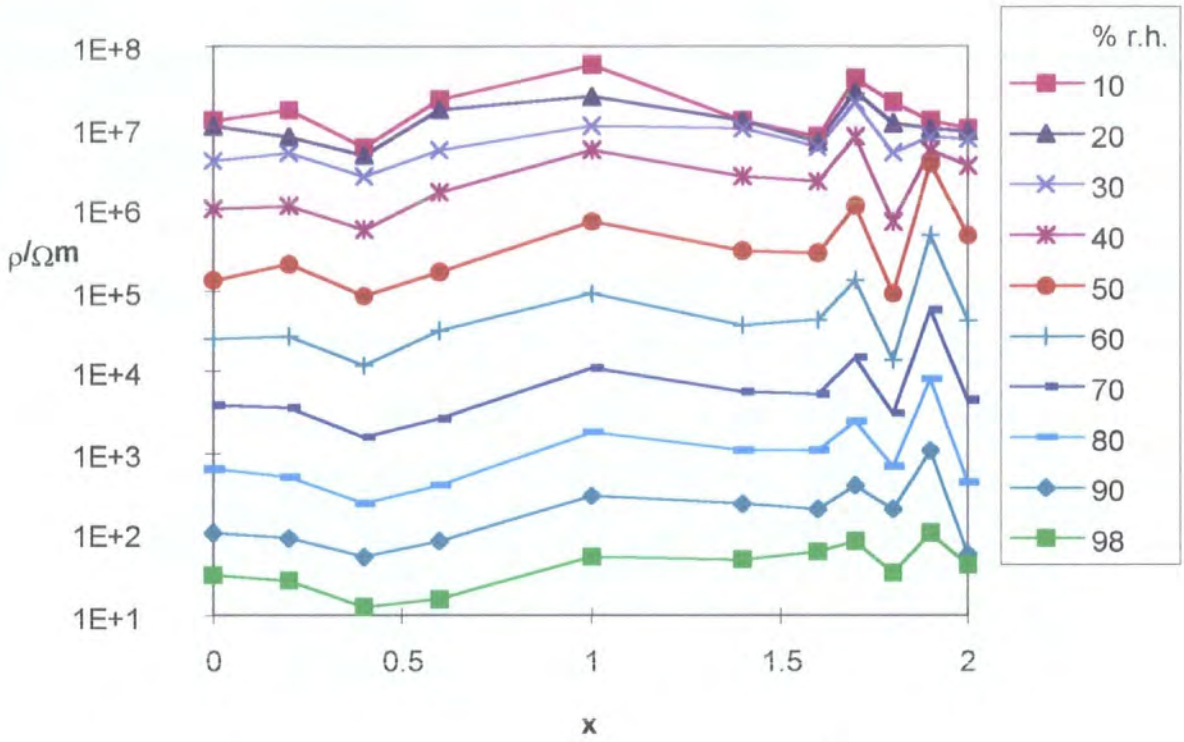

Figure A3.5 -Temperature 60 °C

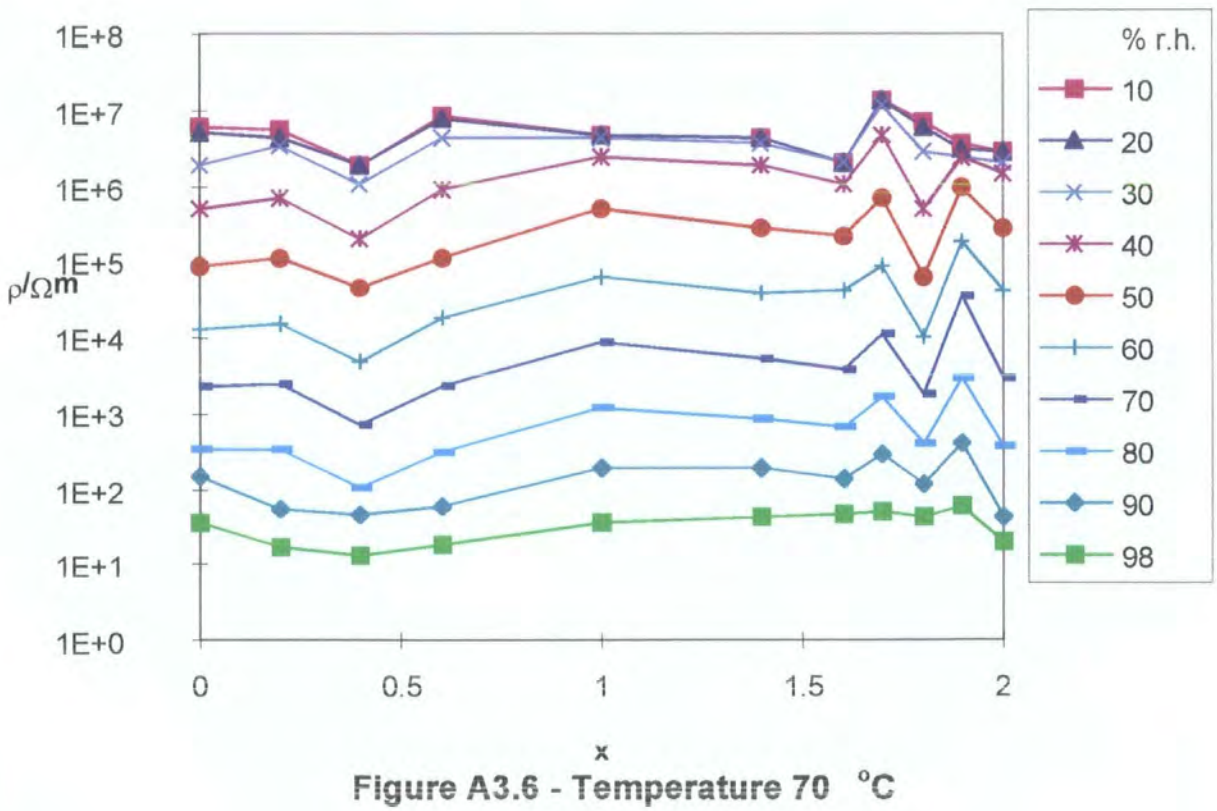

Figure A3.6 - Temperature 70 °C

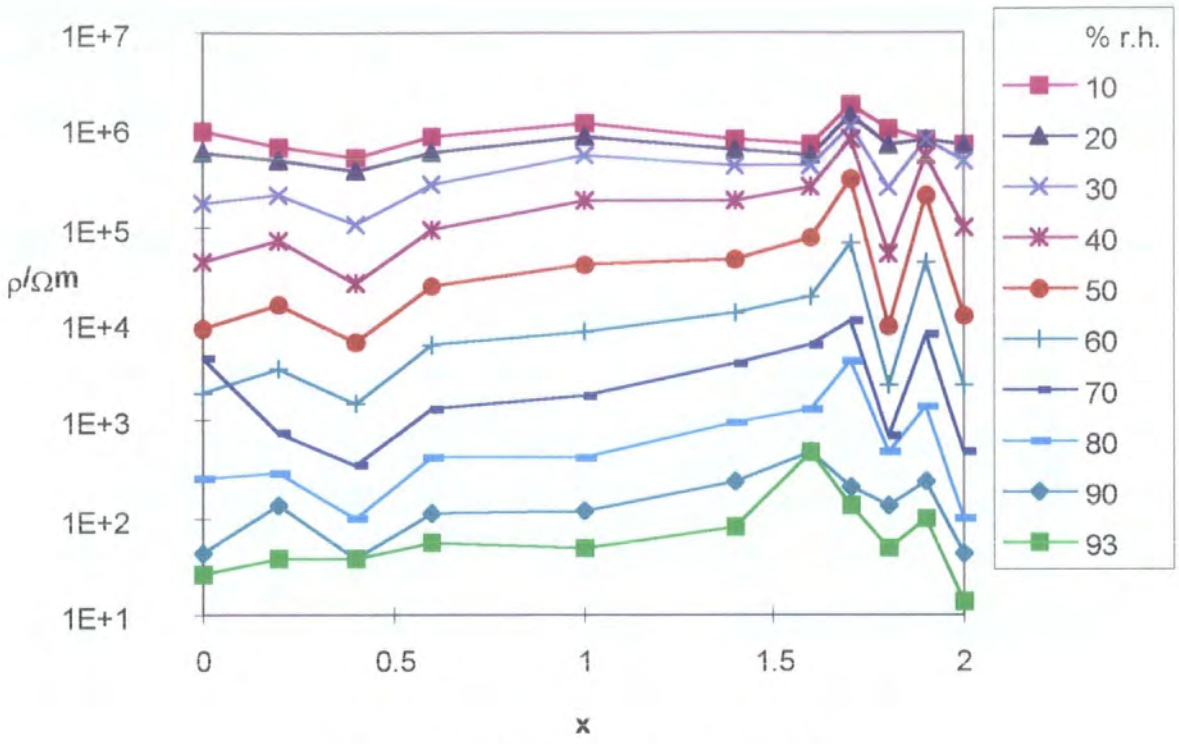

Figure A3.7 -Temperature 90 °C

APPENDIX 4

Figures A4.1 a to f - Real versus imaginary impedance for sample x = 1.8 at various humidities.

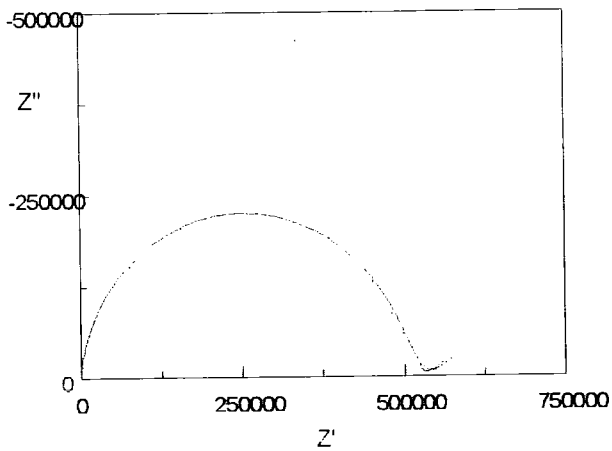

a - 93% r.h.

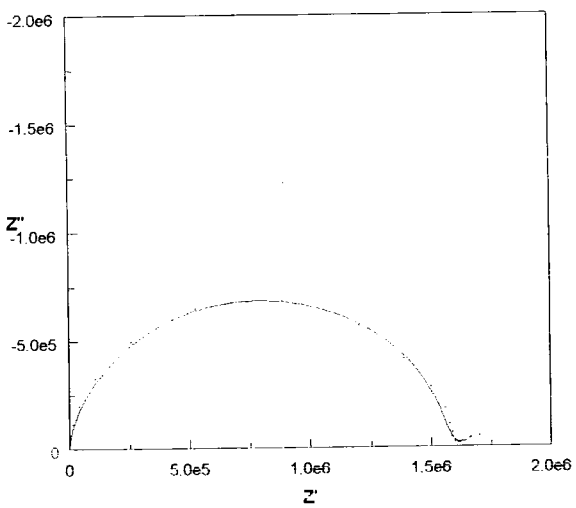

b - 84% r.h.

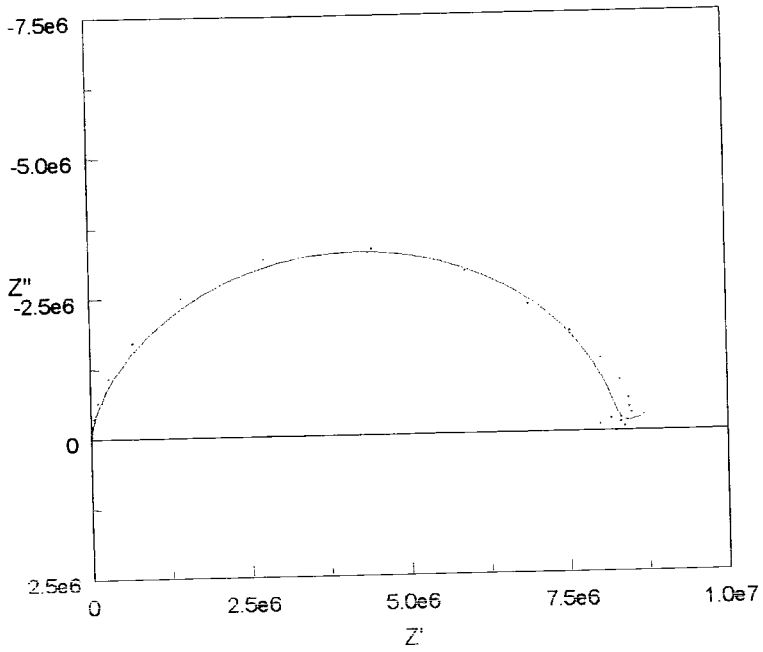
-7.5e6
-5.0e6
Z"
-2.5e6
0
2.5e6
0
2.5e6
5.0e6
7.5e6
1.0e7
Z'

c - 79% r.h.

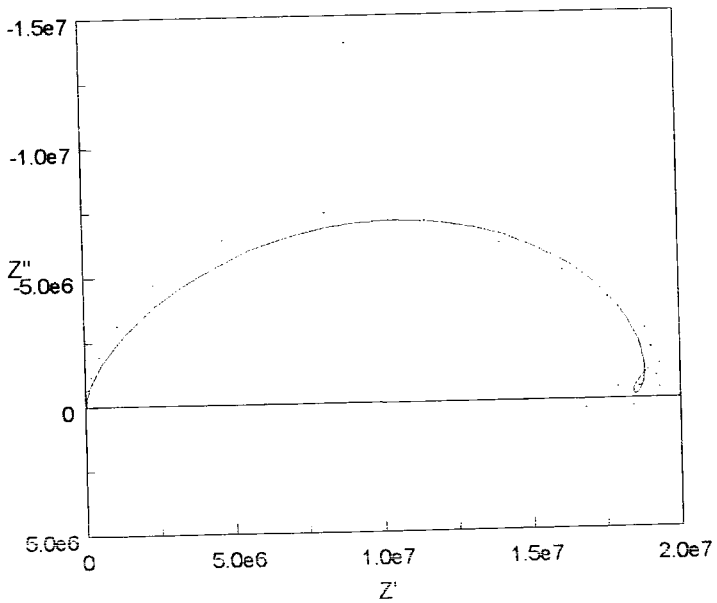
-1.5e7
-1.0e7
Z"
-5.0e6
0
5.0e6
0
5.0e6
1.0e7
1.5e7
2.0e7
Z'

d - 76% r.h.

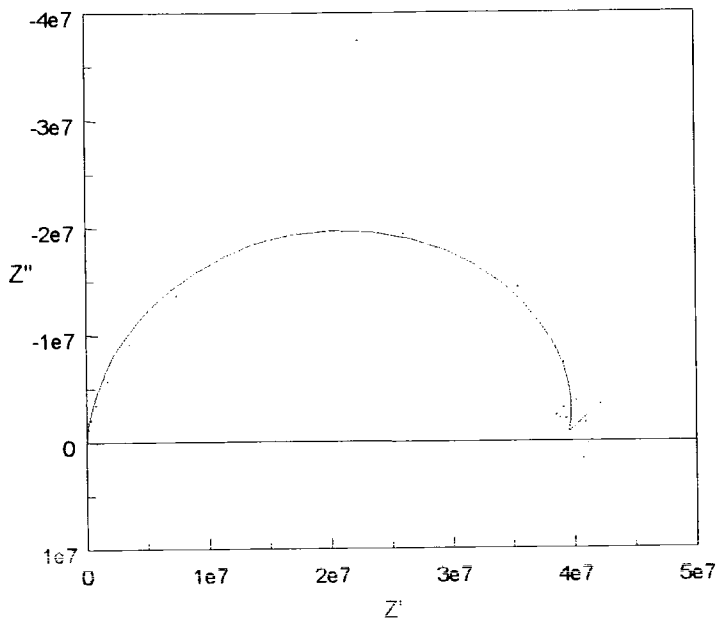
-4e7
-3e7
-2e7
Z''
-1e7
0
1e7
0
1e7
2e7
3e7
4e7
5e7
Z'

e - 64% r.h.

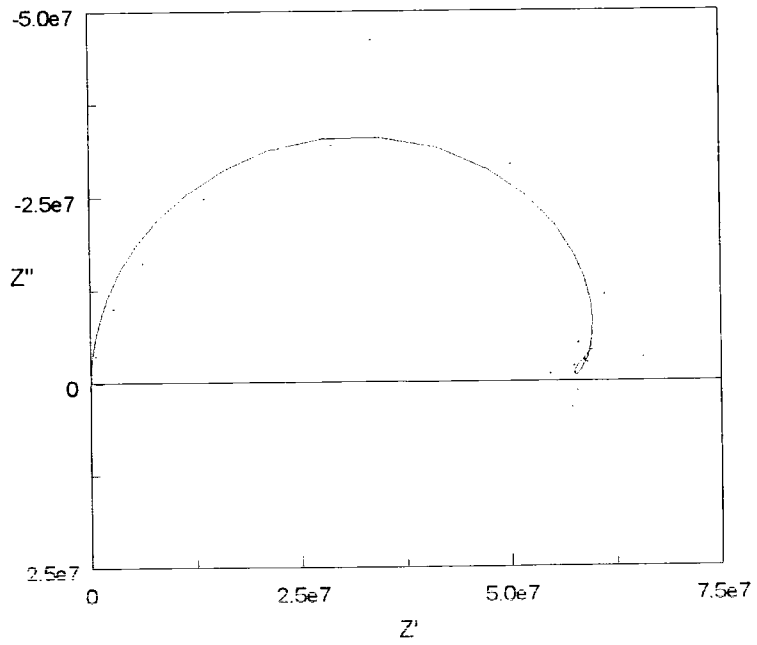
-5.0e7
-2.5e7
Z''
0
2.5e7
0
2.5e7
5.0e7
7.5e7
Z'

f - 55% r.h.

Figures A4.2 a to e - Real versus imaginary impedance for sample x = 0.2 at various humidities.

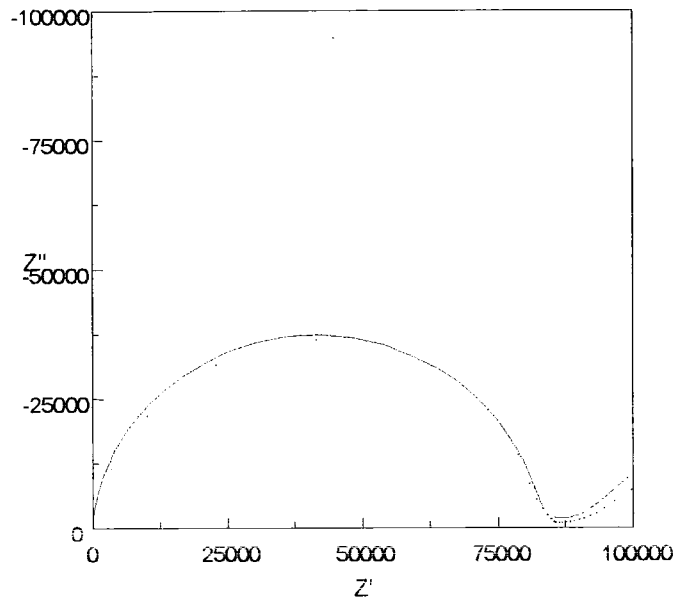

a - 92% r.h.

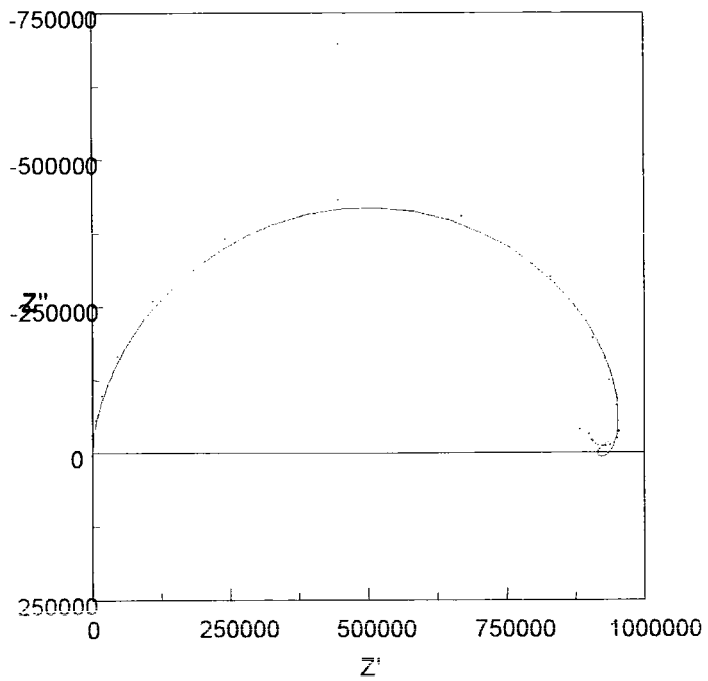

b - 81% r.h.

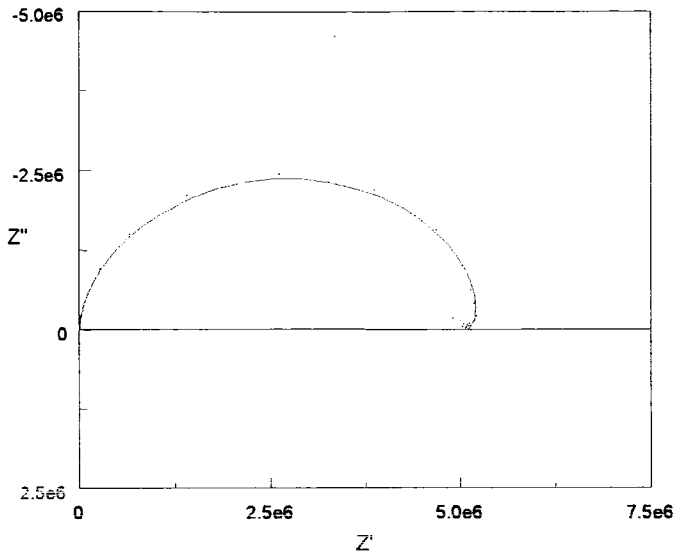
-5.0e6
-2.5e6
Z"
0
2.5e6
0
2.5e6
5.0e6
7.5e6
Z'

c - 68 % r.h.

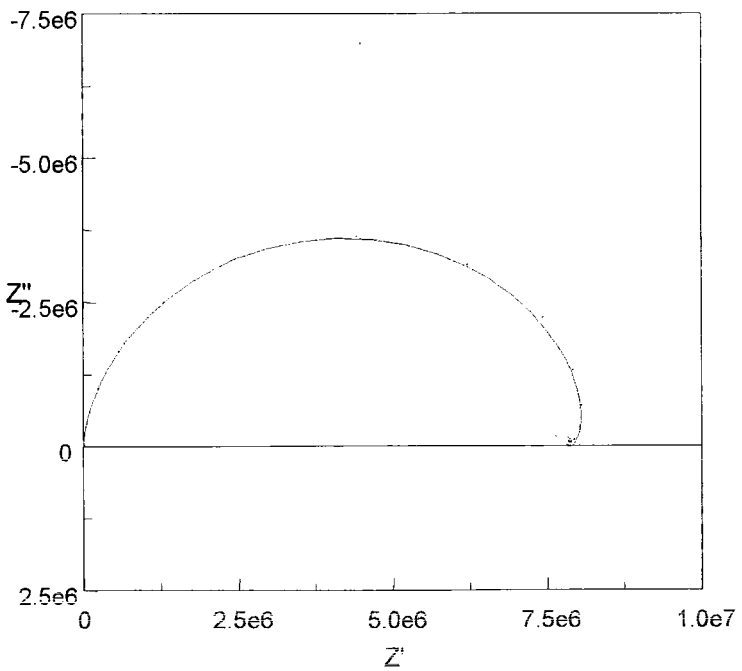
-7.5e6
-5.0e6
Z"
-2.5e6
0
2.5e6
0
2.5e6
5.0e6
7.5e6
1.0e7
Z'

d - 61% r.h.

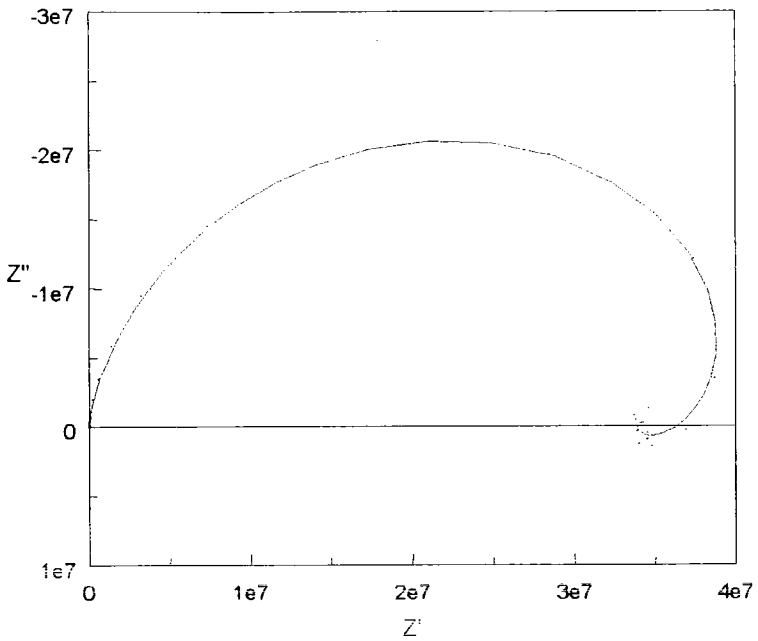

e - 45% r.h.